GALLIUM NITRIDE INTEGRATED MICROSYSTEMS FOR RADIO FREQUENCY APPLICATIONS

by

Azadeh Ansari

A dissertation submitted in partial fulfillment
of the requirements for the degree of
Doctor of Philosophy
(Electrical Engineering)
in the University of Michigan
2016

Doctoral Committee:

Professor Mina Rais-Zadeh, Chair
Professor Pei-cheng Ku
Professor Kevin Pipe
Professor Jasprit Singh

© Azadeh Ansari
All rights reserved
2016

To

My Parents

for their endless love

Acknowledgement

First of all, I would like to dearly thank my advisor, Professor Mina Rais-Zadeh, for her constant guidance and support. None of this work would have been possible without her help and patience. During my PhD years, she was not only a great mentor, but also a strong motivator and role model for me and I shall always remain thankful for her believing in me and providing me the opportunity to conduct research in this field. I am also thankful to my research committee, Prof. Jasprit Singh, a wonderful teacher of not only semiconductor physics but also wellness and life; Prof. Kevin Pipe and his research group for sharing their expertise in acoustic waves and thermal modeling of AlGaN/GaN HEMTs; and Prof. Peicheng Ku and his research group for their wisdom on GaN growth and material characterization.

In the past five years, the resonant MEMS group has been a second home to me where I lived with my lab-mates and am grateful to them for making working insightful and fun, from when I first started, Yonghyun, Vikram, Vikrant, and Zhengzheng and in subsequent years Adam, Muzhi, Cesar, Mohsen and Milad. I would like to take the opportunity to particularly thank Vikrant who was my clean room mentor and taught me all the intricacies of micro/nano fabrication, which I had absolutely no background in; Lei Shao from Prof. Pipe group kindly shared his fabrication recipes of GaN HEMTs with me and was the person to reach out for when anything would go wrong with the HEMT fabrication; and Adam who simply made our lab more fun and was the helping hand when needed. Special thanks go to the postdoc members in our lab Dr. Roozbeh Tabrizian and Dr. Haoshen Zhu

for their expertise in acoustics and all the technical discussions. I will be forever grateful for the help and support of all my colleagues for providing a friendly and productive research environment in the lab.

It goes without saying that none of this research would have been accomplished was it not the help and assistance of the staff at the Lurie Nanofabrication Facility (LNF) at University of Michigan. I am very grateful that I had the opportunity to work at LNF and WIMS (center of wireless integrated micro-systems) at University of Michigan, where a very significant portion of the MEMS history has been shaped throughout the years.

I would also like to express my gratitude to my dear friends in Ann Arbor, who made Ann Arbor home away from home for me. I cannot imagine how my life would have been if I did not share all the good moments and memories with them.

Above all, I would like to express my deepest appreciation to my parents, Parvin and Mojtaba for their endless love and support. They are the ones who encouraged me to reach for my goals and aim high. I certainly owe all my accomplishments to them. A big thank you goes to my dearest grandmother, Tooran, who brought a smile on my face each and every time I would see her through Skype during the last five years. I dedicate this thesis to my family for their unconditional love.

Table of Contents

Dedication……………………………………………………………………………...ii

Acknowledgement iii

List of Figures viii

List of Tables xxvii

Abstract xxviii

Chapter 1 Introduction 1

1.1 Motivation and Background 1

1.2 Piezoelectric Transduction 5

1.3 Quality Factor and $\boldsymbol{f} \times \boldsymbol{Q}$ limits 8

1.4 Coupling Efficiency and the $\boldsymbol{keff2} \times \boldsymbol{Q}$ Metric 11

1.5 Temperature Coefficient of Frequency 12

1.6 Power Handling Capability 14

1.7 Research Objectives & Contributions 14

5.1 Organization of Thesis 16

Chapter 2 Electromechanical Material Properties and Process Technology of Gallium Nitride Thin Films 21

2.1 Motivation, background and Challenges 22

2.2 Electro-mechanical Properties of GaN 24

2.3 Crystallinity of GaN on Si 28

2.4 GaN-on-SOI Epitaxial Growth 32

2.5 Fabrication of GaN MEMS 33

2.6 GaN Resonators with Embedded Meshed Metal Bottom Electrode 37

2.7 Conclusion 42

Chapter 3 Gallium Nitride MEMS Devices 46

3.1 GaN-on-Si thickness-mode MEMS resonators and filters 47

3.2 GaN Thickness-mode MEMS Resonators 54

3.3 GaN Contour-mode MEMS Resonators 58

3.4 GaN Radial (Breathing)-mode Coupled Ring Resonators 59
3.5 Conclusion 59
Chapter 4 Integration of GaN MEMS, HEMTs and Resonant Body HEMTs 62
1.1 Intimate Integration of GaN MEMS Resonators and HEMTs: Two Approaches .. 63
1.2 GaN Resonator/HEMT Device Modelling 66
1.3 HEMT Characterization 66
1.4 Integrated GaN Resonators/HEMT Characterization 68
1.5 Temperature Compensation of GaN MEMS Resonators 70
1.6 The Resonant Body Transistor 74
1.7 RB-HEMT Modeling 77
1.8 RB-HEMT Measurement Results 80
1.9 RB-HEMT Analytical Modelling 87
1.10 Conclusion 92
Chapter 5 Depletion-mediated AlGaN/GaN Piezoelectric Resonators and Resonant HEMTs 96
5.1 A Brief History 97
5.2 Design and Characterization 98
5.3 Effect of Electric Field on Acoustic Properties 99
5.4 *Q* Enhancement 108
5.5 Standard GaN piezoelectric resonators with lateral electric field excitation ... 112
5.6 Optimization of the geometry of acoustic cavity 114
5.7 Phonon Trap Design 115
5.8 Device Characterization 117
5.9 Forward-biased Schottky IDTs 121
5.10 Embedded Resonant AlGaN/GaN HEMTs 124
5.11 Resonant HEMTs: Design and Characterization 126
5.12 *Q* Enhancement Mechanism in Resonant HEMTs 129
5.13 Thermal Modelling 130
5.14 Conclusion 134

Chapter 5: References 135
Chapter 6 Big Picture & Future Directions.. 137

List of Figures

Figure 1.1 The combined need for digital and non-digital functionalities in an integrated system is translated as a dual trend in the International Technology Roadmap for Semiconductors (ITRS): miniaturization of the digital functions (“More Moore”) and functional diversification (“More-than-Moore”). Image taken from ITRS [1.1]. 2

Figure 1.2 GaN HEMTs and power transistors find diverse applications in RF, microwave and satellite communication. Image taken from Cree (Wolf Speed) [1.3]. 3

Figure 1.3 (a) A simplified schematic of a front-end transmitter based on all-GaN modules. (b) A schematic of a GaN MEMS/HEMT-based pierce oscillator. 4

Figure 1.4 COMSOL simulation of displacement of an exemplary resonator showing (a) fundamental length-extensional mode, (b) cross section of a thickness-extensional resonance mode. 7

Figure 1.5 (a) Vertical electric field applied between the top and the bottom electrode, and (b) lateral electric field between two adjacent electrodes. (c) This work: electric field applied between the top electrode and an embedded bottom electrode. 8

Figure 1.6 Theoretical $f \times Q$ limits of GaN showing Akhieser and L-R regime for phonon-phonon loss limit (black lines), phonon-electron loss limit at different carrier density levels (blue lines) and TED limit (red line) [1.15]. 10

Figure 1.7 A simple schematic of an RF transceiver module. GaN power amplifiers (PAs) are already being used in base stations. Future direction of research on GaN includes realization of novel electroacoustic devices (e.g. acoustic circulators), and integration of all GaN components to build an integrated GaN MMIC transceiver module. 15

Figure 1.8 A simplified cross section schematic of my thesis organization with a single device representing the main idea in each chapter. Chapter 2 involves the growth and fabrication of such structures. 18

Figure 2.3 GaN stiffness matrix components *vs.* temperature. Temperature coefficient of stiffness components are extracted for C_{11}, C_{33}, C_{12}, C_{13} and C_{44} for GaN Wurtzite crystalline structure. 27

Figure 2.1 Ga-face and N-face crystal structure of GaN.GaN thin films grown by MOCVD yield Ga-face, whereas MBE-grown GaN yields a N-face crystalline structure [2.9]. 29

Figure 2.2 XRD spectroscopy on a GaN thin film grown on a Si (111) substrate using metal-organic chemical vapor deposition (MOCVD). Inset: Rocking curve of the (0002) GaN plane exhibits a very clear peak and a FWHM of 1296 arcsec [2.4]. 30

Figure 2.4 Schematic of the epi-stack of MOCVD-grown AlGaN/GaN heterostructure on Si (111) by Nitronex Corporation. The thickness of the transition and buffer layers are indicated. 2DEG is induced at the AlGaN/GaN interface due to spontaneous and piezoelectric polarization. The peak charge concentration of 2DEG measured with Hg

probe CV measurements is 3×10^{19} cm^{-3} concentrated at an average peak distance of ~190 Å from the AlGaN surface. 32

Figure 2.5 (a) GaN-on-SOI wafer stack and (b) XRD of the thin film GaN layer showing an FWHM of 0.535˚ [2.20]. 33

Figure 2.6 Fabrication process flow; a) mesa isolation using a short chlorine etch, b) Ohmic contact metallization and rapid thermal annealing, c) formation of gate Schottky contac, d) deposition of top metal electrode of the resonator, e) GaN chlorine-based plasma etch for defining resonator contours, f) DRIE backside etch and sputtering of gold as the bottom metal electrode. 36

Figure 2.7 Fabrication steps: (a) mesa isolation, AlGaN is etched to define the active area of resonator/HEMTs, (b) ohmic contact metallization and annealing, used for contacting 2DEG and forming the source and drain of the HEMTs, (c) Schottky contact formation used as IDT sets for acoustic excitation/sensing and HEMT gates. (d) Trenches are made through GaN and Si is subsequently etched isotropically using XeF2. 37

Figure 2.8 Various MEMS devices relized with the fabrication process demonstrated above. (a) thickness-mode RB-HEMT (Chapter 4), (b) depletion-mediated piezoelectric AlGaN/GaN resonators, and (c) width-extensional resonant HEMTs (Chapter 5). 37

Figure 2.9 SEM images showing (a) 250-nm deep trenches made in GaN, forming a grid-like pattern; (b) trenches are refilled with W/SiO_2. GaN islands act as the seed layer for the GaN regrowth initiation. 39

Figure 2.10 SEM images of the cross-section of the regrown GaN, (a) on a reference GaN buffer layer of 500 nm thickness with no pattterns. The total thickness of the GaN stack is ~3 μm. (b) GaN regrown on W/SiO_2 structures and GaN islands. The regrowth of GaN has well-coalesced and a uniform film is grown on top of the meshed metal electrode......... 39

Figure 2.11 Room temperature photoluminescence (PL) measurement of 11 different points on (**a**) the reference sample, where GaN is grown on a thin GaN buffer layer without any patterns and embedded metals, or the reference, and (**b**) on the W/SiO_2 patterned structures. The PL measurements clearly indicate the GaN peak (at 364 nm) is not degraded in (**b**).. 40

Figure 2.12 Fabrication steps of GaN resonator with embedded bottom electrode. (a) A thin layer of GaN is grown on a Si (111) substrate, (b) 250 nm deep trenches are made in the GaN layer using BCl_3/Cl_2 plasma etch, (c)thetrenches are filled with sputtered W and (d) evaporated SiO_2, (e) GaN device layer is regrown on the W/SiO_2 mesh, starting from the bottom GaN seed layer, (f) trenches are made through the GaN layer to access the Si substrate, (g) the top metal is deposited on the device area, (h) the resonator is released with XeF_2 isotropic etch.. 41

Figure 2.13 (a) An exemplary schematic of a GaN resonator with a thick GaN layer grown on W/SiO_2 embedded electrodes. (b) The resonant stack schematic with a total thickness of ~3 μm. (c,d) SEM images of the GaN trenches before the GaN regrowth.................. 42

Figure 3.1 (a) A schematic view showing the TPoS filter configuration. (b) COMSOL 2D simulation of the displacement of the fifth-order thickness resonance mode.................. 48

Figure 3.2 (a) An SEM image of a GaN-on-Si filter with electrode width of 10 µm, electrode spacing of 3 µm and active area of 260× 240 µm^2. (b) Measured filter frequency response exhibiting a center frequency of 2.1 GHz and a bandwidth of 20.2 MHz......... 49

Figure 3.3 Wide-band filter frequency response showing a good match between the (a) simulated and (b) measured frequency responses.. 49

Figure 3.4 Measured S_{21} response of a TPoS filter at 802.5 MHz. Inset shows the mode shape obtained using ANSYS.. 50

Figure 3.5 (a) A SEM image of an apodized GaN-on-Si FBAR with an active area of 81600 µm^2. (b) ANSYS simulation of the FBAR showing the first-order thickness mode frequency at 370 MHz. 50

Figure 3.6 Measured response of the GaN-on-Si FBAR. Extracted mechanical *Q* is 424 at 2.1 GHz.. 51

Figure 3.7 (a) Mason's model of a thickness-mode resonator. (b) Simulated and measured impedance plots of the FBAR in a wide frequency range, showing a good match between the measured and simulated responses. The impedance is shown in logarithmic scale. .. 52

Figure 3.8 Measured S_{21} response of the TPoS filter at different power levels................ 53

Figure 3.9 Linear resonance frequency variation of the TPoS filter over a temperature range of 150 K to 300 K. 53

Figure 3.10 SEM image of a fabricated 40 µm × 60 µm GaN BAW resonator, with tethers of 20 µm in length and 5 µm in width. 55

Figure 3.11 Wide-band frequency response of the 40 µm × 60 µm GaN resonator. The effect of capacitive feed-through is not de-embedded from the response. The mode shape for each thickness-mode resonance is also shown. 56

Figure 3.12 De-embedded frequency response of the 40 µm × 60 µm GaN resonator with a resonant frequency of 8.7 GHz, and an extracted Q of 330 at room temperature and ambient pressure. Capacitive feed-through is de-embedded from the resonator response using an unreleased but otherwise identical resonator. 56

Figure 3.13 Two-tone power measurements of the (a) first and (b) fourth-order thickness-mode harmonics. The IIP3 value is extracted to be 30.6 dBm and 29.2 dBm, respectively, with a frequency separation of 5.1 KHz. (c) P1-dB measurement showing P1-dB of ~16 dBm for both the first and the forth-order thickness-mode resonances. It must be mentioned that different coupling coefficients affect IIP_3 values of the two modes. 57

Figure 3.14 Room temperature frequency response of an 80 µm × 40 µm GaN resonator with center frequency (f) of 119.8 MHz and high *Q* of 7413. This resonator demonstrates a very high frequency ×Q value of 0.88×10^{12}. 58

Figure 3.15 Normalized resonance frequency and measured Q of the GaN resonator *vs*. temperature. The TCF value of the resonator is extracted to be -17.2 ppm/K. 58

Figure 3.16 Wide band frequency response of dog-bone resonators. The inner and outer radii are 20 and 60 μm respectively. 60

Figure 3.17 Narrow band resonance frequency of (a) 3rd-order breathing mode at ~373 MHz, (b) 9th-order breathing mode at ~900.7 MHz and (c) highest $f \times Q$ values of 1.05×10^{13} achieved at 1.62 GHz. 60

Figure 4.1 A simple transmitter MMIC module, ideally realized in a GaN platform. Two approaches are investigated to realize a GaN-based oscillator: (I) a conventional oscillator configuration (e.g., Pierce oscillator), wherein a MEMS resonator is cascaded with an amplifier and the loop is closed with an addition of a few capacitors if required. (II) Resonant body HEMT (RB-HEMT), where the role of a resonator and a transistor is combined as the main building block of an oscillator. 63

Figure 4.2 (a) Platform I: a passive bulk-mode resonator is co-fabricated with a HEMT, with the resonator output connected to the HEMT gate. (b) Resonant body HEMT: Confined 2DEG at AlGaN/GaN interface acts as the bottom electrode to actuate AlGaN layer piezoelectrically. Signal is then picked up and amplified by a resonant HEMT. 64

Figure 4.3 An all-GaN integrated microsystem platform wherein GaN MEMS resonators are monolithically integrated with AlGaN/GaN HEMT. Resonator output is connected to the HEMT gate. SEM images of a GaN resonator co-fabricated with a two-gate

AlGaN/GaN HEMT. Drain and source are 7 μm apart. Two-fingered gates are each 1 μm long and 100 μm wide. The resonator is a 40 μm × 80 μm resonator. 65

Figure 4.4 Equivalent circuit model of the MEMS resonator cascaded with a HEMT. The output port of the resonator is connected to the gate of the HEMT, where the signal gets amplified and collected at the drain. The inductances connected to the gate and the drain model the Bias Tees. 66

Figure 4.5 DC I-V curves of a two-fingered, 100 μm wide AlGaN/GaN HEMT. Drain current is plotted vs. drain-source voltage, with V_{GS} swept from -0.5 V to -2 V in -0.5 V steps.. 67

Figure 4.6 (a) Normalized drain DC current variation over temperature range of 100 K to 350 K with respect to its value at 100 K. T= 350 K as the maximum operation temperature reported here is the measurement tool limit. (b) Drain current and extrinsic trans-conductance *vs.* V_{GS} at 100 K and 350 K for V_{DS} = 10 V. 68

Figure 4.7 SEM image of a fabricated GaN BAW resonator integrated AlGaN/GaN HEMT, with the zoomed view of the resonator. The geometry of the fabricated resonators are summarized in the table. 69

Figure 4.8 (a) Measured S_{21} response of a contour-mode resonance (red). Unreleased device response is shown in grey and the de-embedded response is shown in blue. (b) Cascaded resonator/HEMT response showing more than 30 dB signal tuning. 69

Figure 4.9 (a) Measured S_{21} response of fundamental thickness-mode resonance of a cascaded resonator/HEMT structure. The insertion loss is modulated with various drain DC voltages. (b) The de-embedded fourth-order thickness-mode resonance with ~7 dB of improvement in the insertion loss.. 70

Figure 4.10 Temperature trends of GaN thickness-mode resonator (a) without and (b) with SiO_2 layer. The level of temperature-compensation depends on the stress profile in the location of SiO_2. Lower TCF value achieved for the higher-order mode can be attributed to higher stress levels in SiO_2 for the higher-order resonance mode. 71

Figure 4.11 (a) Simulated Q and k_t^2 of the first-order thickness-mode resonance of Device B vs. SiO_2 thickness based on Mason's model, taking into account only the acoustic impedance mismatch of the materials in the stack. (b) Simulated TCF vs. SiO_2 thickness, assuming TCE of +160 ppm/K for SiO_2 and -60 ppm/K for the GaN-based stack. 72

Figure 4.12 Measured admittance (Y_{11}) plot of the fundamental thickness-mode resonance of Device B, comparing the passivated and non-passivated resonance peaks. Both Q and k_t^2improve with 400 nm SiO_2 passivation. (b) Measured Q vs. temperature of the Device B, showing a reduction of only 7% from T=200 K to T=300 K. 73

Figure 4.13 Schematic of AlGaN/GaN RB-HEMT. AC signal is applied to the back gate, which is biased in the depletion region (shown as the darker area under the back gate) for efficient transduction. 2DEG, at the AlGaN/GaN interface, acts as the bottom electrode to piezoelectrically actuate the thickness resonance mode of the stack. The 2DEG carrier

density is modulated with the induced acoustic strain and reflected in the drain source current (ID). 75

Figure 4.14 SEM images of the AlGaN/GaN RB-HEMT with inter-digitated fingers. Top gate length is 1 μm. The width of source and drain is 6 μm, and the back gate electrode is 8 μm wide. 76

Figure 4.15 COMSOL 2-D simulation of strain in the thickness direction (z), showing the second-order thickness-mode resonance of GaN-based RB-HEMT. The AlGaN piezoelectric transduction layer is sandwiched between the back gate (top metal electrode) and the 2DEG (bottom electrode). The simulation is used to define the electrode layout as shown in Fig. 4.14.. 78

Figure 4.16 Equivalent electrical circuit model of the four-terminal RB-HEMT. AC signal is fed to the back gate and collected from the drain. The actuation takes place between the back gate and the source. The induced acoustic wave modulates the drain current. Values of the acoustic transconductance (g_a) and the back gate transconductance (g_{mb}) both depend on the top DC gate voltage.. 80

Figure 4.17 Two-port I-V (conductance) measurement between the Schottky back gate and the source ohmic contact. A turn-on voltage of 0.75 V is measured for the Schottky contact. The inset shows the reverse Schottky region of operation, where the back gate is biased at. The back gate voltage of ~ -1.9 V marks the VBG value at which the 2DEG is totally depleted (pinch-off voltage).. 81

Figure 4.18 DC response of the read-out HEMT, consisting of the drain, top gate, and source (back gate is floating). The gate width is 100 µm. DC I-V transfer curves are plotted as: (a) Drain current versus the drain voltage at different gate voltage values (I_D-V_{DS}). The negative resistance at higher drain currents is associated with self-heating in the AlGaN/GaN HEMT channel. (b) Drain current and transconductance versus top gate voltage at V_{DS}= 0.4 V (I_D-V_{GS} and G_m-V_{GS}). (c) Drain current of the read-out HEMT is plotted vs. the DC voltage of the back gate with the top gate and drain voltage fixed at V_{TG}= 0 V and V_D= 0.4 V. 81

Figure 4.19 Admittance parameters (Y_{21} and Y_{12}) are plotted at (a) V_{BG}= 0 V and (b) V_{BG}= -1.8 V. The resonance peak only appears in (b) where the 2DEG under the back gate is depleted. (c) The acoustic transconductance (g_a) is extracted from (b). The second-order thickness-mode resonance at 4.23 GHz is excited, with a *Q* of 250 at V_{BG}=-1.8 V. The electrical back gate feed-through floor (gmb= 0.043 mS) is subtracted from $|Y_{21}$-$Y_{12}|$ to plot ga. V_{TG}= -1 V, and V_{DS}= 0.4 V is kept constant in all the plots. 83

Figure 4.20 Fundamental thickness mode resonance of the RB-HEMT. The acoustic peak only appears when back gate is biased in depletion. The DC voltage on the back gate can act as a switch and turn the acoustic transconductance ON and OFF. 84

Figure 4.21 (a) Total transconductance dependency on the top gate voltage (V_{BG}=-1.8 V, V_{DS}= 0.4 V). $|Y_{21} – Y_{12}|$ is plotted at different top gate voltages. The acoustic and back gate electrical transconductance decrease as the top gate DC voltage decreases. (b) Acoustic

transconductance is plotted versus top gate DC voltage. The acoustic transconductance drops to zero when the channel is fully depleted (at V_{TG}= -2 V). 85

Figure 4.22 (a) Total transconductance $|Y_{21} – Y_{12}|$ at different drain-source voltages in the linear region of operation. (b) The acoustic transconductance decreases as the depletion region grows towards the drain contact at higher V_{DS} values. (c) When the 2DEG under the drain contacts gets pinched (SAT region), the acoustic transconductance value drops to zero. V_{DS}= 0.5 V, corresponds to the knee voltage measured in Fig. 4.7, when V_{TG}= -1 V, marking entering the saturation region of operation. The darker area in the AlGaN channel shows the depletion region, growing at higher V_{DS} values... 86

Figure 4.23 Frequency response of the drain motional current ($g_a \times V_{bg}$) of the RB-HEMT. As the input RF power increases, the motional current increases. Nonlinear effects start to show up at higher P_{in} values. 87

Figure 4.24 (a) Structure of the read-out HEMT, showing the source and drain access regions and the intrinsic HEMT. (b) The external strain in the channel is induced from the back gate actuator, and effectively modulates the sheet density of the drain access region only. The drain access resistance can be equivalently modeled as a transistor [4.25], where the channel resistance is modulated with the back gate voltage. The voltage drop at the drain and source access regions, results in effective voltages of V_{Di} and V_{Si} at the intrinsic HEMT drain and source terminals... 91

Figure 5.1 SEM image of the fabricated AlGaN/GaN resonator. (b) A cross-section schematic of the depletion-mediated resonator, where the input Schottky IDTs are biased in depletion and the output Schottky IDTs are biased at 0 V_{DC}. Access to 2DEG is provided via Ohmic contacts biased at 0 V_{DC}. (c) COMSOL simulation of the stress profile of the ninth-order width-extensional resonance mode. (d) S_{21} frequency response at P_{in}= -5 dBm when the depletion voltage at the input port is varied from 0 V to -40 V. The voltage at output port is kept at 0 V_{DC}. Mechanical *Q* increases from 3500 at -5 V to 5000 at -40 V. 99

Figure 5.2 Dependency of acoustic properties of piezoelectric resonators on DC voltage. (a) Frequency (or acoustic velocity) tuning, normalized to the resonance frequency at 0 V. (b) electromechanical coupling coefficient (k_t^2), (c) mechanical *Q*, and (d) $k_t^2 \times Q$ *vs.* DC voltage. 100

Figure 5.3 Diode-embedded equivalent circuit model of depletion-mediated AlGaN/GaN resonators. 101

Figure 5.4 Schottky characteristics: C-V (measurement taken at 1 MHz) and DC I-V curves between one Schottky IDT set and Ohmic GND. -1.65 V marks the threshold voltage at which point the depletion region pinches the 2DEG. 0.75 V marks the turn-on voltage of the Schottky diode. In case (i), at zero DC voltage, the depletion layer depth in the z-direction is set by the thickness of the AlGaN layer; in case (ii) the depletion layer has pinched the 2DEG sheet and penetrated into the high-resistivity GaN layer. 102

Figure 5.5 (a) Energy band diagram of the AlGaN/GaN hetero-structure under reverse bias condition. (b) Measured 2DEG carrier concentrations *vs.* depth from the C-V profile in Fig. 5.4. 104

Figure 5.6 *Q* amplification and *IL* enhancement at frequency of resonance for P_{in}= +10 dBm. Modulation of the impedance of the depletion layer with a frequency equal to the actuation frequency creates an electrostatic force, which adds to the piezoelectric force only at the frequency of resonance. 109

Figure 5.7 Carrier concentration *vs.* depth from the AlGaN surface in AlGaN/GaN heterostructure. The dashed lines show charge modulation when ac signal is applied in addition to a negative DC voltage to the Schottky contact. 111

Figure 5.8 Charge, electric field, and force component of depletion-mediated resonators with uniformly-distributed charge carriers. $Z_{d,min}$ and $Z_{d,max}$ denote the minimum and maximum depletion widths when ac signal is applied [5.19]. 112

Figure 5.9 (a) S_{21} frequency response of the ninth-order width-extensional resonance mode of GaN resonator when 2DEG is removed. The voltage applied between two adjacent electrodes are -40 V, 0 V and +40 V. (b) Small fractional resonance frequency change with applied DC voltage. The slope of the frequency tuning *vs.* DC voltage is 0.39 ppm/V, corresponding to piezoelectric tuning effect. (c) Cross section schematic of the lateral-field-excited GaN resonator. 113

Figure 5.10 SEM images of a ninth-order width-extensional mode resonator with (a) single narrow tethers, and (b) multiple tethers. (c) “Phonon trap” design, where narrow tethers do not exist. 114

Figure 5.11 Schematic of a ninth-order width extensional phonon trap using Schottky IDTs to actuate and sense acoustic resonance modes. 115

Figure 5.12 Dispersion characteristic of the 9th width-extensional mode for different widths, along with the schematic demonstration of the acoustic engineering concept for phonon trapping. 116

Figure 5.13 Simulated synthesized mode shape of the phonon trap along with its cross sectional polarization and the proposed lateral-field excitation scheme. 117

Figure 5.14 A SEM image of a fabricated piezoelectric lateral field-excited AlGaN/GaN resonator. DC voltage is applied to one set of the Schottky IDTs for a more effective acoustic transduction. The device is designed to resonate at its 9th-order width-extensional mode.. 118

Figure 5.15 Measured S_{21} response at room temperature. A record high $Q_{unloaded}$ of 13,122 is extracted from the measured phase of S_{21} when V_{DC}= -9 V. 119

Figure 5.16 Phonon trap frequency response when the input RF power is varied from -20 dBm to 14 dBm. The improvement of *IL* and *Q* from -20 dBm to 5 dBm is attributed to efficient charge modulation as the depletion layer varies. The inset shows the zoomed plot. The weak spurious resonance modes are supressed a higher input levels. 119

Figure 5.17 Two-tone power measurement of the resonator shown in Fig. 6. The frequency separation of the two tones is 20 kHz and the extracted IIP3 value is 31.2 dBm. 120

Figure 5.18 Frequency vs. temperature dependency of (a) third-order resonance, and (b) ninth-order resonance modes of acoustic phonon trap. A TCF of ~-21 ppm/K is extracted for both resonance modes. 121

Figure 5.19 (a) SEM image of the AlGaN/GaN resonator. Access to the 2DEG sheet is provided by Ohmic contacts outside of the active device area indicated as GND. (b) DC I-V curve of the forward biased output Schottky IDT, when input IDT set is biased at -10 V, -20 V, and -40 V. 123

Figure 5.20 (a) Frequency response of the AlGaN/GaN resonator at its 9th-order width-extensional resonance mode at frequency of ~733 MHz and *Q*= 4,500, when the input IDT set is biased in depletion (i.e. V_{DC}= -40 V) and the output IDT set is forward biased with a DC voltage varying from 2 V to 5 V. The cross section of COMSOL simulation of the stress profile is shown in the inset. (b) Frequency tuning versus consumed DC power. Actuation IDT set is biased in depletion (V_{DC}= -40 V, -20 V, and -10 V) and sense IDT setis biased in forward region. The slope of the linear fit is -10 ppm/mW.................... 123

Figure 5.21 Normalized resonance frequency vs. DC voltage applied to the sense IDT set. The acuation IDT bias is maintained at -40 V. The resonance frequency is normalized against its value at 0 V. Significant frequency tuning is observed once the sense IDT set enters the forward bias region. 124

Figure 5.22 (a) A cross-section schematic of a resonant HEMT, with three IDT fingers on each side of the acoustic cavity for piezoelectric actuation and an embedded HEMT in the middle of the cavity to readout the strain. (b) COMSOL simulation of stress profile of the ninth-order width-extensional resonance mode indicating the Source and Drain located at the location of maximum stress. 125

Figure 5.23 SEM images of the resonant body HEMT. The trenches are tapered to concentrate the acoustic energy in central region of the device and couple the propagating acoustic wave in the center to the evanescent waves in the flanges. 126

Figure 5.24 DC trends of the current and consumed DC power of the embedded HEMT, when no DC voltage is applied to the gate. 127

Figure 5.25 Frequency response of the AlGaN/GaN resonator at various V_{DS}. The drain-source DC voltage is varied from 4 V to 9 V. The quality factor of the resonator increases with an increase in the electric field applied between the source and drain. 127

Figure 5.26 Frequency response of the piezo-resistive trans-conductance (g_m). $|g_m|$ rises to ~107 μS when V_{DS} is biased at 9 V and is hardly detectable with a value of only ~2 μS at V_{DS}= 2 V. The inset shows the dependency of $|g_m|$ on V_{DS}. 128

Figure 5.27 Thermo-elastic feedback loop, indicating the three terminals of the resonant HEMT (RF input, output and DC Source) and demonstrating a series of inter-related mechanisms. Once the thermal expansion/contraction caused by the resistive heating/cooling is in phase with the initial piezoelectric actuation, *Q* is enhanced........ 131

Figure 5.28 (a) SEM image of the resonant using a micro-thermocouple to estimate the temperature rise in the channel of the HEMT. (b) Frequency tuning versus consumed DC power. The slope of the linear fit is -29 ppm/mW. 133

Figure 6.1 Summary of GaN-based devices realized in this work showing the schematic of cross section of various classes of GaN-based MEMS devices, HEMTs and resonant HEMTs. 138

Figure 6.2 Big Picture: A simple schematic of an RF transceiver module. GaN power amplifiers (PAs) are already being used in base stations. Future direction of research on GaN includes realization of novel electroacoustic devices (e.g. acoustic circulators), and integration of all GaN components to build an integrated GaN MMIC transceiver module. 138

Figure 6.3 (a) Amplification, (b) attenuation of travelling acoustic wave based on the direction of electric field applied to the 2DEG channel via Source and Drain Ohmic contacts. $V_{electron}$ is assumed positive if electron drift direction is the same as the travelling wave and negative if it is in the opposite direction. 139

Figure 6.4 Acoustic diode or listening without being heard [6.9]. 141

Figure 6.5 Realization of piezoelectric acoustic diodes based on travelling surface acoustic waves or Lamb waves. The acoustic cavity is designed to avoid creation of standing waves. If the GaN waveguide is continuous in the wave propagation direction, the reflections from

the edges are minimized and thus one-directional acoustic communication would be possible. 142

Figure 6.6 (Top) Schematic images of Lamb-wave GaN devices, showing (a) the standing wave resonator, and (b) the travelling-wave delay-line structure. (Bottom) Frequency response of (a) the resonator and (b) the delay-line. The SEM images are shown in the inset. [6.10] 143

List of Tables

Table I: Properties of a selection of electromechanical materials…………………………...23

Table II: Electrical Properties of GaN……………………...…………………………….29

Table III Comparison of this work with more conventional TPoS resonators and filters……………………………………………………………………………………..53

Table IV Summary of measured performance metrics……………………………..........72

Table V Comparison of performance metrics of AlGaN/GaN resonant HEMTs………..92

Abstract

The focus of this work is design, fabrication, and characterization of novel and advanced electro-acoustic devices and integrated micro/nano systems based on Gallium Nitride (GaN). Looking beyond silicon (Si), compound semiconductors, such as GaN have significantly improved the performance of the existing electronic devices, as well as enabled completely novel micro/nano systems. GaN is of particular interest in the "More than Moore" era because it combines the advantages of a wide-band gap semiconductor with strong piezoelectric properties. Popular in optoelectronics, high-power and high-frequency applications, the added piezoelectric feature, extends the research horizons of GaN to diverse scientific and multi-disciplinary fields. In this work, we have incorporated GaN micro-electro-mechanical systems (MEMS) and acoustic resonators to the GaN baseline process and used high electron mobility transistors (HEMTs) to actuate, sense and amplify the acoustic waves based on depletion, piezoelectric, thermal and piezo-resistive mechanisms and achieved resonance frequencies ranging from 100s of MHz up to 10 GHz with *frequency×quality factor* ($f \times Q$) values as high as 10^{13}. Such high-performance integrated systems can be utilized in radio frequency (RF) and microwave communication and extreme-environment applications.

The first part of this research work is focused on the design and fabrication of high-performance GaN piezoelectric bulk acoustic wave (BAW) resonators and filters used in timing applications. High-order thickness-mode resonators with frequencies as high as 8.7 GHz are realized marking the highest frequency reported on GaN BAW devices to date.

Toward this end, GaN thin films grown on Si (111) substrates are utilized to ease the fabrication of suspended membranes and allow for future integration with Si CMOS circuitry. Because GaN is an inert, chemically-stable wide band-gap semiconductor, and can only be grown on single crystalline hexagonal substrates, it is rather difficult to build free-standing GaN structures. Etching GaN, as well as growing vertical metal-GaN-metal structures are particularly challenging, and mostly require non-conventional fabrication techniques, implemented in this work.

GaN material systems are very exciting for integration of diverse functionalities onto a single substrate. The second area in this research work is focused on the integration of AlGaN/GaN active components (HEMTs) and passives (capacitors, inductors, and *etc.*) with acoustic devices (resonators, filters and sensors). Cascaded structures of a GaN micromechanical resonators and HEMTs have been implemented in this work for the first time to build an oscillator, which is used in transceiver modules. The goal of this work is to ideally implement the RF transceiver module with a single all-GaN MMIC. Such GaN MMICs save area and power, operate at higher frequencies and have improved noise performance compared to the state-of-the art transceiver modules.

The two-dimensional electron gas (2DEG) sheet induced at the AlGaN/GaN interface is yet another exciting feature of GaN material systems, used to build novel electro-acoustic devices. The 2DEG sheet, confined within ~20 nm below the AlGaN surface, is highly sensitive to any potential change on the surface of AlGaN/GaN hetero-structures, making HEMTs perfect sensing elements. In this work, 2DEG is utilized for actuation, sensing, and amplification of longitudinal acoustic waves. For actuation of acoustic waves, the

2DEG sheet is used as the top as well as the bottom electrodes in resonant stacks to eliminate the deposition of metal layers and thus the metal loading effect. Also, by forming Schottky contacts and depleting the AlGaN layer, depletion forces are utilized in addition to piezoelectric forces to enhance Q by ten times achieving Q values of ~13,000 at resonance frequency of ~740 MHz marking the highest $f\times Q$ value and Q for GaN-based resonators to date. On the sensor side, by using the same basic concept as HEMT static strain sensors and leveraging the sensitivity of the charge density and mobility of 2DEG sheet to mechanical stress, multi-GHz resonant body HEMTs (RB-HEMTs) have been realized. Finally, the piezo-resistive properties of the 2DEG sheet is deployed to locally heat/cool the HEMT channel upon application of a DC voltage and flow of current, to add to the elastic force in the resonant structures and thus amplify the Q to a value much higher than its purely piezoelectric counterparts. Q-amplification from 2,000 to 13,000 has been achieved when DC voltage applied to the HEMT drain-source contact is increased from 4 V to 9 V. We have demonstrated that the pumped DC energy from the HEMT partially compensates the acoustic losses in GaN resonators. Once this amplification mechanism overcomes all existing loss mechanisms, self-oscillation can be achieved.

Future directions of research on GaN include fundamental studies and device-level explorations in order to shed light on the physical and electro-acoustic properties of GaN. Explorations of interactions of phonons and electrons, give birth to a new class of devices operating based on non-reciprocal propagation of the acoustic wave. By leveraging "acoustoelectric amplification" to break the acoustic wave propagation reciprocity, novel GaN-based acoustic devices, such as acoustic diodes/isolators and circulators can be

realized. Another area of future research direction is realization of all-GaN monolithically integrated RF modules that incorporate high-power electronic devices, acoustic devices and passive components. All the pieces of the transceiver module, including the modulators, oscillators, mixers, filters and power amplifiers can be replaced with a single MMIC, resulting in a significant reduction of the size and improvement of power efficiency, while enabling faster communication.

Chapter 1 Introduction

1.1 Motivation and Background

For the past few decades the semiconductor industry has been able to follow the Moore's law with the number of transistors in an integrated circuit (IC) being doubled in approximately every two years. Miniaturization has played an integral role in the evolution of microelectronics industry; until recently that shrinking the size of transistors and ICs have reached its physical limits given the technology used to build them. Of course, the trend for increased performances would continue, but instead, would be sustained by incorporation of new materials and novel devices. This trend is characterized by functional diversification of semiconductor-based devices and is designated as the "More-than-Moore" trend. [1.1]

To enable functional devices for tomorrow's smart technologies, there is a constant quest for novel materials that would overcome the challenges and limits that silicon is facing today. Group III-V semiconductors have many advantages to offer because of their superior and unique material/structural properties. Among them, GaN is of particular interest because its properties lie at the crossroad where piezoelectric, pyroelectric, and piezo-resistive properties meet, making it a perfect candidate for building functionally diverse modules, such as electro-acoustic devices. Furthermore, the ability to form hetero-structures with GaN-based material systems that confine 2DEG sheet with high mobility

and high sensitivity to strain opens up a wide variety of application for GaN-based electro-acoustic devices.

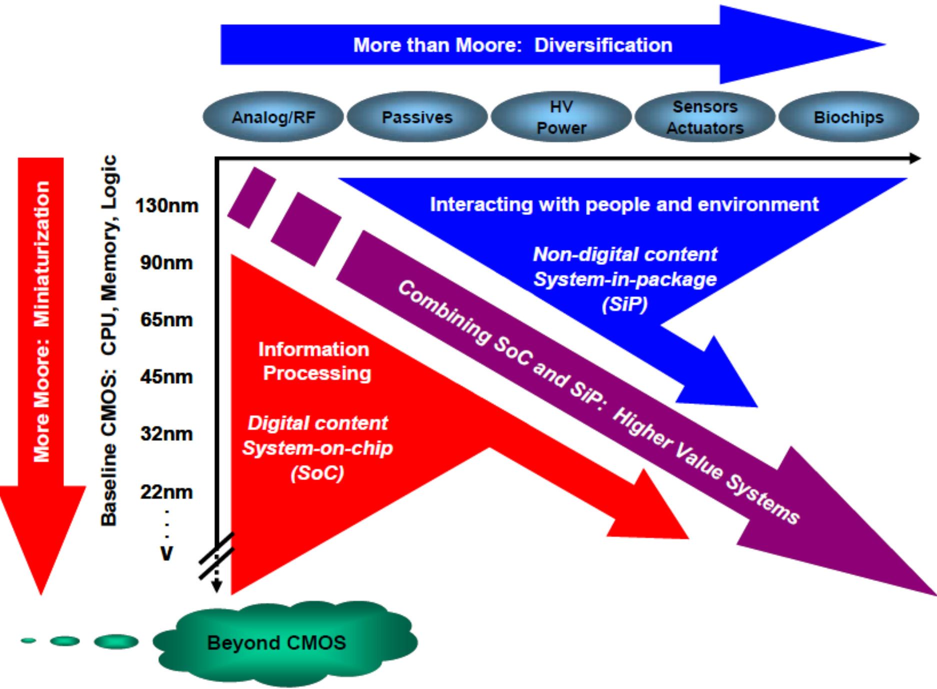

Figure 1.1 The combined need for digital and non-digital functionalities in an integrated system is translated as a dual trend in the International Technology Roadmap for Semiconductors (ITRS): miniaturization of the digital functions ("More Moore") and functional diversification ("More-than-Moore"). Image taken from ITRS [1.1].

GaN is the second most popular semiconductor today, only after silicon. The prime movers behind its growth have been the lighting industry (blue LEDs and lasers) and power electronic (AlGaN/GaN HEMTs used in power amplifiers). Recently, GaN HEMTs are being widely used in RF power amplifiers in base stations (Fig. 1.2). There is a great demand for miniaturization of such products and designers continuously move from hybrid to compact integrated solutions [1.2]. Integrating GaN MEMS devices with power amplifiers, significantly saves area and enhances the performance of the front-end module.

Fig. 1.3 shows an example of a simple transmitter and the preferred integration boundary of the power amplifier with other front-end components. GaN monolithic microwave integrated circuits (MMICs) provide better performance in terms of power, radiation hardness, and operation temperature, leading to products that could be used in harsh environments. This work seeks to ideally implement the entire transmitter module with all-GaN MMICs/MEMS.

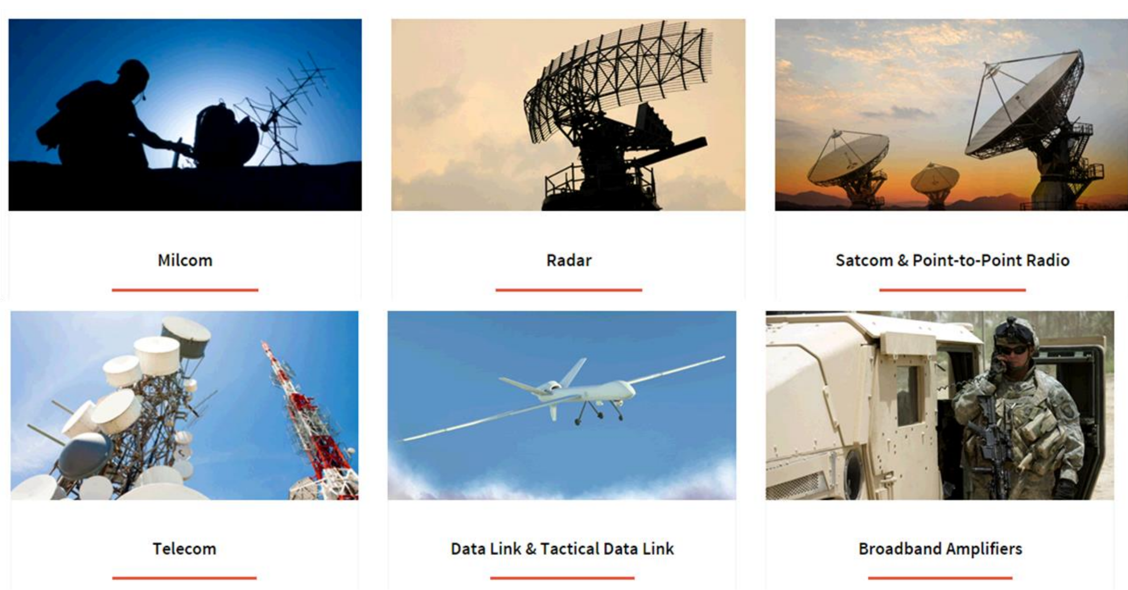

Figure 1.2 GaN HEMTs and power transistors find diverse applications in RF, microwave and satellite communication. Image taken from Cree (Wolf Speed) [1.3].

Popular in optoelectronics and power electronics, the electromechanical and acoustic properties of GaN have remained relatively unexplored. To fully unlock the potential of GaN, and add more functionalities to such a fast-growing technology, it is important to integrate diverse GaN-based acoustic devices on the same platform. Incorporating MEMS to GaN baseline foundry enhances the performance of GaN integrated microsystems in

many ways. For time-keeping applications, for instance, MEMS-based oscillators offer better phase noise and time jitter, and power handling, and can be designed to be temperature stable.

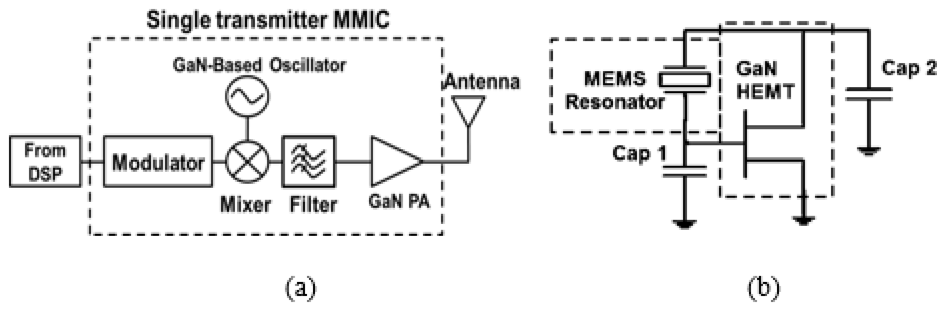

Figure 1.3 (a) A simplified schematic of a front-end transmitter based on all-GaN modules. (b) A schematic of a GaN MEMS/HEMT-based pierce oscillator.

As seen in Leeson's qualitative phase noise approximation (Eq. 1.1) [1.4], MEMS-based resonators with higher *Q*s and superior power handling capabilities (higher P_{sig}) can significantly reduce the phase noise of the oscillator,

$$L(\Delta w) = 10\log\ [\frac{2FKT}{P_{sig}}\{1+\left(\frac{\omega_0}{2Q\Delta\omega}\right)^2\}(1+\frac{\Delta\omega_{1/f3}}{|\Delta\omega|})], \qquad \text{(Equation 1.1)}$$

where L is the phase noise in a 1 Hz bandwidth at an offset angular frequency $\Delta\omega$ from the carrier angular frequency ω_0, F is the effective noise figure, K is the Boltzmann's constant, T is absolute temperature in Kelvin, Q is the quality factor of the resonator, P_{sig} is the signal power, and $\Delta\omega_{1/f3}$ is the corner frequency for the phase noise. Similarly, piezoelectric MEMS-based GaN oscillators can provide lower phase noise and precise frequency selectivity by incorporating GaN mechanical resonators. GaN MEMS-based oscillators can deliver large output powers and thus eliminate the need for an output power amplifier,

reducing the overall transmitter size. Therefore, it is desirable to build an all-GaN monolithically integrated piezoelectric MEMS-based HEMT oscillators.

1.2 Piezoelectric Transduction

Ever since its discovery by the Curie brothers in 1880's [1.5], piezoelectricity has been widely used for time keeping from Quartz crystals in wrist watches to surface acoustic wave (SAW) filters in cellphones [1.6] to miniaturized bulk acoustic wave (BAW) resonators [1.7] integrated with electronic circuitry in oscillator circuits. The application of piezoelectricity is not limited to time keeping; piezoelectric micro-machined ultrasound transducer (PMUTs) [1.8, 1.9], energy harvesters [1.10], sensors [1.11] (mass, gas, pressure, bio, *etc*.) and many other devices have been realized so far.

Piezoelectric materials are characterized by their ability to convert an applied mechanical force into an electrical signal or vice versa. When materials with a non-centrosymmetric crystal structure experience deformation under applied stress, they generate a net dipole potential leading to an electrically measureable potential at the output [1.12]. The basic constitutive equations for piezoelectricity can be written as,

$$T_{ij} = c_{ijkl}S_{kl} - e_{kij}E_k \ , \qquad \text{(Equation 1.2)}$$

$$D_k = e_{kij}S_{ij} + \epsilon_{ki}E_i \ , \qquad \text{(Equation 1.3)}$$

where

T_{ij} is the mechanical stress tensor ;

c_{ijkl}, are the coefficients of elasticity;

S_{kl} , is the strain tensor;

e_{kij} , is the piezoelectric stress tensor;

E_k , is the electric field tensor;

D_k , is the electric displacement vector;

ϵ_{ki} , is the dielectric constant tensor.

Materials with wurtzite crystal symmetry such as aluminum nitride (AlN) [1.13], zinc oxide (ZnO) [1.14], and GaN [1.15] have been successfully used to make microfabricated resonators. One of most successful device made from thin-film piezoelectric films integrated with CMOS circuitry is AlN film bulk acoustic resonator (FBAR) [1.16]. Piezoelectric transduction is very popular in the MEMS community compared to its capacitive, thermal, or magnetic counterparts. Ease of fabrication, linearity, and power handling, low motional impedance and operation without a bias voltage are among a few of its advantages.

Various resonance modes can be realized in piezoelectric resonators; length/width extensional resonance or thickness-extensional resonance modes are most common modes used throughout this dissertation. Such modes can be realized in thin film plates, where the resonance frequency can be estimated as:

$$frequency = \frac{n}{2L}\sqrt{\frac{E}{\rho}}, \qquad \text{(Equation 1.4)}$$

where *n* is the harmonic order, *L* (or *t*) is the critical material dimension based on the mode of resonance, *E* is the Young's modulus in a particular direction, and ρ is the resonant material density. COMSOL simulation of displacements of a fundamental length and thickness-extensional resonator are demonstrated in Fig. 1.4. While thickness-mode

resonators allow for scaling the resonance frequency to multi-GHz range, the contour-mode allows for achieving multiple resonance frequencies on the same wafer set by lithography.

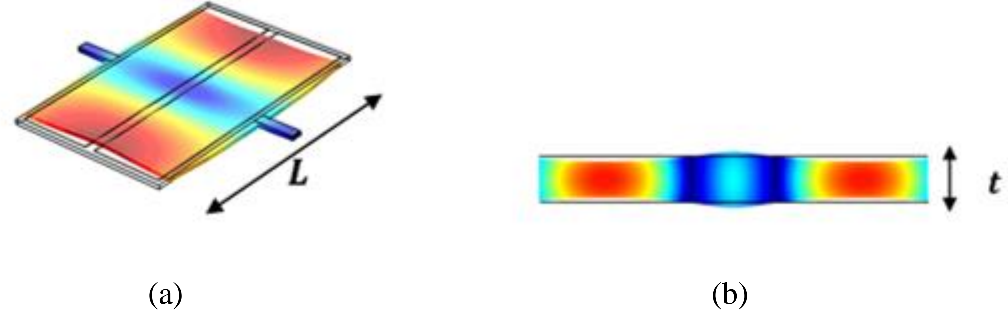

(a) (b)

Figure 1.4 COMSOL simulation of displacement of an exemplary resonator showing (a) fundamental length-extensional mode, (b) cross section of a thickness-extensional resonance mode.

Various metods have been utilized to electrically excite piezoelectric resonators. The most common is to sandwich a thin piezoelectric layer between a top and a bottom electrode. In case of GaN resonators, this is challenging as GaN cannot be directly grown on a metal layer and therefore the metal electrode has to be depositted from backside (more detailed discussion on this is included in Chapter 2). Lateral electric field excitation with the absense of a bottom electrode is easier in terms of fabrication and yields high *Q*s but low coupling coeffients. Thickness resonance modes cannot be sensed in such configurations. Embedded bottom electrodes are desirable in many cases owing to the freedom in placemnet of the bottom electrode for optimized transduction (Fig. 1.5.). In case of AlGaN/GaN heterosturectures, 2DEG can be used as an embedded bottom electrode, reducing the metal loading effect, but is unfortunately located only 20~30 nm below the AlGaN surface. Advances in growth technology can lead to GaN-based heterostrucure

stacks with multiple two dimensional electron (or hole) gas (2DEG or 2DHG) that could be accurately placed at locations of interest and thus siginificantly enhance the peformance of such resonators. In Chapter 2, we introduce novel growth techniques to realize an embedded bottom electrode for GaN-based resonators [1.17].

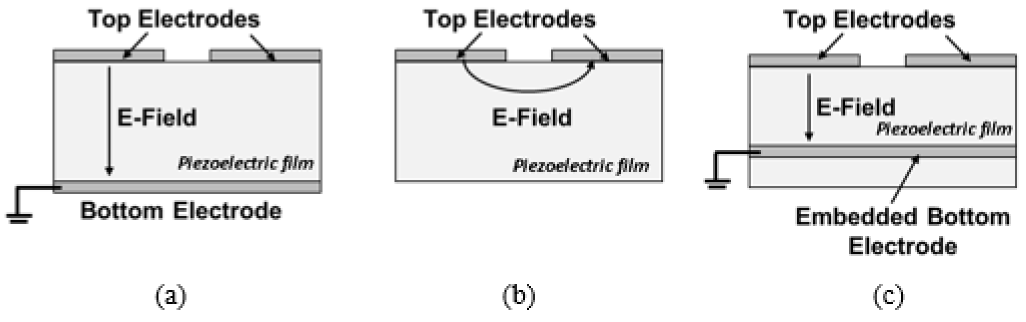

Figure 1.5 (a) Vertical electric field applied between the top and the bottom electrode, and (b) lateral electric field between two adjacent electrodes. (c) This work: electric field applied between the top electrode and an embedded bottom electrode.

1.3 Quality Factor and $f \times Q$ limits

One of the most important metrics for micromechanical resonators is the product of frequency and Q $(f \times Q)$. The Q of an acoustic resonator is defined as the ratio of the peak energy stored to energy lost per cycle of operation.

$$Q = 2\pi \frac{peak\ energy\ stored}{energy\ dissipated\ per\ cycle} \quad \text{(Equation 1.5)}$$

Various methods have been sought to estimate the Q of micromechanical resonators, Among them, 3-dB bandwidth, S_{21} phase ($\varphi(S_{21})$) slope and ring-down technique are the most popular. The first two methods will be used primarily throughout this dissertation.

$$Q = \frac{Resonance\ frequency\ (f_0)}{-3dB\ Bandwidth\ (BW)}. \qquad \text{(Equation 1.6)}$$

$$Q = \frac{f_s}{2}\frac{\partial\varphi(S_{21})}{\partial f}. \qquad \text{(Equation 1.7)}$$

The resonator Q determines the sharpness of the peak of the transfer function, which also determines the spectral purity of the oscillator built using this resonator. To design high-Q resonators, we first study the loss mechanisms that limit the Q of MEMS devices.

Quality factor of a resonator is defined by the dissipation mechanisms While extrinsic energy loss to the ambient media (damping and anchor loss) can be reduced by vacuum packaging and using a good design, energy lost as heat (thermoelastic damping), intrinsic energy losses to the material lattice (phonon-phonon loss), and energy lost to conduction electrons (phonon-electron loss) are considered the ultimate limiting factors of the resonator Q. $Q_{intrinsic}$ is described below.

$$\frac{1}{Q_{intrinsic}} = \frac{1}{Q_{TED}} + \frac{1}{Q_{phonon-phonon}} + \frac{1}{Q_{phonon-electron}} \qquad \text{(Equation 1.8)}$$

The measured values of the resonator $f \times Q$ are a good indicator of how close the resonator is to the limiting values. If the acoustic wave is considered as a strain wave in the material, at a frequency that is much lower than the inverse of the lattice relaxation time of the material crystalline structure, it is found theoretically that the product of frequency and the limiting material Q remains constant (across frequency) [1.18]. This is known as the Akhieser $f \times Q$ limit [1.18]. Above a certain frequency, the system can be treated as an ensemble of phonons and the limiting values of $f \times Q$ is given by the Landau–Rumer (L–R) regime [1.20]. For piezoelectric semiconductors, the electron scattering is also a

significant loss mechanism and is highly dependent on the free carrier concentration, the carrier mobility, and the coupling between the electrical and mechanical domains (due to piezoelectric or deformation potential coupling) [1.21]. Fig. 1.6 shows the Akhieser, L-R and TED limits for GaN-based resonators.

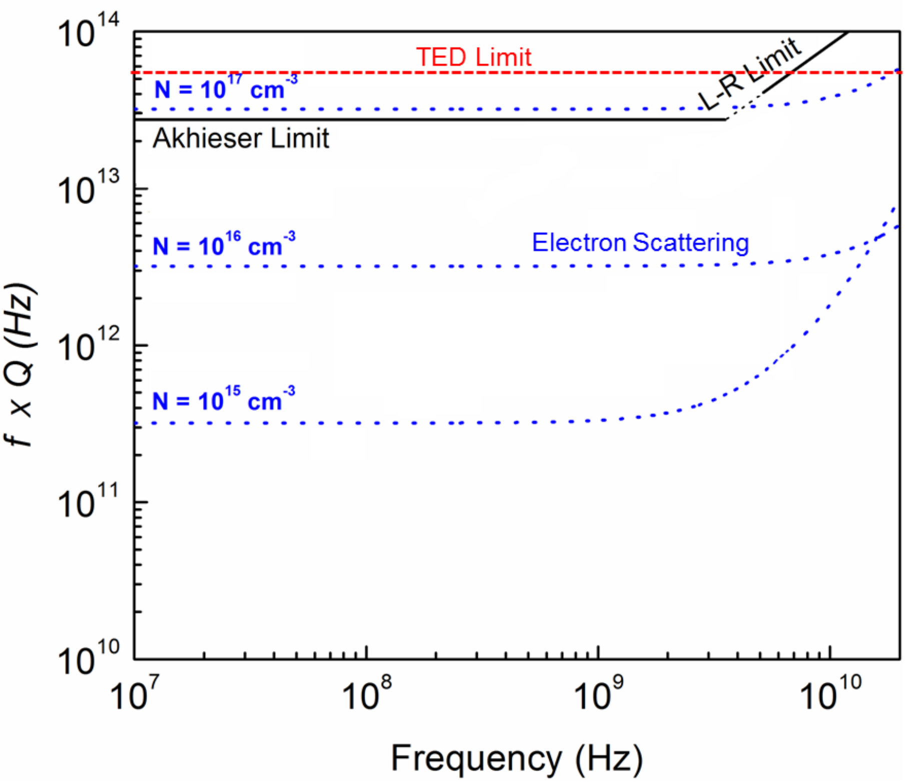

Figure 1.6 Theoretical $f \times Q$ limits of GaN showing Akhieser and L-R regime for phonon-phonon loss limit (black lines), phonon-electron loss limit at different carrier density levels (blue lines) and TED limit (red line) [1.15].

1.4 Coupling Efficiency and the $k_{eff}^2 \times Q$ Metric

The piezoelectric coupling coefficient k_t^2 is a material property that determines the efficiency of converting electrical energy into mechanical energy and vice-versa. It is defined as:

$$k_t^2 = \frac{U_{12}^2}{U_1 U_2}, \quad \text{(Equation 1.9)}$$

where U_1 and U_2 are the elastic and electric energy density, and U_{12} corresponds to the piezoelectric energy density. The intrinsic coupling coefficient depends on elastic, dielectric, and piezoelectric matrices for the target resonance mode [1.22]. For a longitudinal wave, with electric field applied in the z-direction, it can be simplified as:

$$k_t^2 = k_{3i}^2 \frac{d_{3i}^2}{\epsilon_{33}^T \epsilon_{ii}^E}, \quad \text{(Equation 1.10)}$$

where the wave can be launched in x, y, or z direction. The interplay between the mechanical and electrical domains can be taken into account as a change in the effective stiffness of the piezoelectric medium to form a modified Hooke's law as:

$$T = C_{eq} S, \quad \text{(Equation 1.11)}$$

$$C_{eq} = C(1 + k_t^2), \quad \text{(Equation 1.12)}$$

$$k_t^2 = \frac{e^2}{c\epsilon}, \quad \text{(Equation 1.13)}$$

For the various electromechanical axes of GaN, the values of k_t^2 range from 1.3% for in-plane modes to ~2% for thickness modes [1.23, 1.24]. The effective coupling coefficient k_{eff}^2 is extracted from the mechanical response of the resonators and includes the effects

of metal electrode loading, non-ideal electrode area coverage, anisotropic effects, and other non-idealities [1.24].

Another related metric that is used often for characterizing the applicability of a piezoelectric material for use in RF electromechanical filters is the $k_{eff}^2 \times Q$ product. A higher k_{eff}^2 increases the separation between the series and parallel resonances in a resonator. For coupled-resonator filter topologies, this higher separation implies a wider bandwidth. A higher Q (for each individual resonator) imparts a sharper roll-off for the filter. Thus, a high $k_{eff}^2 \times Q$ product is desirable for wide-band RF filters.

1.5 Temperature Coefficient of Frequency

One of the important metrics for resonator performance is the temperature coefficient of frequency (TCF), which describes the relative shift in the resonator frequency with temperature change. The TCF is a function of material properties, residual stress in the material layers, resonance mode, and dimensions of the device. In most materials, the dominant mechanism is the change in the elastic modulus of the material with respect to temperature, defined by temperature coefficient of elasticity (TCE). For many mechanical resonator applications, such as reference oscillators, clocks, and gyroscopes, the goal is to minimize the TCF in order to get temperature invariant performance. On the other hand, for thermal and infrared (IR) sensors [1.25], the temperature dependency should be maximized. In both cases, it is important to carefully characterize the TCF of the resonator. Theoretical calculations for the stiffness coefficients of GaN [1.26] indicate TCE values of

-50 ppm/K to -54 ppm/K for the longitudinal mode. The temperature-dependent resonance frequency of a MEMS resonators can be expressed in terms of the TCF by:

$$f(T) = f_0 \sum (TCF_n . (T - T_0)^n), \qquad \text{(Equation 1. 14)}$$

Where, n is the order of the approximation. Therefore, linear TCF can be approximated as:

$$TCF = \frac{1}{\Delta T}\frac{\Delta f}{f} = \frac{1}{2}TCE - \alpha, \qquad \text{(Equation 1. 15)}$$

where TCE is the thermal coefficient of the Young's modulus and α is the thermal expansion of coefficient, usually neglected compared to TCE [1.27]. However, in certain designs, the difference between the thermal expansion coefficients of various materials in the resonant stack and that of the substrate can become dominant in the TCF equation and utilized to compensate or increase the TCF value [1.28].

The temperature coefficients of stiffness matrix of Wurtzite GaN used in this work are extracted from [1.29] at room temperature and summarized below.

$$\mathrm{TC}_{11} = -37\ ^{\mathrm{ppm}}/_{\mathrm{k}}, \mathrm{TC}_{12} = -46\ ^{\mathrm{ppm}}/_{\mathrm{k}}, \mathrm{TC}_{33} = -47\ ^{\mathrm{ppm}}/_{\mathrm{k}}, \mathrm{TC}_{13} = -66\ ^{\mathrm{ppm}}/_{\mathrm{k}},$$

$$\mathrm{TC}_{44} = -16\ ^{\mathrm{ppm}}/_{\mathrm{k}}. \qquad \text{(Equation 1.16)}$$

It must be noted that the precise values of stiffness matrix and its temperature coefficients depend on the crystal quality, growth conditions, defect density, doping and *etc.* and may vary from wafer to wafer considering the current status of growth technology.

For GaN resonators, TCF values ranging from -14 ppm/K to -30 ppm/K [1.15] have been measured for different resonance modes. The variations in measured TCF arise from different AlN buffer layer thickness, with a higher TCE compared to GaN, as well as various TCE values of the metal electrodes used as the top/bottom electrode of the resonant

stack. Also, specific material properties in different stacks (*e.g.*, different level of doping for unintentionally doped GaN) and the mode of resonance can cause variations in measured TCF values.

1.6 Power Handling Capability

The ability to handle high power levels is an attractive feature of MEMS devices. Electromechanical devices, especially resonators, also have limiting values of input power that can be handled without distortion of the output due to the onset of electrical and mechanical non-linearity. In piezoelectric resonators, mechanical non-linearity is primarily due to the non-linearity in the elastic coefficients of the material (especially for the suspension tethers). Popular methods for characterizing the non-linearity and distortion of mechanical resonators associated with high input power levels are third order intercept point (IIP_3) and 1-dB power compression point ($P_{1\text{-dB}}$). Extrapolated IIP_3 values in excess of +32 dBm, and $P_{1\text{-dB}}$ values of ~20 dBm [1.30] have been reported for GaN resonators.

1.7 Research Objectives & Contributions

This work aims at building an all-GaN monolithically integrated RF module that would save area, add power density, and operate at high frequencies with lower noise. A schematic of a front-end module with future GaN-based electro-acoustic devices such as circulators are highlighted.

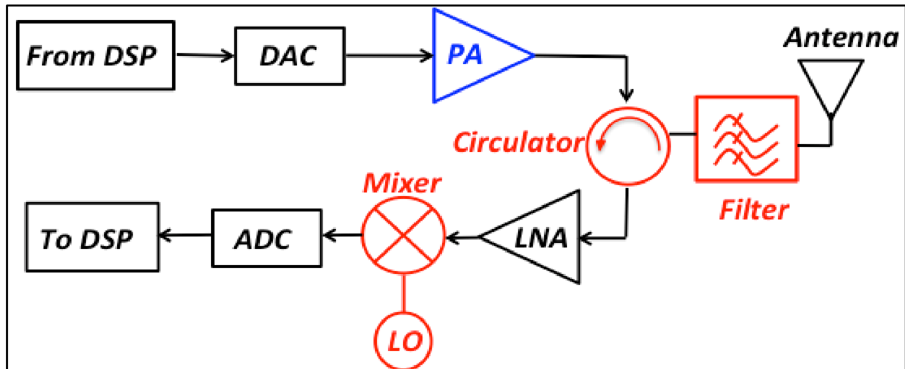

Figure 1.7 A simple schematic of an RF transceiver module. GaN power amplifiers (PAs) are already being used in base stations. Future direction of research on GaN includes realization of novel electroacoustic devices (e.g. acoustic circulators), and integration of all GaN components to build an integrated GaN MMIC transceiver module.

In summary, my research contributions include:

- Design and fabrication of the first GaN-on-Si micromechanical resonators and filters, exhibiting high $f\times Q$ values (1.5×10^{12}), high power handling capabilities (> 20 dBm), and relatively large electro-mechanical coupling coefficient (k_t^2~ 1.7%).
- Implementation of the first hybrid GaN MEMS-HEMT platform showing intimate integration of GaN MEMS resonators and GaN HEMTs by cascading a bulk acoustic resonator with a 2-fingered HEMT, enabling more than 30 dB of signal tuning with changing the DC voltage applied to the HEMT.
- Development of the first thickness-mode “Resonant Body HEMT” (RB-HEMT) by taking advantage of combined benefits of piezoelectric and semiconducting properties of GaN. The thickness-mode RB-HEMT shows a second-order thickness-mode resonance frequency of 4.2 GHz, with a Q of 250 and an acoustic transconductance (g_a) of up to 25 µS.

- Design and fabrication of the highest resonance frequency measured to-date on GaN bulk-mode resonators. A *Q* of 330 is achieved at 8.7 GHz corresponding to the fourth-order thickness-mode resonance.
- Demonstration of the first temperature-compensated GaN MEMS resonator, by depositing the silicon dioxide passivation layer on the resonator. The TCF is reduced to half of its original value.
- Developing novel growth techniques to form vertical metal-GaN-metal structures desirable in temperature compensated GaN-based resonators and filters.
- Using depletion forces in AlGaN/GaN heterostructures to enhance the *Q* beyond that of purely piezoelectric resonator.
- Combination of depletion-mediated piezoelectric force with phonon trap designs that have yielded the highest *Q* measured to date (~13,000) at 740 MHz corresponding to the ninth-order width extensional resonance mode.
- Implementation of resonant HEMT, placed in the middle of the acoustic cavity to accurately sense the strain. Such resonant HEMT can be used for precise temperature sensing. By tailoring the DC current, the temperature-induced frequency shifts can be compensated and such a system can provide an ovenized platform for temperature-stable frequency reference applications.

5.1 Organization of Thesis

Chapter 1 was focused on the motivation of this work, particularly what GaN acoustic devices can add to GaN integrated microsystems. Also, piezoelectric transduction

mechanism and the figures of merit of MEMS resonators, used in later chapters, were summarized.

In Chapter 2, electro-mechanical material properties of GaN are summarized that are useful to design GaN MEMS, HEMTs, and resonant HEMTs. The growth procedure of GaN on Si (111) substrate is briefly explained and the fabrication process of suspended GaN membranes, co-fabricated with AlGaN/GaN HEMTs is presented. A novel growth technique to realize vertical metal-GaN-metal structures is presented and the fabrication challenges of suspended GaN structures as well as the challenges arising from the uncertainties in electro-mechanical properties of GaN are discussed.

Chapters 3-5 are focused on GaN-based acoustoelectric devices as summarized by Fig. 1.8, and their combination with HEMTs and 2DEG sensing. More specifically, Chapter 3 is focused on the design and characterization of passive bulk-mode GaN-on-Si and GaN MEMS resonators and filters. The resonant stack is essentially made of thin GaN film sandwiched between a top and a bottom metal electrode. High performance, length-extensional and multi-GHz thickness-extensional resonators realized in GaN are characterized.

In Chapter 4, results of intimate integration of bulk-mode GaN MEMS with AlGaN/GaN HEMTs are presented. Then, a multi-GHz resonant body HEMT is presented, which combines the frequency selectivity of a MEMS resonator with the amplification of HEMT in a single device. Such a device is a great candidate to be used in oscillator circuits.

In Chapter 5, a new set of devices, depletion-mediated piezoelectric AlGaN/GaN resonators, are presented, where the 2DEG carrier density is modulated and depletion

forces are added to the piezoelectric force. Q-amplification is achieved by modulating the carrier density of 2DEG. Dispersion curves are used to engineer the geometry of the acoustic cavity to ensure acoustic energy is concentrated in the center of the device and thus highest value of the Q is achieved without the need for narrow tethers. Finally, a resonant HEMT is realized by placing the HEMT in the middle of the acoustic cavity to sense the strain. We show that such resonant HEMT can be used as temperature sensors of the HEMT channel, as well as thermal oscillators.

Finally, Chapter 6 concludes this thesis work, showing the big pictures, and presents a few of many exciting future research directions of GaN electro-acoustic devices and integrated microsystems.

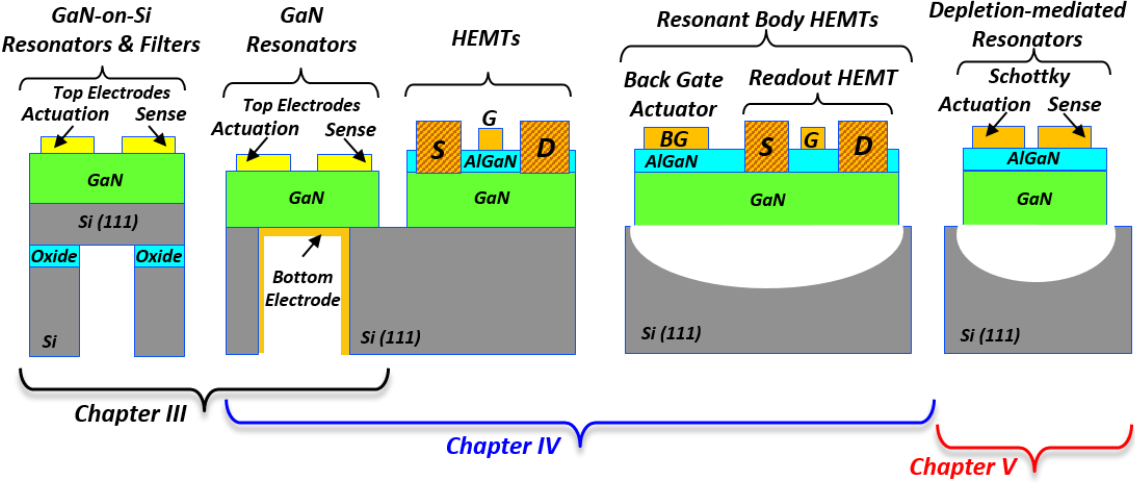

Figure 1.8 A simplified cross section schematic of my thesis organization with a single device representing the main idea in each chapter. Chapter 2 involves the growth and fabrication of such structures.

Chapter 1: References

[1.1] W. Arden *et al.*, "More than Moore" White Paper*, International Technology Roadmap for Semiconductors,* 2010.

[1.2] C. Sanabria, "Noise of AlGaN/GaN HEMTs and Oscillators," *Thesis Dissertation*, June 2006.

[1.3] "http://www.wolfspeed.com/rf/applications," [Online]. Accessed July 19, 2016.

[1.4] D. Leeson, "A Simple Model of Feedback Oscillator Noise Spectrum," *Proc. IEEE*, Vol. 54, No. 2, pp. 329–330, Feb. 1966.

[1.5] P. Curie & J. Curie, C. R. Acad. Sci. 91, 294, 1880.

[1.6] M. White and F. W. Voltmer, "Direct Piezoelectric Coupling to Surface Elastic Waves," *Applied Physics Letters*, vol. 7, pp. 314-&, 1965.

[1.7] R. C. Ruby, P. Bradley, Y. Oshmyansky, A. Chien, and J. D. Larson, "Thin film bulk wave acoustic resonators (FBAR) for wireless applications," *IEEE Ultrasonics Symposium Proceedings*, Vols 1 and 2, pp. 813-821, 2001.

[1.8] A. Guedes, S. Shelton, R. Przybyla, I. Izyumin, B. Boser, and D. A. Horsley, "Aluminum nitride pMUT based on a flexurally-suspended membrane," in *International Solid-State Sensors, Actuators and Microsystems Conference (Transducers)*, 2011, pp. 2062-2065.

[1.9] P. Muralt and J. Baborowski, "Micromachined Ultrasonic Transducers and Acoustic Sensors Based on Piezoelectric Thin Films," *Journal of Electroceramics*, Vol. 12, No. 1-2, pp. 101-108, 2004.

[1.10] P. Muralt, R.G. Polcawich, and S. Trolier-McKinstry. "Piezoelectric thin films for sensors, actuators, and energy harvesting," MRS bulletin, 34(09):658-664, 20.

[1.11] G. Gautschi. "Piezoelectric sensorics: force, strain, pressure, acceleration and acoustic emission sensors, materials and amplifiers," Springer, 2002.

[1.12] J. Yang, "An Introduction to the Theory of Piezoelectricity," Springer US, 2005.

[1.13] G. Piazza, R. Abdolvand, G. Ho and F. Ayazi, "Piezoelectrically-transduced, capacitively-tuned, high-Q single-crystal silicon micromechanical resonators on SOI wafers*,*" *Sensors and Actuators* A, vol. 111, no. 1, pp. 71-78, 2004.

[1.14] V. Thakar, Z. Wu, A. Peczalski and M. Rais-Zadeh, "Piezoelectrically transduced temperature-compensated flexural-mode silicon resonators," *IEEE/ASME Journal of Microelectromechanical Systems (JMEMS),* vol. 22, no. 3, pp. 819-823, 2013.

[1.15] M. Rais-Zadeh *et al.*, "GaN as an electromechanical material," *IEEE Journal of Micro-electro-mechanical Systems*, Vol. 23, No. 6, pp. 1252–1271, December, 2014.

[1.16] D. Moy, "Avago Technologies' FBAR filter technology designed into latest generation of 4G and LTE Smartphones," [Online]. Available: www. avagotech.com/fbar.

[1.17] A. Ansari, C.-Y. Liu, C.-C. Lin, H.-C. Kuo, P.-C. Ku, and M. Rais-Zadeh, "GaN micromechanical resonators with meshed metal bottom electrode," *Materials*, 8(3), pp. 1204–1212, 2015.

[1.18] R. Tabrizian, M. Rais-Zadeh, and F. Ayazi, "Effect of phonon interactions on limiting the f.Q product of micromechanical resonators," *Solid-State Sensors, Actuators and Microsystems (Transducers)*, Denver, CO, pp. 2131-2134, June, 2009.

[1.19] A. Akhieser, "On the absorption of sound in solids," *Journal of Physics, Academy of Sciences USSR,* Vol. 1, No. 4, pp. 277-287, 1939.

[1.20] L. Landau and G. Rumer, "über schallabsorption in festen körpern," in Collected papers of L. D. Landau, D. T. Harr, Ed., 1967, pp. 187-192.

[1.21] M. Pomerantz, "Ultrasonic Loss and Gain Mechanisms in Semiconductors," *Proceedings of the IEEE*, Vol. 53, No. 10, pp. 1438-1451, 1965.

[1.22] "IRE Standards on Piezoelectric Crystals: Determination of the Elastic, Piezoelectric, and Dielectric Constants-The Electromechanical Coupling Factor, 1958". *Proceedings of the IRE*, 46(4):764-778, April 1958.

[1.23] V. Siklitsky. (1998). Semiconductors on NSM-Gallium Nitride (1998 ed.). Available: http://www.ioffe.ru/SVA/NSM/. Accessed on July 19, 2016.

[1.24] J. Kaitila, "BAW Device Basics," in *RF Bulk Acoustic Wave Filters for Communications*, K.-y. Hashimoto, Ed., ed Norwood, MA: Artech House, 2009, pp. 51-90.

[1.25] V. J. Gokhale and M. Rais-Zadeh, "Uncooled Infrared Detectors Using Gallium Nitride on Silicon Micromechanical Resonators," *IEEE/ASME Journal of Microelectromechanical Systems (JMEMS)*, ol. 23, No. 4, pp. 803 - 810, 2013.

[1.26] R. Ram Yadav and D. Kumar Pandey, "Ultrasonic characterisation of gallium nitride," *Materials Research Innovations*, Vol. 10, No. 4, pp. 402-407, 2006.

[1.27] R. Tabrizian, G. Casinovi and F. Ayazi, "Temperature-Stable Silicon Oxide Micromechanical Resonators," *IEEE Transactions on Electron Devices*, Vol. 60, No. 8, Aug. 2013 pp. 2656-63.

[1.28] W-T Hsu, J. R. Clark, and C. T.-C. Nguyen, "Mechanically Temperature-Compensated Flexural-Mode Micromechanical Resonators," *IEEE Electron Device Meeting (IEDM),* San Francisco, California, Dec. 11-13, 2000, pp. 399-402.

[1.29] M. Edwards, "Temperature dependent properties of GaN," University of Bath (UoB), *MorGaN Report*, Feb. 2009.

[1.30] A. Ansari and M. Rais-Zadeh, "A temperature-compensated micromechanical gallium nitride resonator," *IEEE Electron Device Letters*, vol. 35, no. 11, pp.1127–1129.

Chapter 2 Electromechanical Material Properties and Process Technology of Gallium Nitride Thin Films

In this chapter, various electromechanical properties of GaN, useful for designing GaN MEMS, HEMTs, and novel electro-acoustic devices are investigated. Epitaxial growth of GaN on Si (111) by metal-organic chemical vapor deposition (MOCVD), fabrication techniques used to build AlGaN/GaN as well as GaN suspended structures are presented. In addition, current challenges in material growth, fabrication and characterization of GaN thin films are discussed and future research directions to mitigate such issues are touched upon. Using the fabrication techniques discussed in this chapter, GaN MEMS and acoustic devices can be co-fabricated with AlGaN/GaN HEMTs with only an additional release step that is used to selectively remove the silicon substrate and form suspended structures. Finally, a novel vertical metal-GaN-metal structure is presented that is used as the resonating stack and is based on lateral regrowth of GaN on a meshed metal electrode. The meshed metal electrode is coated with a thin silicon dioxide layer. Such configuration not only allows for accurate control over the placement of the bottom electrode, but can also be used to build temperature compensated resonators by leveraging the opposite frequency-temperature trends of silicon dioxide and GaN.

2.1 Motivation, background and Challenges

Over the past decade, GaN has become one of the most popular semiconductor materials [2.1-3]. Similar to any other growing industry, advancements in material science and growth technology have aided the rapid improvements in GaN processing techniques, with consistent improvement in wafer size, material quality, diversification of epitaxial substrate material, and ease of market access [2.4]. While the current cost of GaN substrates is still high, high-volume production of GaN wafers is expected to reduce the wafer cost to the same level as GaAs substrates. In addition, epitaxial growth of high-quality GaN on low-cost substrates, such as Si, is becoming more mature, resulting in availability of 6-inch GaN on Si substrates nowadays.

The prime movers behind the growth of GaN semiconductor industry have been optoelectronics, power electronics and radio-frequency (RF) electronics. While a significant amount of scientific research has been devoted to these applications, little attention has been directed to the use of GaN for nano and micro-electro-mechanical systems (N/MEMS). Unlike Si, GaN is a piezoelectric semiconductor and one can envision using the piezoelectric properties of GaN to manufacture multitude of devices for diverse applications, as will be discussed in this thesis.

However, the fabrication of suspended GaN membranes as well as precise control over the design of GaN MEMS-based devices is quite challenging. The device performance is heavily dependent on the growth conditions, which impacts (1) the epitaxial stack thickness and composition; GaN growers tend to choose different AlN/GaN compositions as the nucleation/buffer layers, while the Al and Ga mole fraction and the transition from AlN to

GaN is usually not very clear. Such uncertainty impacts the effective Young's modulus and material density of the AlN/GaN resonant stack. (2) Dislocation density consisting of screw and edge-type dislocations; it is known that screw-type dislocations do not create electric fields due to their zero divergence and thus do not contribute to changing the thin film polarization, however edge dislocations have non-zero divergence at the interface, which can create electric fields that impact the film polarization [2.5]. (3) Doping concentration, GaN thin films are normally unintentionally doped with n-type conductivity and the doping level may vary in different samples, this impacts the stress level in GaN thin films. Furthermore, the variable conductivity in GaN films affect the acoustic wave propagation and piezoelectricity of GaN thin films. (4) Residual stress that is affected by the thickness of the stack as well as the doping dislocation density. The residual stress shifts the resonance frequency, changes the temperature coefficient of frequency as well as the yield of suspended membranes.

Moreover, material properties of GaN are still not well-characterized, thus significant effort was put into extracting electromechanical properties of GaN from fabricated test structures which were subsequently used in simulation tools to precisely model the resonator performance. Such challenges can be mitigated by advancements in growth or deposition technologies of thin films which in turn paves the way for advancements in design and fabrication of GaN N/MEMS devices.

In this chapter a selection of some of the pertinent material properties and figures of merit (FOM) of GaN is compared with a selection of other commonly used electromechanical materials. Furthermore, various growth and fabrication techniques

suitable for building GaN suspended structures are discussed, highlighting their challenges and advantages.

TABLE I [2.4]
PROPERTIES OF A SELECTION OF ELECTROMECHANICAL MATERIALS

Material	**Elastic Modulus** c_{33} **(GPa)**	**Acoustic Velocity (m/s)**	**Piezoelectric Coefficient** e_{33} **(Cm^{-2})**	$f \times Q$ * **(Hz)**	k^2_{eff} **(%)**
Si	165	8415	*N/A*	2.5×10^{13}	*N/A*
SiC	605	13100	+0.2	3.5×10^{14}	0.08
GaAs	118	2470	-0.16	-- †	0.04
AlN	390	11000	+1.55	10^{13}	5.6
Sc doped AlN	244	8509	+3.9	3×10^{11}	15.5
$LiNbO_3$ (X-cut,)‡	60	3900	+3.65	7.7×10^{11} (measured)	16
GaN	398	8044	+0.65	2.5×10^{13} (theory)	2

* For anharmonic phonon scattering in Akhieser regime
† Data not available
‡ $LiNbO_3$ data are for shear mode, not longitudinal mode

2.2 Electro-mechanical Properties of GaN

Here, a summary of a few of the important electromechanical material properties of GaN, useful for designing N/MEMS structures, is provided.

2.2.1 Mechanical Properties of GaN

The mass density of GaN has been quoted in the literature as 6150 kg/m^3 [2.2]. Due to its hexagonal nature, the elastic properties of Wurtzite GaN are symmetric along the in-plane vectors. The full stiffness matrix for GaN [2.6] is given by Eq. 2.1 as:

$$C_{ij=} \begin{pmatrix} 390 \pm 25 & 145 \pm 20 & 106 \pm 20 & 0 & 0 & 0 \\ 145 \pm 20 & 390 \pm 15 & 106 \pm 20 & 0 & 0 & 0 \\ 106 \pm 20 & 106 \pm 20 & 398 \pm 20 & 0 & 0 & 0 \\ 0 & 0 & 0 & 105 \pm 10 & 0 & 0 \\ 0 & 0 & 0 & 0 & 105 \pm 10 & 0 \\ 0 & 0 & 0 & 0 & 0 & 122.5 \pm 20 \end{pmatrix} GPa$$

Equation (2.1)

The elastic compliance and constants for the binary compounds, the rule to obtain the values for alloys, and the Knoop hardness of GaN are summarized by Ambacher *et al.* [2.2] and agrees well with experimental data obtained for GaN-on-Si samples used in this work.

2.2.2 Piezoelectric and Acoustic Properties of GaN

The use of GaN as an electromechanical material is predicated on its piezoelectric properties. Piezoelectric actuation can be used for both static as well as dynamic actuation/sensing, with frequencies as high as tens of GHz. As a piezoelectrically actuated vibrating or resonant system, GaN has the advantage of high coupling efficiency compared to similar devices using capacitive, thermal, or magnetic actuation. The piezoelectric coefficients of Wurtzite GaN have been reported by [2.7-8] to be:

$$e_{ij} = \begin{pmatrix} 0 & 0 & 0 & 0 & -0.3 & 0 \\ 0 & 0 & 0 & -0.3 & 0 & 0 \\ -0.49 & -0.49 & +0.73 & 0 & 0 & 0 \end{pmatrix} Cm^{-2} \qquad \text{(Equation 2.2)}$$

Piezoelectric polarization in w-GaN can be calculated as [2.9]:

$$P_{PE} = e_{33}\varepsilon_z + e_{31}(\varepsilon_x + \varepsilon_y) \qquad \text{(Equation 2.3)}$$

$$\varepsilon_z = {(c - c_0)}/{c_0} \qquad \text{(Equation 2.4)}$$

$$\varepsilon_x = \varepsilon_y = {(a - a_0)}/{a_0} \qquad \text{(Equation 2.5)}$$

Since $\varepsilon_z = -2\frac{C_{13}}{C_{33}}\varepsilon_x$, therefore,

$$P_{PE} = 2\frac{(a-a_0)}{a_0}\left(e_{31} - e_{33}\frac{C_{13}}{C_{33}}\right), \quad \text{(Equation 2.6)}$$

where $e_{33}$and e_{31} are the piezoelectric coefficients of GaN, $\varepsilon_x, \varepsilon_y$, and ε_z are the in-plane and out-of plane strain. a_0 and c_0 are the lattice constants under no strain and a and c are the lattice constants when the lattice is under stress. C_{13} and $C_{33}$are in-plane and c-plane GaN stiffness components.

The velocity of longitudinal acoustic wave in GaN is expected to be ~7960 m/s for in-plane modes and ~8044 m/s along the c-axis [2.4].

2.2.3 Thermal Properties of GaN

The thermal conductivity of GaN is highly dependent on the film quality, the concentration and type of impurities and defects and the temperature of operation. Experimental results for thermal conductivity of GaN indicate that the room temperature values for thermal conductivity are within the range of 100 W/m-K to 250 W/m-K [2.10-12]. The specific heat capacity of GaN is in the range of 300 J/kg-K to 500 J/kg-K at room temperature [2.11-12]. GaN coefficient of thermal expansion (β) is on the order of 3×10^{-6} K^{-1} along the c-axis, and in the range of 3.8×10^{-6} K^{-1} to 5.6×10^{-6} K^{-1} in-plane [2.13-14].

The temperature coefficients of Young's modulus of GaN play an important role in determining the temperature trends of the resonance frequency of GaN micromechanical devices. Fig. 2.3. summarizes the temperature trends of C_{33}, C_{11}, C_{12}, C_{13}, and C_{44} stiffness matrix of Wurtzite GaN based on [2.15].

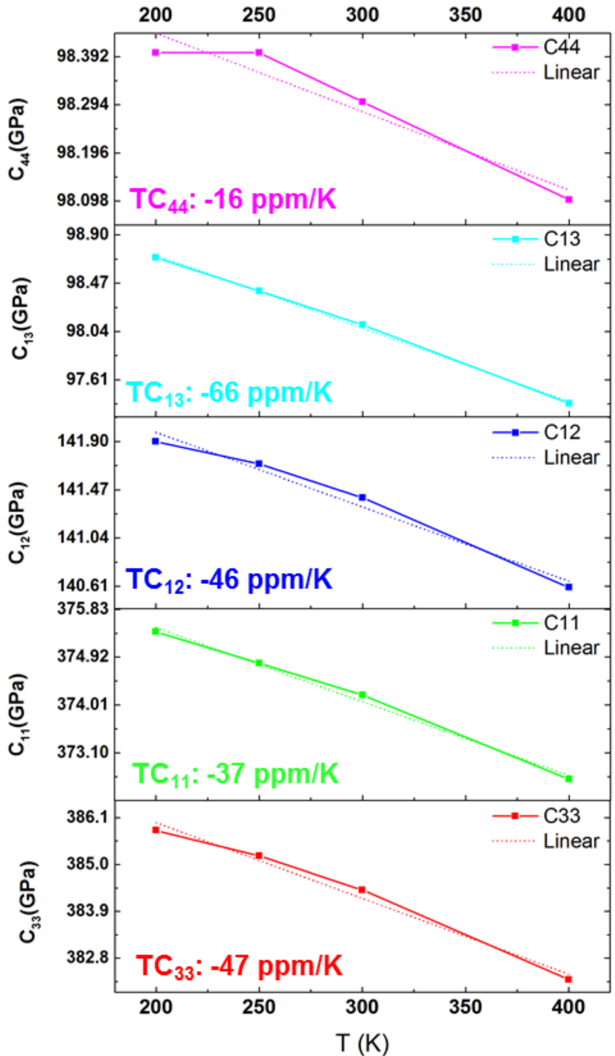

Figure 2.1 GaN stiffness matrix components *vs.* temperature. Temperature coefficient of stiffness components are extracted for C_{11}, C_{33}, C_{12}, C_{13} and C_{44} for GaN Wurtzite crystalline structure.

2.2.4 Electrical Properties of GaN

Extensive research has been recently conducted on compound semiconductor materials, motivated by their superior material properties as compared to Si. GaN, as the second most popular semiconductor, with a bandgap energy of E_g= 3.4 eV at room temperature, offers high breakdown electric field, high thermal conductivity, high peak

velocity, and high saturation velocity. Further contributing to the outstanding material properties of GaN, is the ability to achieve two-dimensional electron gases (2DEG) with sheet carrier concentrations of more than 10^{13} cm^{-2} and high electron mobility of more than 2000 $cm^2/V\text{-}s$ at AlGaN/GaN hetero-interface without intentional doping. Table II compares the electrical properties of GaN with a few conventional semiconductors [2.4].

TABLE II
ELECTRICAL PROPERTIES OF GAN

Properties	Si	GaAs	SiC	GaN
μ (electron mobility) ($cm^2/V\text{-}sec$)	1400	10^{4}*	800	2000*
E_g (bandgap) (eV)	1.1	1.4	3.26	3.4
E_{br} (breakdown field) (MV/cm)	0.3	0.4	3.5	3.3
Dielectric Constant (Static)	11.5	12.9	9.7	8.9
V_{sat} (Saturation velocity) ($\times 10^7$cm/s)	1.0	1.5	2	2.5
n_s (density) ($\times 10^{12}cm^{-2}$)	<1	~1*	-	15*
T_{max} (°C)	300	300	600	700

* Measured values of the corresponding hetero-structure.

** Measured value at E= 500 KV/cm.

*** Reported values are normalized to Si.

2.3 Crystallinity of GaN on Si

A wide range of techniques have been used to epitaxially grow thin-film GaN on a substrate, such as molecular beam epitaxy (MBE), metal organic chemical vapor deposition (MOCVD), and hybrid vapor phase epitaxy (HVPE). A variety of substrates such as Si, silicon carbide (SiC), and sapphire have been used for these studies [2.2]. In this work, we focus on properties of Wurtzite GaN grown on Si (111) substrate by MOCVD. Besides being relatively cost-effective, GaN-on-Si substrates are attractive candidates for GaN MEMS, since Si can be selectively removed underneath GaN to form thin suspended GaN

membranes. Integration of GaN components on Si is also desirable since it allows for future integration with CMOS circuitry and Si-based large scale integrated circuits.

GaN in its Wurtzite crystal structure offers piezoelectric as well as spontaneous polarization. GaN crystal structure has polar bonds and lacks inversion symmetry. The lattice parameters are $a = 3.189$ Å and $c = 5.185$ Å. The $^{c}/_{a}$ ratio of 1.6259 [2.9] is deviated enough from the ideal 1.633 ratio to give rise to spontaneous polarization in unstrained GaN lattice (Fig. 2.1).

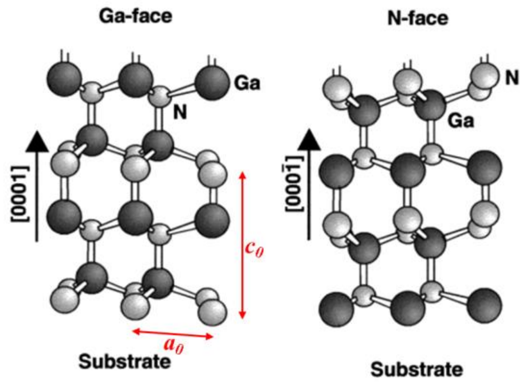

Figure 2.2 Ga-face and N-face crystal structure of GaN.GaN thin films grown by MOCVD yield Ga-face, whereas MBE-grown GaN yields a N-face crystalline structure [2.9].

A figure of merit that is commonly used to characterize the crystalline quality of an epitaxially grown thin film is the Full Width at Half Maximum (FWHM) acquired using X-Ray Diffraction (XRD) analysis. A narrow FWHM denotes high long-range crystalline order and good internal alignment of the crystal (Fig. 2.2). To achieve good FWHM values for GaN-on-Si, it is often necessary to grow a thin layer of AlN or a graded AlN/AlGaN buffer layer to avoid chemical reactions between gallium and silicon and to accommodate the lattice mismatch between the substrate and the epitaxial GaN.

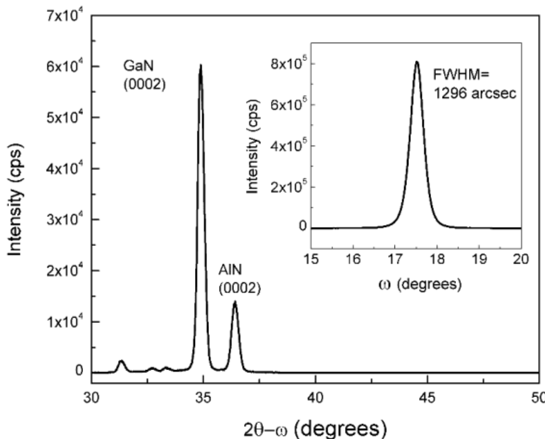

Figure 2.3 XRD spectroscopy on a GaN thin film grown on a Si (111) substrate using metal-organic chemical vapor deposition (MOCVD). Inset: Rocking curve of the (0002) GaN plane exhibits a very clear peak and a FWHM of 1296 arcsec [2.4].

There are numerous studies on the epitaxial growth techniques and optimization of GaN MBE, MOVPE/MOCVD, and more recently HVPE are the most common techniques for the growth of GaN on Si [2.4]. The threading defects in GaN are dislocation lines normally oriented parallel to the *c*-axis of the material, with reported densities of 10^8~10^{11} cm^{-2}. Pure screw-type threading dislocation densities of less than 10^7 cm^{-2} can be obtained for GaN-on-Si substrates. Edge type dislocations and point defects can become charged and act as centers of Coulomb scattering, whereas screw-type dislocations have been reported to cause electrical leakage, causing degradation in electric and optoelectronic performance as well as long-term reliability [2.17-18]. However, the measured acoustic properties of GaN suggest that the issue is less significant in the case of mechanical and acoustic properties of GaN.

This work is focused on GaN thin films grown on Si substrates. The majority of GaN-on-Si substrate used in this work, were grown by our collaborators at Nitronex Corporation (now MACOM) using MOCVD technique. Fig. 2.4 demonstrates the HEMT epi-layer

grown on Si and used in this work, highlighting the 2DEG at the AlGaN/GaN hetero-interface. GaN-on-SOI (stack shown in Fig. 2.5) is also grown by Nitronex Corporation and used to build various electro-acoustic devices described in detail in the following chapters.

Growth of high quality GaN on Si (111) can be achieved by addressing the significant levels of lattice misfit (~17%) and thermal expansion coefficient (~ 56%) mismatch. An initial layer of aluminum nitride (AlN) is deposited on the Si substrate to accommodate the strain associated to the differences between crystal properties of Si and GaN. The transition layer addresses the two challenges necessary for the successful growth of GaN on Si: It manages both the lattice and the thermal mismatch between the two materials. The AlN/Si interface absorbs most of the lattice mismatch while the (Al, Ga) N transition layer is successful in absorbing the stresses that arise due to the mismatch of thermal expansion coefficients [2.19].

The screw dislocation density measured on the samples used in this work are in the range of ~10^7 cm^{-2}. This was characterized by using KOH solution. The wafers were immersed in KOH solution, where the defects get etched faster due to having multiple facets exposed. The measured value agrees well with the numbers reported by our vendors.

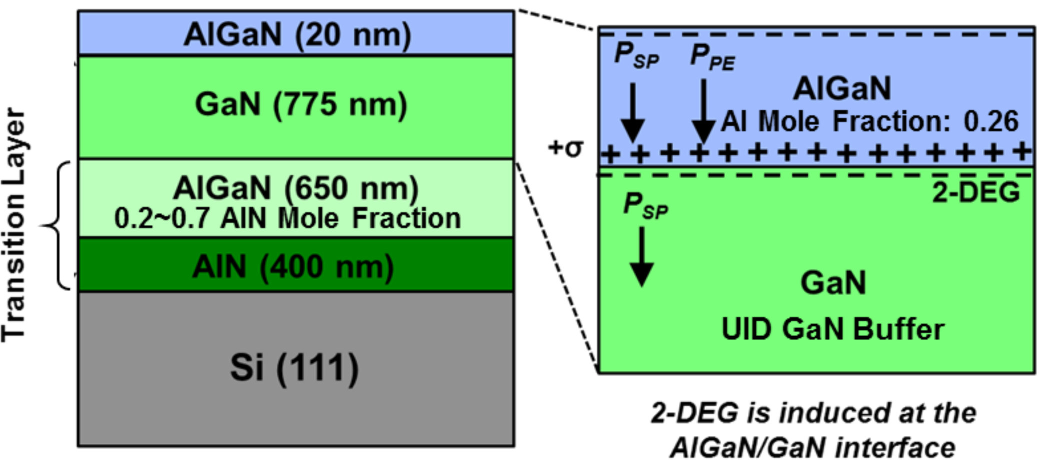

Figure 2.4 Schematic of the epi-stack of MOCVD-grown AlGaN/GaN heterostructure on Si (111) by Nitronex Corporation. The thickness of the transition and buffer layers are indicated. 2DEG is induced at the AlGaN/GaN interface due to spontaneous and piezoelectric polarization. The peak charge concentration of 2DEG measured with Hg probe CV measurements is 3×10^{19} cm^{-3} concentrated at an average peak distance of ~190 Å from the AlGaN surface.

2.4 GaN-on-SOI Epitaxial Growth

The epitaxial GaN layer was grown on a 100 mm diameter silicon-on-insulators (SOI) wafer in a custom-built, cold-wall, rotating disc metalorganic chemical vapor deposition (MOCVD) reactor at nominal temperature of 1020 ºC. The SOI substrate consisted of a 2 µm thick buried silicon dioxide layer and a 10 µm thick p-type (0.001-0.01 Ω.cm) Si (111) device layer (miscut angle ±0.5°). For the MOCVD growths, trimethylgallium (TMG) and trimethylaluminum (TMA) precursors were carried by Pd-diffused hydrogen, and ammonia (NH3) was used as the N precursor. The full epitaxial stack consists of an AlN nucleation layer, two AlGaN layers, and a ~0.75 µm thick GaN buffer layer (Fig. 2.5). The total thickness of the epi-layer is 1.43 µm [2.20].

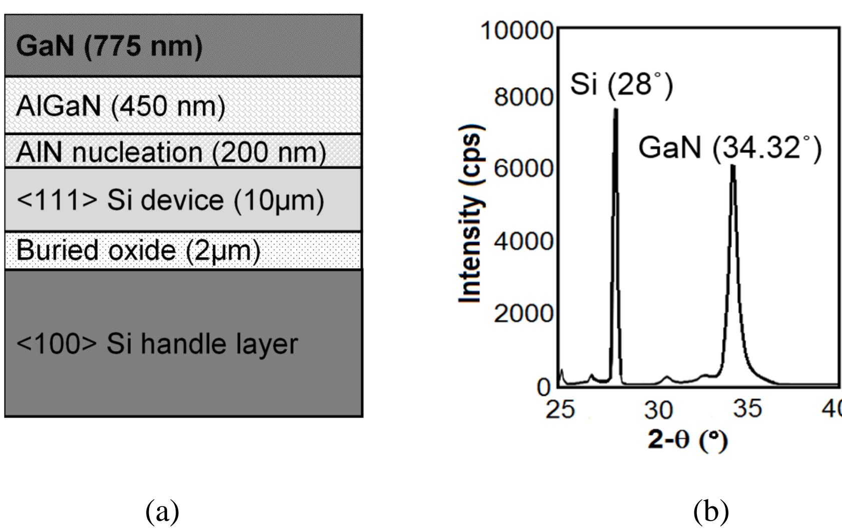

(a) (b)

Figure 2.5 (a) GaN-on-SOI wafer stack and (b) XRD of the thin film GaN layer showing an FWHM of 0.535˚ [2.20].

2.5 Fabrication of GaN MEMS

2.5.1 Suspended GaN membranes

GaN in particular and group III-nitrides in general are notable for their excellent chemical stability as characterized by their invulnerabilities to wet etching. No wet etching technique has been reported to date for effective removal of single crystalline GaN. To realize suspended microstructures, a sacrificial layer can be deposited/grown and selectively removed later. However, single crystalline GaN can only be easily grown on single crystalline materials which are also hard to remove. Due to difficulties in removal of the sacrificial layer on which GaN can be grown on, the most practical option for releasing GaN structures for MEMS is the selective removal of the substrate under the GaN device area. In this case, Si is the best candidate as the substrate since mature micromachining techniques can be employed to either isotropically etch Si from the front-

side (*e.g.*, using xenon difluoride (XeF_2)) or through deep reactive ion etching (DRIE) or Bosch process from the back-side of the wafer. While DRIE is costlier and requires back-side lithography, not favorable in many fabrication processes; it allows for deposition of bottom metal electrode from the back side of the wafer. It is more versatile in the sense that it allows the entire epi-layer to be used for piezoelectric transduction, yielding higher electromechanical couplings. Furthermore, it does not involve large undercuts due to its directional nature. On the other hand, XeF_2 isotropic Si etch is faster, cheaper and compatible with front-side fabrication process. In this work, we use XeF_2 release technique when 2DEG is used as the bottom electrode, or where piezoelectric transduction is based on lateral electric field (no bottom electrode involved). We investigate both techniques and introduce a novel growth procedure based on lateral regrowth of GaN thin film on a meshed bottom metal layer.

2.5.2 Dry Etching of GaN

In order to define the contours of acoustic cavities wherein acoustic energy is trapped, plasma-based chemical dry etching is utilized as the patterning technique for group III-nitrides. In particular, high-density electron cyclotron resonance (ECR) and inductively coupled plasma (ICP) etch processes have yielded smooth, highly anisotropic, etch characteristics. The choice of the reactive source gas (Cl_2, BCl_3, ICl, IBr, *etc.*) and secondary gases (H_2, N_2, Ar) changes the concentration of reactive neutrals and ions in the plasma, which directly correlates with the etch rate. Smooth, anisotropic pattern transfer was obtained over a wide range of plasma etch platforms, chemistries, and conditions. The process parameters used for anisotropic etching of GaN by our group is summarized in

[2.4]. In the case where deposition of a bottom metal electrode is required, we use DRIE of Si substrate to form suspended structures and have access to the bottom of the GaN thin film.

2.5.3. Co-fabrication of GaN MEMS and HEMTs

The fabrication process of GaN MEMS/HEMT integrated platform is summarized in Fig. 2.6 [2.21]. The fabrication of the HEMTs starts with mesa isolation; 2DEG is maintained at the mesa islands and removed elsewhere by a short BCl_3/Cl_2 plasma etch. Next, source and drain Ohmic contacts are formed on the mesa islands. Proper surface cleaning is a critical step before Ohmic metal deposition. Ti/Al/Ti/Au (200/1000/450/550 Å) multilayer is evaporated and lifted off, followed by 30 s of thermal annealing in N_2 environment at 800~900 ˚C to let the low-work function metal penetrate into the barrier layer and access the 2DEG channel with low enough resistance. The low resistance between ohmic contacts ensures higher current densities. Next, Ni/Au (300/200~1000 Å) was used as Schottky contacts for gates and interconnect metallization. Devices are then passivated with Si_3Ni_4 or SiO_2 using plasma enhanced chemical vapor deposition (PECVD) to improve RF performance and avoid current slump by reducing surface trapping effects [2.22]. Following the completion of HEMTs, GaN is plasma etched to create contours of the resonators, followed by top electrode (Ti/Au) deposition and lift-off. Openings are then created on the passivation film to allow interconnection of HEMTs and resonators with Ti/Au pads. Finally, devices are released from the back side using deep reactive ion etching (DRIE), and Ti/Au is sputtered on the back to serve as the bottom electrode of the resonators [2.23].

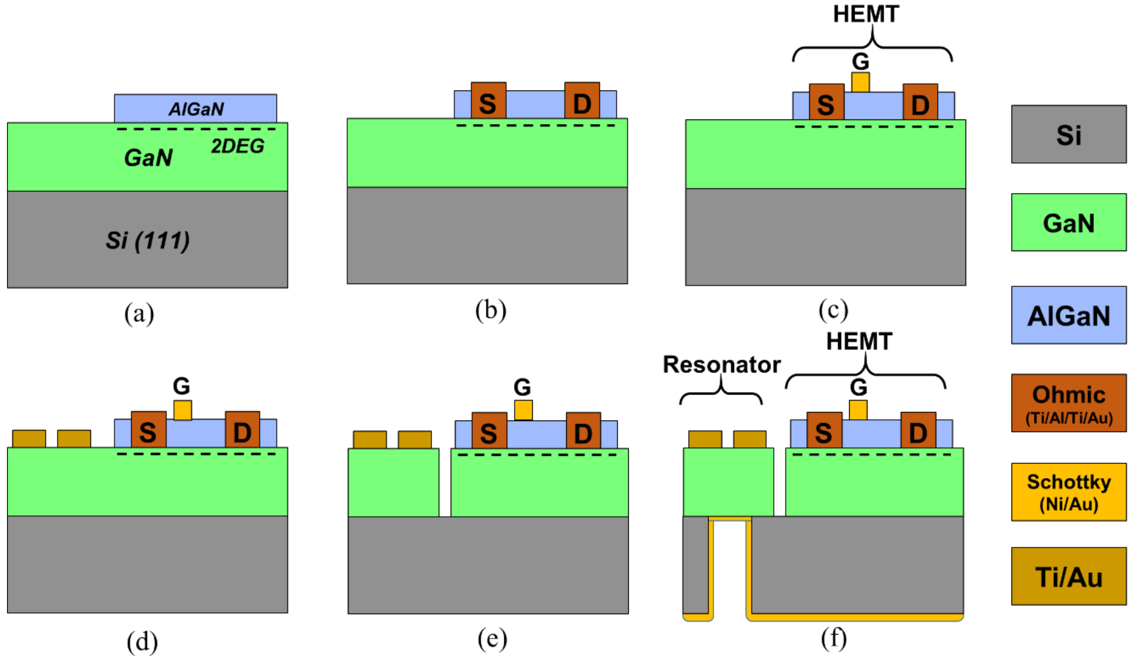

Figure 2.6 Fabrication process flow; a) mesa isolation using a short chlorine etch, b) Ohmic contact metallization and rapid thermal annealing, c) formation of gate Schottky contac, d) deposition of top metal electrode of the resonator, e) GaN chlorine-based plasma etch for defining resonator contours, f) DRIE backside etch and sputtering of gold as the bottom metal electrode.

As a cost-effective alternative to DRIE, we utilize XeF_2 isotropic etch of Si to form suspended membranes in the case that 2DEG is used as the bottom electrode, or the actuation is based on the lateral electric field excitation (no need for bottom electrode). The fabrication process is summarized in Fig. 2.7. It again starts with the HEMT fabrication steps and only has an additional step to etch Si isotropically from the front side. Using such process, various electromechanical devices such as resonant body transistors, depletion-mediated transistors, resonators with 2DEG as the top electrode, can be realized and co-fabricated with the GaN circuitry (Fig. 2.8).

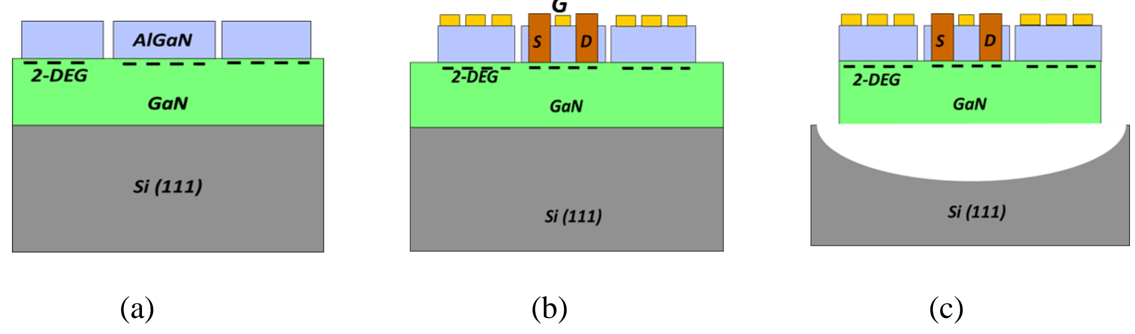

Figure 2.7 Fabrication steps: (a) mesa isolation, AlGaN is etched to define the active area of resonator/HEMTs, (b) ohmic contact metallization and annealing, used for contacting 2DEG and forming the source and drain of the HEMTs, (c) Schottky contact formation used as IDT sets for acoustic excitation/sensing and HEMT gates. (d) Trenches are made through GaN and Si is subsequently etched isotropically using XeF2.

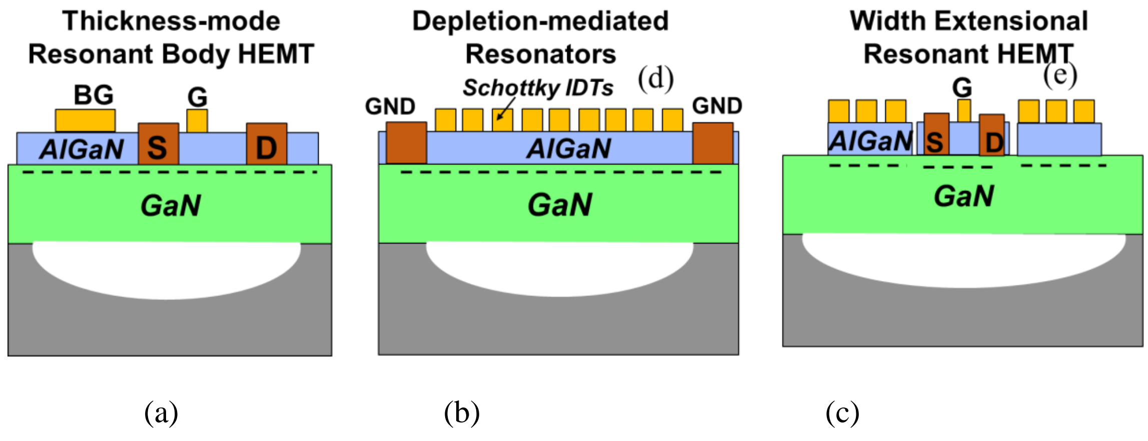

Figure 2.8 Various MEMS devices relized with the fabrication process demonstrated above. (a) thickness-mode RB-HEMT (Chapter 4), (b) depletion-mediated piezoelectric AlGaN/GaN resonators, and (c) width-extensional resonant HEMTs (Chapter 5).

2.6 GaN Resonators with Embedded Meshed Metal Bottom Electrode

We present a new GaN resonator architecture that employs a metal layer within the piezoelectric stack [2.24] and discuss its advantages from both fabrication and acoustic performance points of view. We used a commercial 500 nm-thick unintentionally-doped (UID) GaN template grown on a Si (111) substrate purchased from Kyma Technologies

[2.25]. Next, the GaN buffer layer was patterned and etched with 250 nm-deep trenches using a chlorine (Cl_2) based plasma recipe (Fig. 2.9 (a)) and refilled with sputter-deposited W and evaporated SiO_2 layers of ~120 nm and ~100 nm-thick, respectively (Fig. 2.9 (b)). The W/SiO_2 patterning was done using a lift-off process. The W/SiO_2 formed a pattern such that GaN can be partially exposed to serve as the seed layer for the subsequent GaN regrowth. The sample surface was cleaned of organic contaminants with oxygen (O_2) plasma, acetone, and Isopropyl alcohol (IPA). Hydrogen peroxide (H_2O_2) wet surface cleaning was then performed to clean any trace of exposed W. Exposed W can diffuse into regrown GaN layer if it is not capped well with SiO_2. The sample was returned to the MOCVD reactor to regrow the thick GaN layer. The regrowth was done by our collaborators at National Chiao Tung University (Taiwan), using a Veeco D75 MOCVD system. The growth temperature was 1070 °C, with a V/III ratio of 1500. Nitrogen (N_2) and hydrogen (H_2) were used as the environment gases with H_2 as the carrier gas. The growth rate was ~2.8 μm/h. The thickness of the regrown GaN is measured to be ~2.5 μm (Fig. 2.10). SEM images of the refilled trenches and the cross-section of the regrown GaN are shown in Fig. 1. To prove the good quality of the regrown GaN on the meshed structure, photoluminescence (PL) measurements on the regrown GaN on the meshed structures are compared against measurement points on a reference sample (Fig. 2.11).

Besides facilitating the fabrication of the GaN BAW resonators through elimination of backside DRIE and metal sputtering, in the new process, we have precise control over the placement of the embedded metal electrode and can therefore excite the thickness resonance modes efficiently. Embedding the SiO_2 structures within the resonant stack can

compensate for the negative TCE of the GaN layer. SiO_2, unlike most other materials has a positive TCE and is used to cancel out the effect of temperature on the elasticity and thus resonance frequency. Depositing SiO_2 on the surface of the resonator is not efficient since the surface is stress-free and larger volumes of SiO_2 will be required to fully compensate temperature-induced frequency.

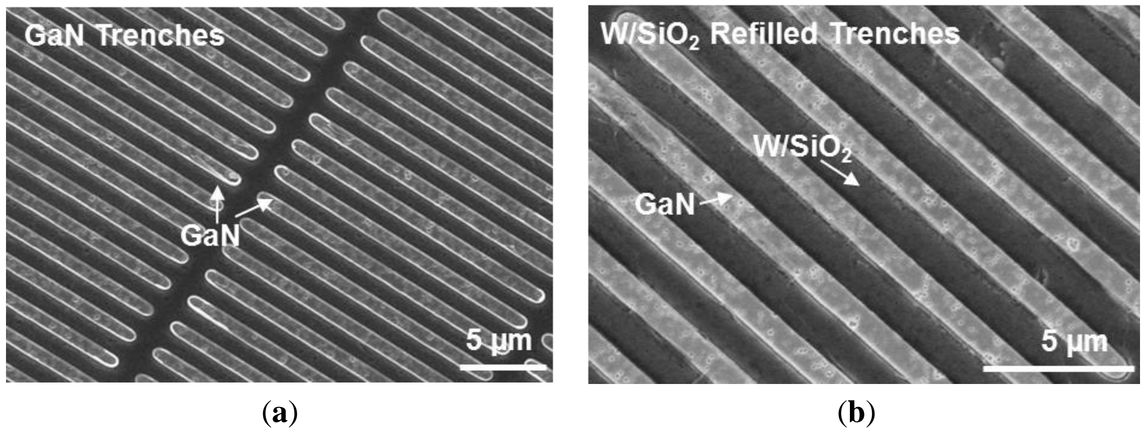

Figure 2.9 SEM images showing (a) 250-nm deep trenches made in GaN, forming a grid-like pattern; (b) trenches are refilled with W/SiO_2. GaN islands act as the seed layer for the GaN regrowth initiation.

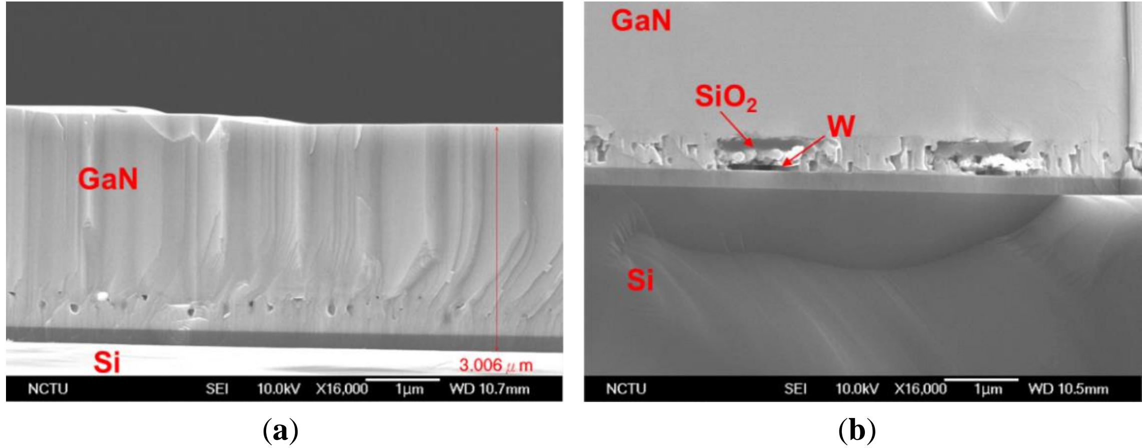

Figure 2.10 SEM images of the cross-section of the regrown GaN, (a) on a reference GaN buffer layer of 500 nm thickness with no pattterns. The total thickness of the GaN stack is ~3 µm. (b) GaN regrown on W/SiO_2 structures and GaN islands. The regrowth of GaN has well-coalesced and a uniform film is grown on top of the meshed metal electrode.

The regrown GaN on the patterned seed layer is characterized and compared against GaN regrown on non-patterned GaN seed layer (reference). PL measurements are taken to prove that the quality of GaN formed on the patterned structure is not degraded. Results shown in Fig. 2.11 demonstrate that high-quality GaN layers can be grown on a patterned metal electrode.

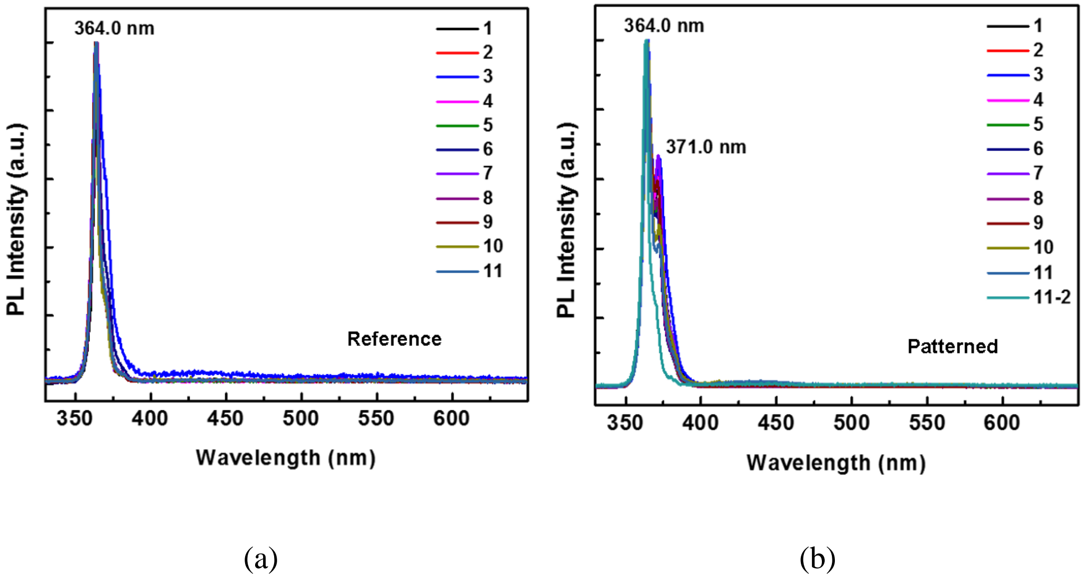

(a) (b)

Figure 2.11 Room temperature photoluminescence (PL) measurement of 11 different points on (**a**) the reference sample, where GaN is grown on a thin GaN buffer layer without any patterns and embedded metals, or the reference, and (**b**) on the W/SiO_2 patterned structures. The PL measurements clearly indicate the GaN peak (at 364 nm) is not degraded in (**b**).

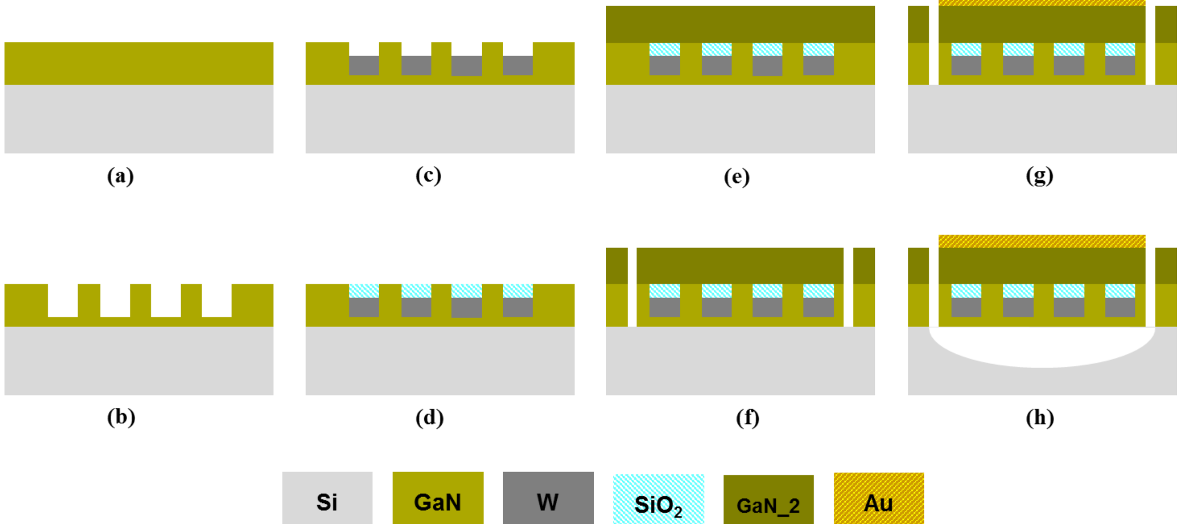

Figure 2.12 Fabrication steps of GaN resonator with embedded bottom electrode. (a) A thin layer of GaN is grown on a Si (111) substrate, (b) 250 nm deep trenches are made in the GaN layer using BCl_3/Cl_2 plasma etch, (c)thetrenches are filled with sputtered W and (d) evaporated SiO_2, (e) GaN device layer is regrown on the W/SiO_2 mesh, starting from the bottom GaN seed layer, (f) trenches are made through the GaN layer to access the Si substrate, (g) the top metal is deposited on the device area, (h) the resonator is released with XeF_2 isotropic etch.

Growing GaN on patterned layers requires careful control over the thickness of the etched and refilled trenches, as well as the regrown GaN layer to ensure surface uniformity and smoothness. This is not a trivial problem to tackle, as our GaN thin films suffered from surface non-uniformity, replicating the meshed patterns on the regrown GaN surface. Although PL measurements (shown in Fig. 2.11) demonstrate that the quality of the regrown GaN is not degraded, the surface roughness is still an issue that should be addressed in order to build high-performance MEMS devices. Future effort should be directed to minimize the surface roughness to ensure lower loss and thus higher quality factors.

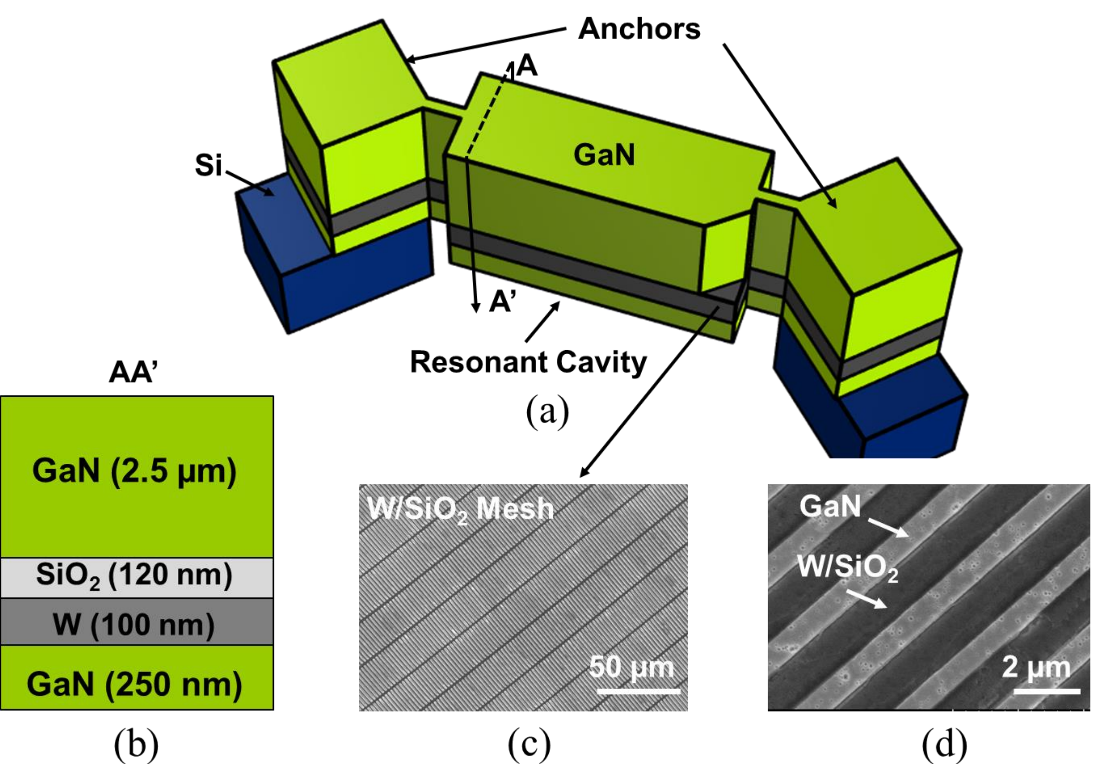

Figure 2.13 (a) An exemplary schematic of a GaN resonator with a thick GaN layer grown on W/SiO_2 embedded electrodes. (b) The resonant stack schematic with a total thickness of ~3 µm. (c,d) SEM images of the GaN trenches before the GaN regrowth.

2.7 Conclusion

Advances in material growth and characterization can greatly enhance the performance of GaN MEMS. Similar to the path taken by AlN MEMS over the course of the past few decades, one can envision cost-effective GaN thin films grown on versatile substrates in high volumes. Previously, the only deposition technique of AlN was single-crystalline epitaxial growth, whereas nowadays, fast, cost-effective sputtering of AlN has made AlN MEMS very popular. Currently GaN MEMS suffers from unknown material properties that require iterative designs and wafer-to-wafer material characterization.

In this chapter various fabrication techniques were discussed which allow for co-fabrication of GaN-on-Si MEMS and HEMTs. Having GaN thin films grown on versatile substrates with customized thickness (ultra-thin films), as well as flexibility over the location of the 2DEG/2DHG can greatly benefit the AlGaN/GaN transducers discussed in the following chapters.

Chapter 2: References

[2.1] D. Hanser and K. R. Evans, "Development of the Bulk GaN Substrate Market," in *Technology of Gallium Nitride Crystal Growth*, Vol. 133, Springer Berlin Heidelberg, 2010, pp. 3-27.

[2.2] V. Cimalla, J. Pezoldt, and O. Ambacher, "Group III nitride and SiC based MEMS and NEMS: materials properties, technology and applications," *Journal of Physics D: Applied Physics*, Vol. 40, No. 20, pp. 6386-6434, 2007.

[2.3] S. Nakamura and M. R. Krames, "History of Gallium Nitride-Based Light-Emitting Diodes for Illumination," *Proceedings of the IEEE*, Vol. 101, No. 10, pp. 2211-2220, 2013.

[2.4] M. Rais-Zadeh, V. Gokhale, A. Ansari, M. Faucher, D. Theron, Y. Cordier, L. Buchaillot, "Gallium nitride as an electromechanical material," *IEEE Journal of Microelectromechanical Systems*, Vol. 23, No. 6, pp. 1252–1271, December, 2014.

[2.5] C. Shi, P. Asbeck, E. Yu, "piezoelectric polarization associated with dislocations in wurtzite GaN," *Applied Physics Letters*, Vol. 74, No. 4, Jan. 1999.

[2.6] A. Polian, M. Grimsditch, and I. Grzegory, "Elastic constants of gallium nitride," *Journal of Applied Physics*, Vol. 79, no. 6, pp. 3343-3344, 1996.

[2.7] F. Bernardini, V. Fiorentini, and D. Vanderbilt, "Spontaneous polarization and piezoelectric constants of III-V nitrides," *Physical Review B*, Vol. 56, No. 16, pp. 10024-10027, 1997.

[2.8] M. S. Shur, A. D. Bykhovski, and R. Gaska, "Pyroelectric and Piezoelectric Properties of GaN-Based Materials," *MRS Online Proceedings Library*, Vol. 537, 1998.

[2.9] "Electrical/Physical Properties of GaN," Available Online: http://www.ee.sc.edu/personal/faculty/simin/ELCT871/02%20GaN%20Properties.pdf, Accessed on July 19, 2016.

[2.10] C. Luo, D. R. Clarke, and J. R. Dryden, "The temperature dependence of the thermal conductivity of single crystal GaN films," *Journal of Electronic Materials*, Vol. 30, No. 3, pp. 138-146, 2001.

[2.11] A. Jeżowski, B. A. Danilchenko, M. Boćkowski, I. Grzegory, S. Krukowski, T. Suski,,"Thermal conductivity of GaN crystals in 4.2–300 K range*," Solid State Communications*, Vol. 128, No. 2–3, pp. 69-73, 2003.

[2.12] W. Liu and A. A. Balandin, "Thermal conduction in $Al_xGa_{1-x}N$ alloys and thin films," *Journal of Applied Physics*, Vol. 97, No. 7, pp. 073710 - 073710-6, 2005.

[2.13] V. Siklitsky. (1998, 11/30/2013). Semiconductors on NSM-Gallium Nitride (1998 ed.). Available: http://www.ioffe.ru/SVA/NSM/

[2.14] V. Bougrov, "Gallium Nitride (GaN)," in Properties of Advanced Semiconductor Materials: GaN, AIN, InN, BN, SiC, SiGe, ed New York, NY: John Wiley & Sons, 2001.

[2.15] M. Edwards, "Temperature dependent properties of GaN," University of Bath (UoB), MorGaN Report, Feb. 2009.

[2.16] V. J. Gokhale and M. Rais-Zadeh, "Phonon-Electron Interactions in Piezoelectric Semiconductor Bulk Acoustic Wave Resonators," *Scientific Reports*, Vol. 4, No. 5617, pp. 5617:1-5617:10, 2014.

[2.17] NG Weimann *et al.,* "Scattering of electrons at threading dislocations in GaN," *J. of Applied Physics* 83, 3656, 1998.

[2.18] M. A. Moram *et al.*, "On the origin of threading dislocations in GaN films," *J. of Applied Physics*, 106, 073513, 2009.

[2.19] GaN Essentials, Application Note-011 Substrates for GaN RF Devices, Nitronex Corporation.

[2.20] A. Ansari, V. J. Gokhale, V. A. Thakar, J. Roberts, and M. Rais-Zadeh, “Gallium nitride-on-silicon micromechanical overtone resonators and filters,” *IEEE Electron Device Meeting (IEDM)*, pp. 20.3.1-20.3.4, Washington, DC, Dec. 2011.

[2.21] A. Ansari, V. Gokhale, J. Roberts, and M. Rais-Zadeh, “Monolithic integration of GaN-based micromechanical resonators and HEMTs for timing application,” *IEEE International Electron Device Meeting (IEDM’12)*, San Francisco, CA, pp. 15.5.1-15.5.4, Dec. 2012.

[2.22] B. M. Green, *et al.*, “The effect of surface passivation on the microwave characteristics of undoped AlGaN/GaN HEMTs,” IEEE Electron Device Letters, Vol. 21, No. 6, pp. 268-270, June 2000.

[2.23] L. F. Eastman, *et al.*, “Undoped AlGaN/GaN HEMTs for microwave power applications,” IEEE *Transaction on Electron Devices*, Vol. 48, No. 3, pp. 479-485, March 2001.

[2.24] A. Ansari, C.-Y. Liu, C.-C. Lin, H.-C. Kuo, P.-C. Ku, and M. Rais-Zadeh, “GaN micromechanical resonators with meshed metal bottom electrode,” *Materials*, 8(3), pp. 1204–1212, 2015.

[2.25] Kyma Techologies. Available online: http://www.kymatech.com/ (Accessed on 10 May 2016).

Chapter 3 Gallium Nitride MEMS Devices

In this chapter we investigate the principle of piezoelectric transduction in GaN thin-film MEMS devices. Particularly, we focus on composite GaN-on-Si and GaN MEMS resonators and filters used to build thin-film piezoelectric bulk acoustic wave (BAW) MEMS (*e.g.* BAW resonators, acoustic filters, thickness-mode film bulk acoustic resonators (FBARs) and *etc.*). Such devices are realized using GaN-on-SOI and GaN-on-Si 4-inch wafers, where the Si substrate is removed from the backside using the DRIE process and a metal bottom electrode is sputtered from the back side. We characterize different performance metrics of such devices including their $frequency \times Q$ values, power handling capability, linearity, temperature trends, electromechanical coupling coefficient, and motional impedance, and show the viability of their application as frequency selective components in oscillators in RF modules.

3.1 GaN-on-Si thickness-mode MEMS resonators and filters

Thin-film piezoelectric on substrate (TPoS) [3.1] micromechanical devices have been traditionally implemented on conventional piezoelectric materials such as AlN [3.2], ZnO [3.3], and PZT [3.4]. In most of these implementations, the Si layer dominates the stack structure and thus the resonance frequency and the mode shape. Si with a higher energy density than the materials in question improves the Q as well as mechanical robustness, when compared to the case of single material piezoelectric resonators. Furthermore, since Si is a low-acoustic loss material, the thick Si layer suppresses the acoustic non-linearity of the piezoelectric material, leading to a more linear and distortion-free performance at higher power levels. GaN is a prime candidate for TPoS structures since the acoustic velocity of GaN is very close to Si, resulting in lower acoustic mismatch. The Si layer in the GaN-on-Si TPoS stack not only improves the acoustic properties of the resonator but can also be used as the bottom electrode, eliminating the need for bottom metallization. It is specifically difficult to embed a bottom metal layer in a GaN epi-stack, as it is very difficult to epitaxially grow GaN on any metal layer. Previous GaN resonator implementations with top and bottom electrodes have used backside sputtered metals [3.5], or two-dimensional electron gas (2DEG) as the bottom electrode [3.6]. Here, we report on GaN TPoS resonators and filters which benefit from the Si in the stack (as the bottom electrode as well as the structural material) to achieve improvement in $frequency \times Q$ values and better power handling performance when compared to single crystalline GaN resonators.

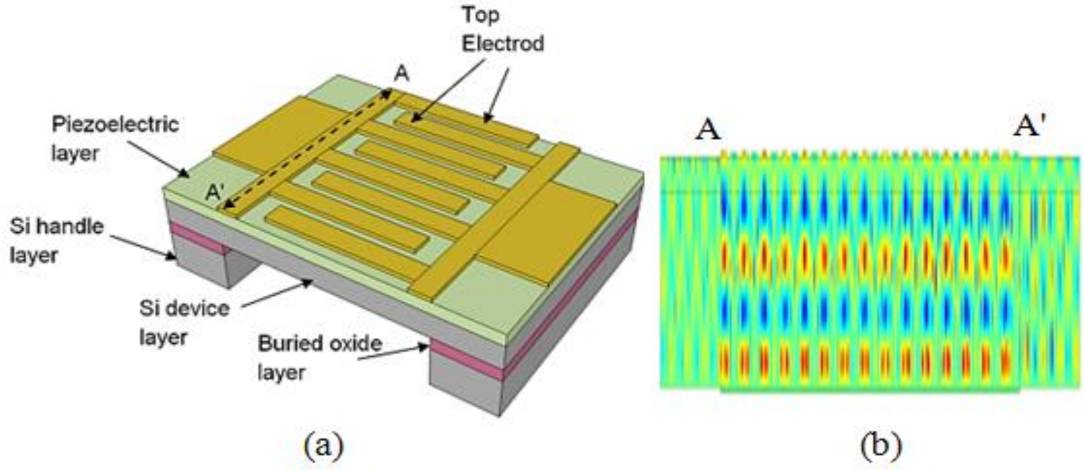

Figure 3.1 (a) A schematic view showing the TPoS filter configuration. (b) COMSOL 2D simulation of the displacement of the fifth-order thickness resonance mode.

The operating frequency of a thickness-mode TPoS filter, as shown in Fig. 3.1, is determined by the thickness and material composition of the stack. The device shown in Fig. 3.2(a) has its fifth-order thickness resonance mode at 2.1 GHz. The bandwidth and the loss of the filter are determined by the number of top electrode fingers, electrode geometry, spacing, and active electrode area [3.7]. The bandwidth of this filter with electrode width of 10 μm and electrode spacing of 3 μm is 20.2 MHz (Fig. 3.2 (b)). COMSOL multi-physics software was used to simulate the frequency response of the device (Fig. 3.3 (a)). The measured response (Fig. 3.3 (b)) agrees reasonably with the simulated response. Knowledge of precise material properties and thickness is necessary for an accurate simulation; uncharacterized AlN/AlGaN layer and fabrication errors can explain the discrepancy between the simulated and measured results.

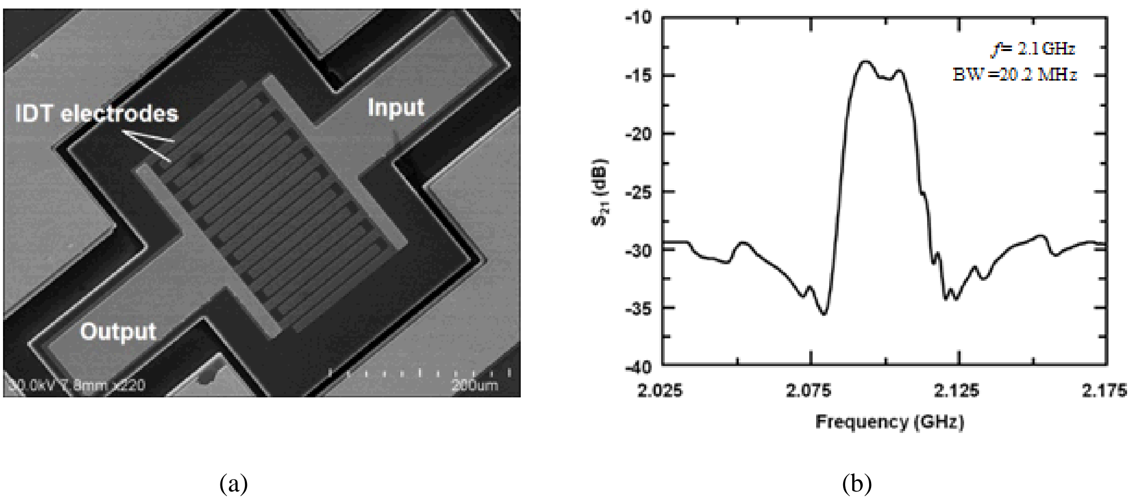

(a) (b)

Figure 3.2 (a) An SEM image of a GaN-on-Si filter with electrode width of 10 μm, electrode spacing of 3 μm and active area of 260× 240 μm^2. (b) Measured filter frequency response exhibiting a center frequency of 2.1 GHz and a bandwidth of 20.2 MHz.

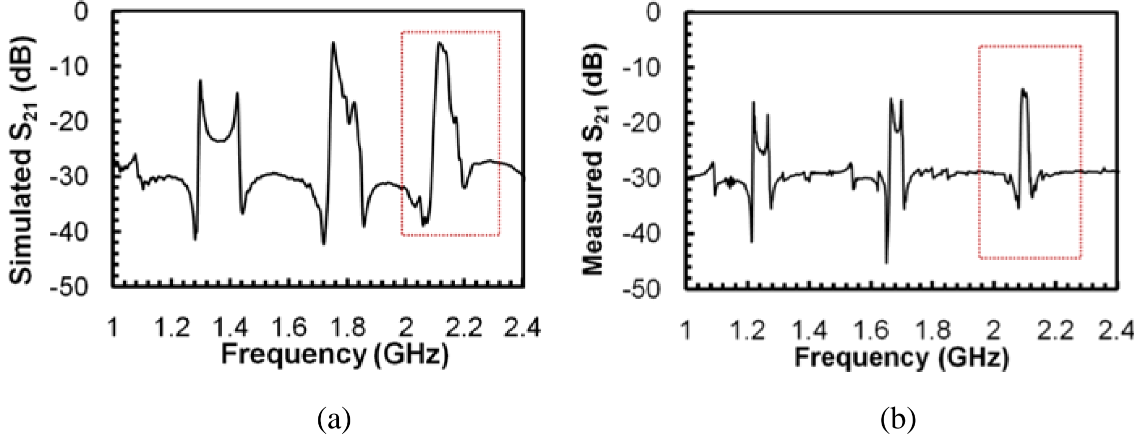

(a) (b)

Figure 3.3 Wide-band filter frequency response showing a good match between the (a) simulated and (b) measured frequency responses.

The second-order thickness mode of a TPoS filter demonstrates a high Q of 1850 at 802.5 MHz at ambient pressure and room temperature (Fig. 3.4), which results in a high *frequency* $\times Q$ value of 1.5×10^{12}.

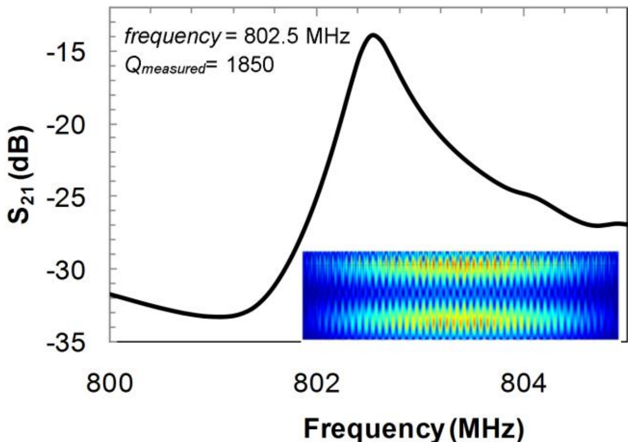

Figure 3.4 Measured S_{21} response of a TPoS filter at 802.5 MHz. Inset shows the mode shape obtained using ANSYS.

In addition to TPoS filters, FBARs have been fabricated on the same substrate. An apodized FBAR shown in Fig. 3.5 exhibits a loaded Q of 210 at its fifth-order thickness-mode resonance frequency of 2.1 GHz (Fig. 3.6). The unloaded Q of the resonator is extracted to be 424, demonstrating a $frequency \times Q$ value of 0.89×10^{12}. The extracted k_t^2 of the FBAR is 1.7% which agrees favorably with the theoretical value of 1.9 % reported in the literature [3.8].

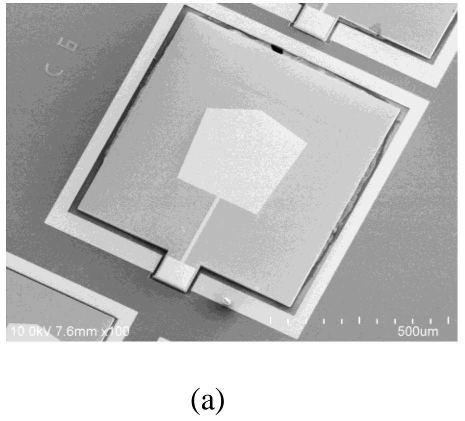

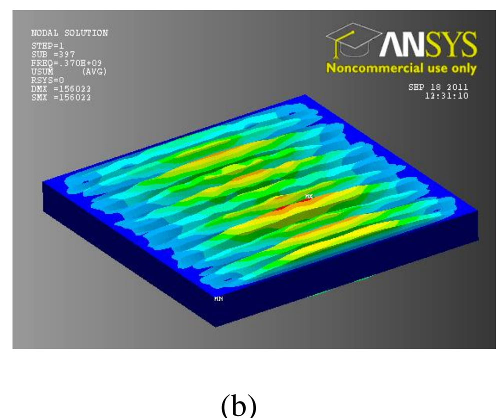

(a) (b)

Figure 3.5 (a) A SEM image of an apodized GaN-on-Si FBAR with an active area of 81600 μm^2. (b) ANSYS simulation of the FBAR showing the first-order thickness mode frequency at 370 MHz.

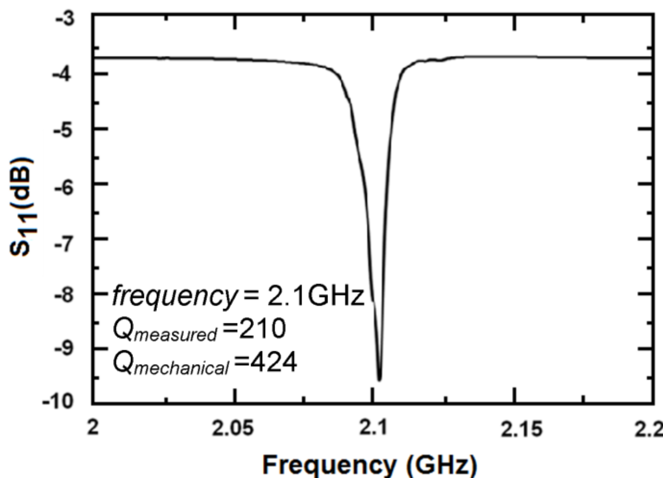

Figure 3.6 Measured response of the GaN-on-Si FBAR. Extracted mechanical Q is 424 at 2.1 GHz.

The Mason's model (3.7 (a)) can be used to predict the thickness-mode frequency and the impedance of piezoelectric resonators. The Mason's model [3.9] translates each layer in the resonator stack to a T-network, based on the material's thickness and acoustic velocity, defined as $Z_{acoustic} = \rho \times v$, where ρ is the mass density and v is the acoustic velocity in the material. C_C is the clamped capacitance given by $C_C = A/(\beta^S t)$, where A is the area of the electroded region, t is the thickness of the piezoelectric layer, and β^S is the dielectric impermeability of the piezoelectric material at a constant strain. Each series and shunt impedance in the T-network is given by:

$$Z_1 = -j \times Z_{acs} \times \tan(\frac{kt}{2}), \qquad \text{(Equation 3.1)}$$

$$Z_2 = j \times Z_{acs}/\sin(kt), \qquad \text{(Equation 3.2)}$$

respectively; where k is the wave number. Using this model, the predicted impedance plot is overlapped with the measured impedance plot. There is a good match between the measured and simulated results. The anchor design, residual stress in the films, and electrode layout are not taken into account in the Mason's model, which explains the

discrepancy between the measured and simulated impedance plots shown in Fig. 3.7 (b). Using this model, the fundamental thickness mode frequency estimated at 365 MHz, and the four overtones of the FBAR and their impedance values are depicted in Fig. 3.8 and compared against measurement results showing a very good match.

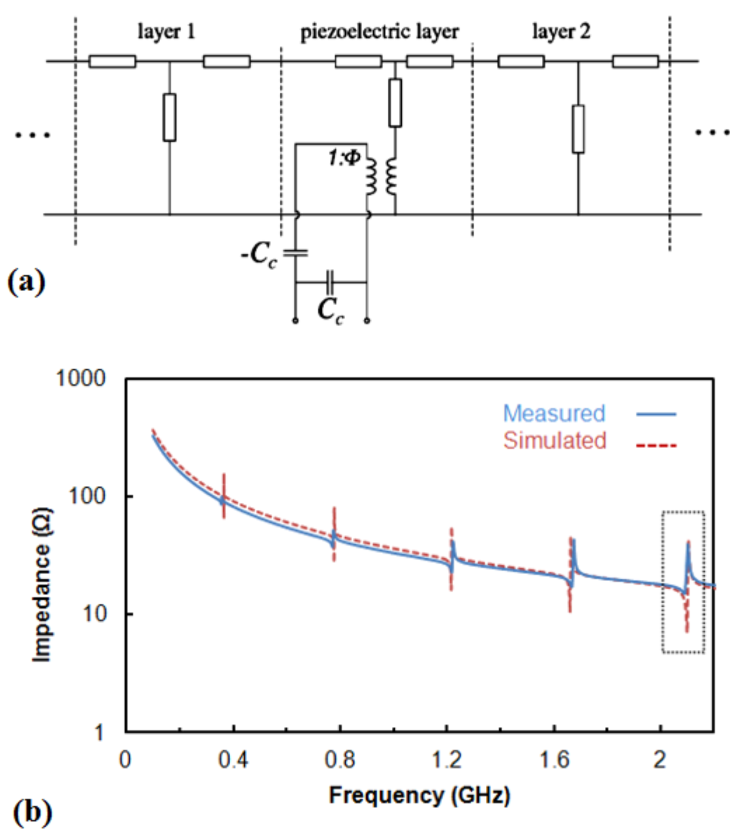

Figure 3.7 (a) Mason's model of a thickness-mode resonator. (b) Simulated and measured impedance plots of the FBAR in a wide frequency range, showing a good match between the measured and simulated responses. The impedance is shown in logarithmic scale.

3.1.1 Power Handling

Nonlinearities of the piezoelectric resonators introduce distortion and noise and therefore limit the output power level. The added Si layer in the stack improves the power

handling capability as the thick Si has a higher energy density [3.3]. The frequency response of the TPoS filter at different power levels clearly shows that the distortion introduced at higher power levels is negligible (Fig. 3.8).

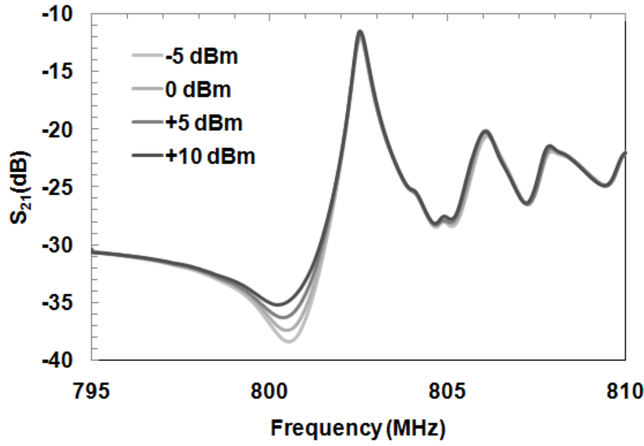

Figure 3.8 Measured S_{21} response of the TPoS filter at different power levels.

3.1.2 Temperature Trends

Fig. 3.9 shows the variation of resonance frequency over a temperature range of 150 K to 300 K. The frequency drops linearly in this range. The temperature coefficient of frequency (TCF) of the GaN-on-Si resonator is extracted to be -20.4 ppm/K.

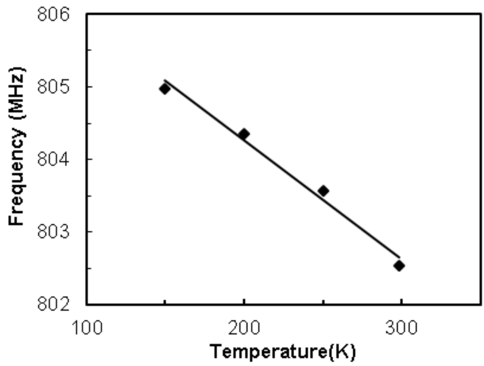

Figure 3.9 Linear resonance frequency variation of the TPoS filter over a temperature range of 150 K to 300 K.

3.1.3 Comparison with other TPoS resonators

The work presented in this chapter demonstrates first time implementation of resonant micromechanical devices realized in GaN-on-Si platform. The use of this configuration enables leveraging the excellent acoustic properties of Si with piezoelectric properties of GaN. This combination has significant advantages over contemporary technologies in terms of performance and integration with Si electronics.

Table III compares the performance of GaN-on-Si resonator reported in this chapter with other conventional piezoelectric-on-Si resonators reported to date [3.2-3.4].

Table III
Comparison of this work with more conventional TPoS resonators and filters.

Reference	TPoS	Resonance Mode	*Freq* (MHz)	*f x Q*	Power Handling	*TCF* (ppm/K)
R. Abdolvand et al.	AlN-on-Si	9th order lateral	**208**	**1.2 x 10^{12}**	Bifurcation at 15 dBm	-2 (compensated)
	AlN-on-Si	Length Extensional	**1006**	**4.2 x 10^{12}**	-	-
G. K. Ho et al.	ZnO-on-Si	6th order lateral bulk	**90**	**0.3 x 10^{12}**	No distortion up to 5 dBm	N/A
H. Chandrahalim et al.	PZT-on-Si	1st order length extensional	**15.94**	**7.97 x 10^{10}**	-	-16 ~ -20
This Work*	GaN-on-Si	2nd order thickness	**802.5**	**1.5 x 10^{12}**	No distortion up to 10 dBm	-20

3.2 GaN Thickness-mode MEMS Resonators

In this section, we present fundamental and high-order harmonics of a thickness-mode GaN-only bulk acoustic wave (BAW) resonator showing fundamental thickness-mode

resonance at 2.18 GHz, with a quality factor (Q) of 655 and a coupling coefficient (k_t^2) of 1%. The fourth-order thickness-mode resonance at 8.7 GHz with an extracted Q of 330, exhibits the highest resonance frequency measured to date on GaN micromechanical resonators with a high *frequency* $\times$ Q value of 2.87×10^{12}. The choice of thickness-mode resonance is motivated by scaling the resonance frequency to multi-GHz regime. Thickness-mode resonators are advantageous for high-frequency applications because they overcome the limits set by lithography, since the resonance frequency is determined by the piezoelectric film thickness and can be further scaled by targeting harmonics of the resonance mode.

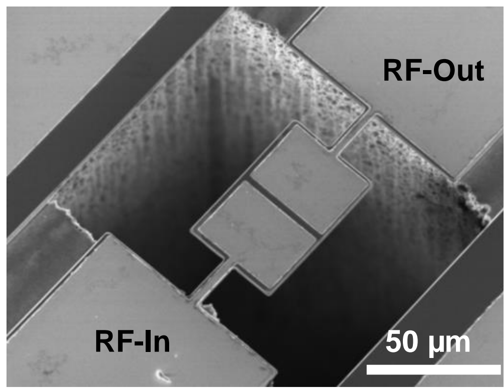

Figure 3.10 SEM image of a fabricated 40 µm × 60 µm GaN BAW resonator, with tethers of 20 µm in length and 5 µm in width.

The two-port wide-band transmission response of the thickness-mode resonator (Fig. 3.10) is shown in the frequency range of 1-10 GHz, in Fig. 3.11, along with the corresponding mode shape for each harmonic of the thickness-mode resonance [3.10]. The fundamental thickness-mode resonance at 2.22 GHz shows an acoustic velocity of ~7920 m/s.

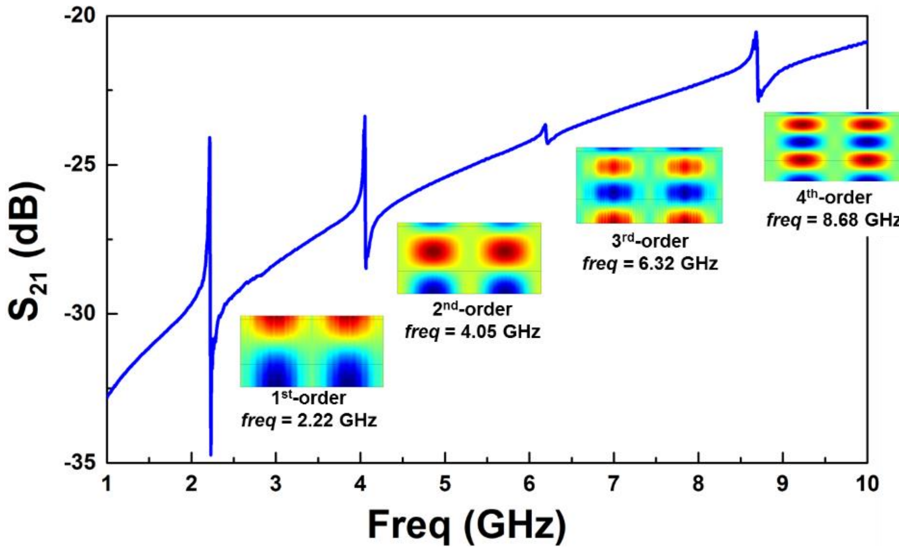

Figure 3.11 Wide-band frequency response of the 40 μm × 60 μm GaN resonator. The effect of capacitive feed-through is not de-embedded from the response. The mode shape for each thickness-mode resonance is also shown.

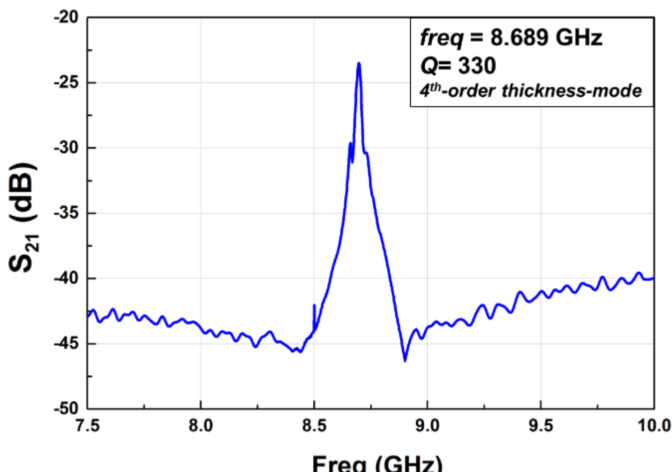

Figure 3.12 De-embedded frequency response of the 40 μm × 60 μm GaN resonator with a resonant frequency of 8.7 GHz, and an extracted Q of 330 at room temperature and ambient pressure. Capacitive feed-through is de-embedded from the resonator response using an unreleased but otherwise identical resonator.

The mechanical response of the fourth-order thickness-mode resonance is de-embedded and sketched in Fig. 3.12. Operation at the fourth-order thickness-mode resonance as compared to lower harmonics, primarily benefits from reduction of three loss

mechanisms, (1) visco-elastic damping, (2) thermo-elastic damping (TED), and most importantly (3) phonon-phonon scattering, as the intrinsic material loss is limited by the Landau–Rumer regime at such high frequencies (see chapter 1 section 1.3), hence larger $frequency \times Q$ values are expected.

The power handling and nonlinearity of the resonator are characterized in Fig. 3.13, showing similar results for the first and fourth-order thickness-mode resonances. Third-order input intercept point (IIP_3) values are extracted in Figs. 3.13 (a, b), showing the highest reported IIP_3 values of ~30 dBm for GaN-based bulk resonators. The 1-dB power compression point (P1-dB) occurs at an input power level of Pin= 16 dBm for both the first and fourth-order harmonics (Fig. 3.13 (c)), suggesting that the power handling and device linearity are most likely limited by the anchor design and are independent of the operation mode [3.11].

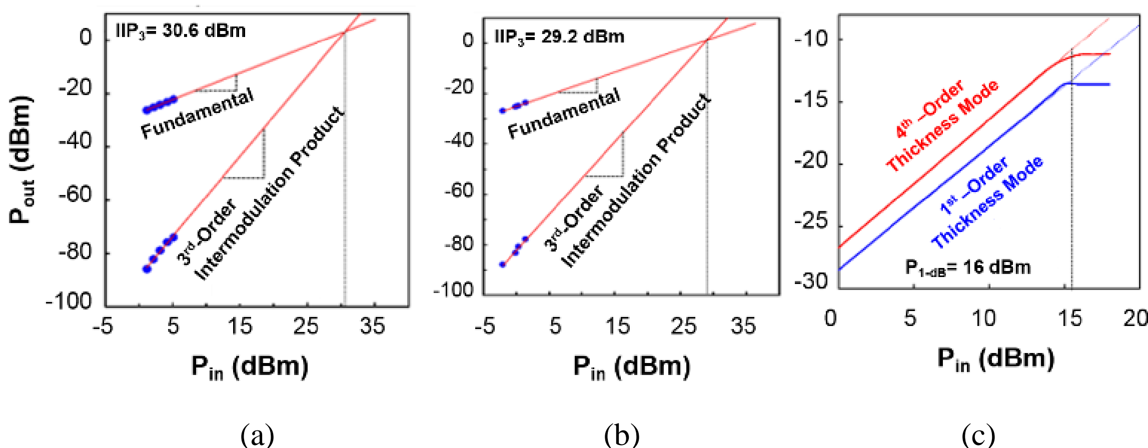

(a) (b) (c)

Figure 3.13 Two-tone power measurements of the (a) first and (b) fourth-order thickness-mode harmonics. The IIP3 value is extracted to be 30.6 dBm and 29.2 dBm, respectively, with a frequency separation of 5.1 KHz. (c) P1-dB measurement showing P1-dB of ~16 dBm for both the first and the forth-order thickness-mode resonances. It must be mentioned that different coupling coefficients affect IIP_3 values of the two modes.

3.3 GaN Contour-mode MEMS Resonators

In this section, GaN contour-mode MEMS resonators are characterized where the resonance frequency is determined lithographically. Fig. 3.14 shows the frequency response of a two-port contour-mode GaN resonator. The Q is 7413 at room temperature and ambient pressure. In Fig. 3.15, the measured *frequency* and Q are shown at a temperature range of 100 K to 300 K. The TCF is estimated to be -17.2 ppm/K at 295 K.

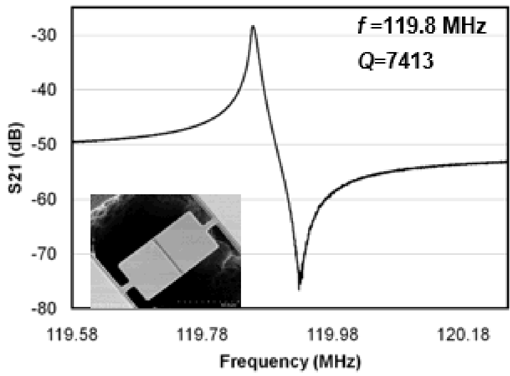

Figure 3.14 Room temperature frequency response of an 80 µm × 40 µm GaN resonator with center frequency (f) of 119.8 MHz and high Q of 7413. This resonator demonstrates a very high frequency ×Q value of 0.88×10^{12}.

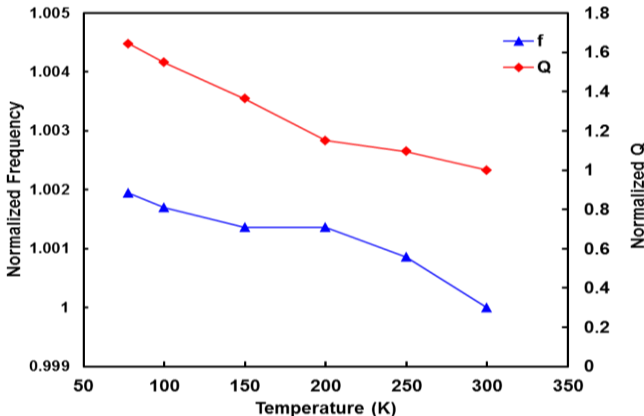

Figure 3.15 Normalized resonance frequency and measured Q of the GaN resonator *vs*. temperature. The TCF value of the resonator is extracted to be -17.2 ppm/K.

3.4 GaN Radial (Breathing)-mode Coupled Ring Resonators

Another class of bulk-mode resonators are radial-extension or breathing mode MEMS resonators, most popular in optomechanical resonators. Such designs offer low motional impedance. Here, we present a "dogbone" GaN bulk-mode resonator. It is comprised of two rings that are connected through a center coupling rod, which mimics a "dogbone" shape. The ring can vibrate in radial extensional mode. In this mode, the resonance frequency can be designed with lithographically defined geometries and is insensitive to the device thickness variation. The coupling rod is attached to the edge of the ring, which is a high velocity point for radial extensional mode [3.12]. This creates a strong energy coupling between the two vibrating rings. The resonator is anchored at the center of the coupling rod, which is the pseudo-nodal point of the in-phase radial extension mode. Such an anchor structure avoids direct attachment to the vibrating rings, and, therefore, the in-plane radial extension mode has low anchor loss. The mechanical coupling scheme improves the power handling and reduces motional impedance compared to a single resonator. The wide-band frequency response is shown in Fig. 3.16. A record $f \times Q$ value of 1.05×10^{13} is achieved at 1.62 GHz.

3.5 Conclusion

In this chapter we demonstrated high-performance piezoelectric bulk-mode GaN-on-Si TPoS and GaN MEMS devices. We showed thickness and contour-mode BAW acoustic resonators and filters, with high $f \times Q$, resonance frequency and high power handling

capabilities. In the next chapter, we show a platform for integration of such devices with AlGaN/GaN HEMTs.

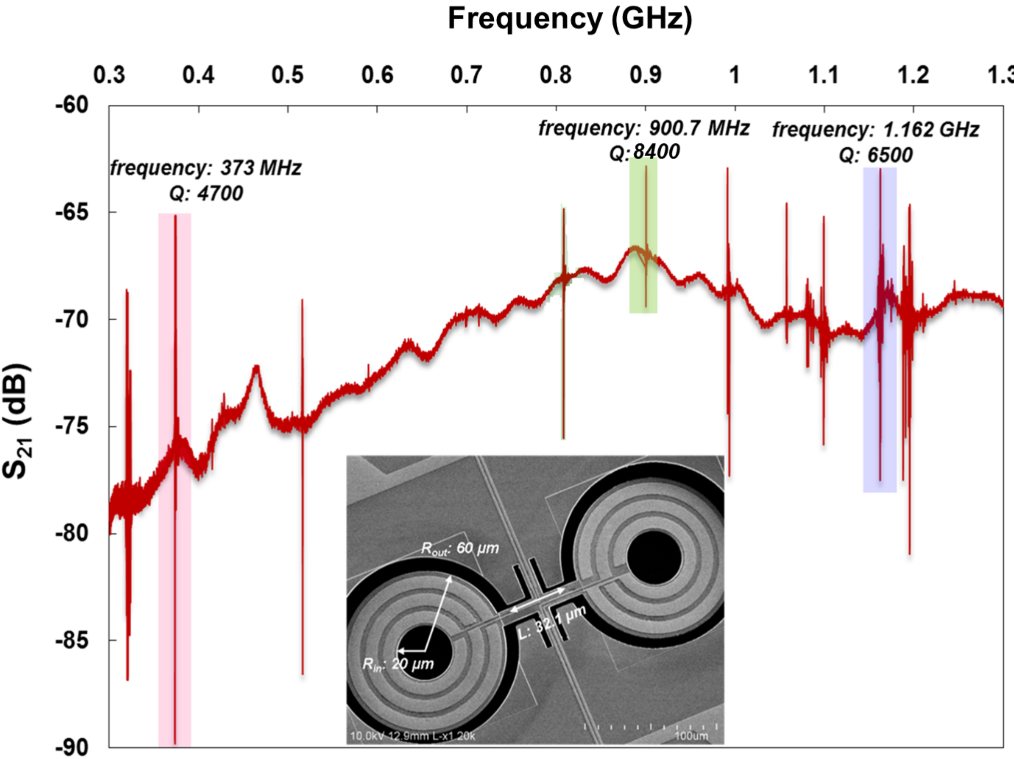

Figure 3.16 Wide band frequency response of dog-bone resonators. The inner and outer radii are 20 and 60 μm respectively.

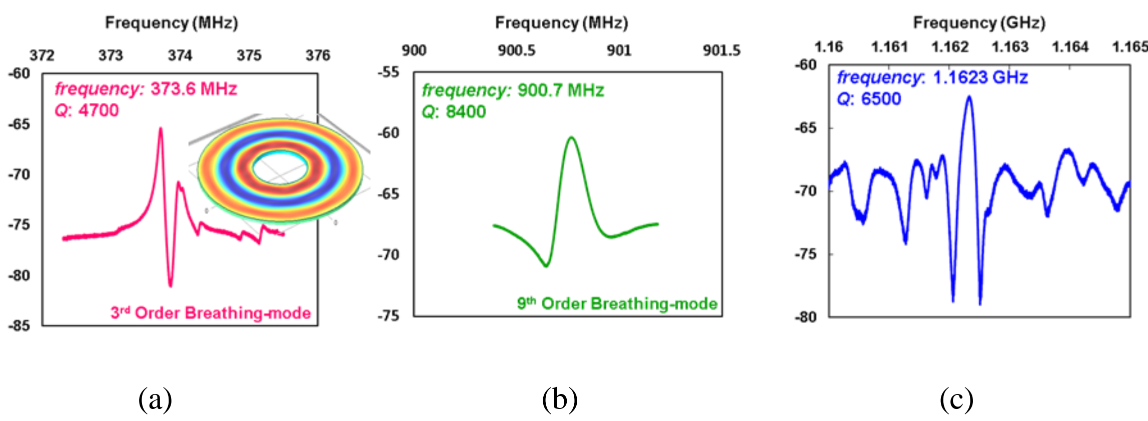

(a) (b) (c)

Figure 3.17 Narrow band resonance frequency of (a) 3rd-order breathing mode at ~373 MHz, (b) 9th-order breathing mode at ~900.7 MHz and (c) highest $f \times Q$ values of 1.05×10^{13} achieved at 1.62 GHz.

Chapter 3: References

[3.1] W. Pan and F. Ayazi, "Thin-film piezoelectric-on substrate resonators with *Q* enhancement and TCF reduction," *IEEE MEMS conference*, Tucson, AZ, Jan. 2008, pp. 727-730.

[3.2] G. K. Ho, R. Abdolvand, A. Sivapurapu, S. Humad, and F. Ayazi, "Piezoelectric-on-silicon lateral bulk acoustic wave micromechanical resonators," *Journal of MEMS*, Vol. 17, No. 2, pp. 512-520, April 2008.

[3.3] R. Abdolvand, H. M. Lavasani, G. K. Ho, and F. Ayazi, "Thin-film piezoelectric-on-silicon resonators for high-frequency reference oscillator applications," *IEEE Transactions on Ultrasonics, Ferroelectrics, and Frequency Control*, Vol. 55, No. 12, pp. 2596-2606, Dec. 2008.

[3.4] H. Chandrahalim, *et al.*, "Influence of silicon on quality factor, motional impedance and tuning range of PZT transduced resonators," *Tech. Dig. Solid-State Sensors, Actuators, and Microsystems Workshop*, Hilton Head Island, SC, June 2008, pp. 360-363.

[3.5] A. Muller, *et al*., "6.3-GHz film bulk acoustic resonator structures based on a GaN/Silicon thin membrane," *IEEE Electron Device Letters*, Vol. 30, No. 8, pp. 799-801, Aug. 2009.

[3.6] K. Brueckner, *et al*., "Two-dimensional electron gas based actuation of piezoelectric AlGaN/GaN microelectromechanical resonators," *Applied Physics Letters*, Vol. 93, No.17, pp. 173504, Oct. 2008.

[3.7] R. F. Milson, D.T. Elliot, S. Terrywood, and M. Redwood, "Analysis and design of coupled-mode miniature bar resonators and monolithic filters," *IEEE Transactions on Sonics and Ultrasonics,* Vol. 30, No. 3, pp. 140-152, May 1983.

[3.8] D. Neculoiu, *et al*., "Microwave FBAR structures fabricated using micromachined GaN membranes," *International Microwave Symposium*, *IEEE/MTT-S*, June 2007, pp. 877–880.

[3.9] W. P. Mason, *Electromechanical Transducers and Wave Filters*, Van Nostrand Co., New York, 1948.

[3.10] A. Ansari and M. Rais-Zadeh, "An 8.7 GHz GaN micromechanical resonator with an integrated AlGaN/GaN HEMT," *Solid-State Sensors, Actuators and Microsystems Workshop (Hilton Head)*, Hilton Head, SC, pp. 295-296, June, 2014.

[3.11] Z. Wu *et al.*, "Piezoelectrically transduced high-Q silica micro resonators," *IEEE Conf. on Micromechanical Systems*, pp. 122-125, 2013.

[3.12] A. Ansari, V. J. Gokhale, V. A. Thakar, J. Roberts, and M. Rais-Zadeh, "Gallium nitride-on-silicon micromechanical overtone resonators and filters," *IEEE Electron Device Meeting (IEDM)*, Washington, DC, 2011, pp. 20.3.1- 20.3.4.

[3.13] A. Ansari and M. Rais-Zadeh, "A Temperature-compensated micromechanical gallium nitride resonator," *IEEE Electron Device Letters*, Vol. 35, No. 11, pp.1127–1129, November, 2014.

Chapter 4 Integration of GaN MEMS, HEMTs and Resonant Body HEMTs

In Chapter 3, we investigated bulk-mode GaN-based MEMS devices theoretically and experimentally. With the goal of building all-GaN monolithically-integrated oscillator circuits, in this chapter, we demonstrate two platforms for intimate integration of GaN MEMS resonators/filters and AlGaN/GaN HEMTs using a fabrication process similar to that of standard GaN HEMTs, with only a final release step added. We show more than 30 dB of transmission modulation by tuning the HEMT biasing points. Next, we introduce a "resonant body HEMT (RB-HEMT)", a more compact alternative for integration of GaN MEMS and HEMTs, operating at multi-GHz regime that combines the sharp frequency selectivity of the resonator with the signal amplification of the HEMT in a single device.

4.1 Intimate Integration of GaN MEMS Resonators and HEMTs: Two Approaches

Two possible approaches are proposed to build a high performance GaN oscillator as the main building block of RF transceivers (Fig. 4.1). In the first platform, a MEMS resonator is co-fabricated and integrated with the GaN circuitry. The second approach is based on a resonant body HEMT (RB-HEMT), a single device that combines the frequency selectivity and high Q of a resonator with the amplification of HEMT.

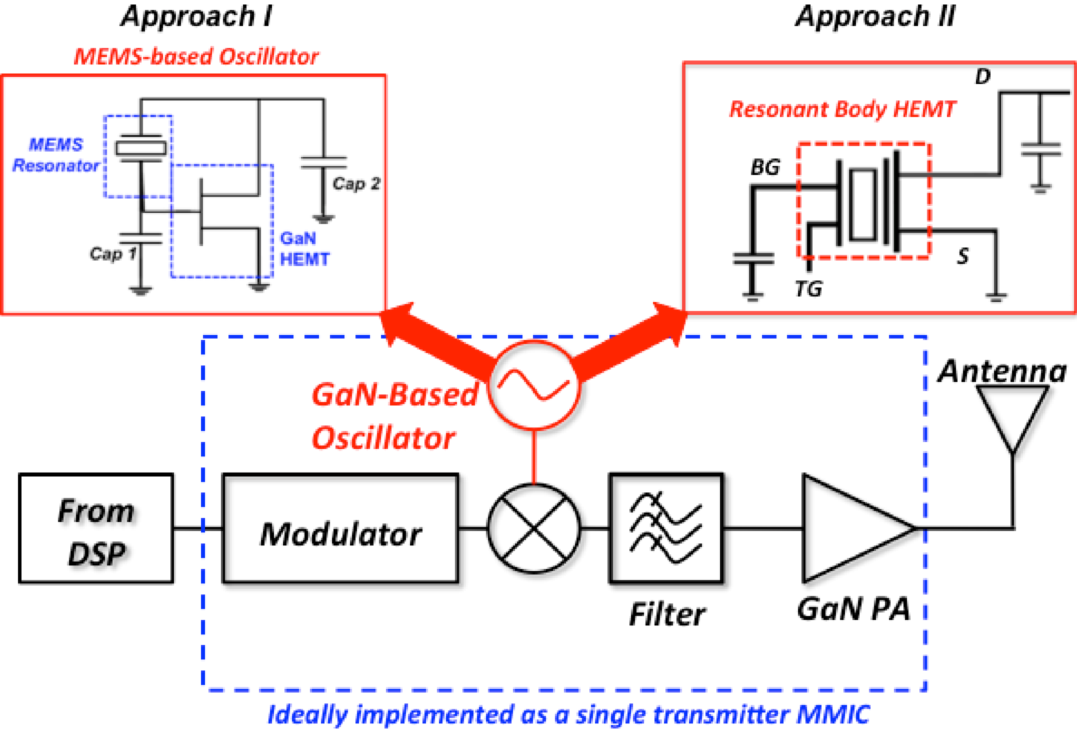

Figure 4.1 A simple transmitter MMIC module, ideally realized in a GaN platform. Two approaches are investigated to realize a GaN-based oscillator: (I) a conventional oscillator configuration (e.g., Pierce oscillator), wherein a MEMS resonator is cascaded with an amplifier and the loop is closed with an addition of a few capacitors if required. (II) Resonant body HEMT (RB-HEMT), where the role of a resonator and a transistor is combined as the main building block of an oscillator.

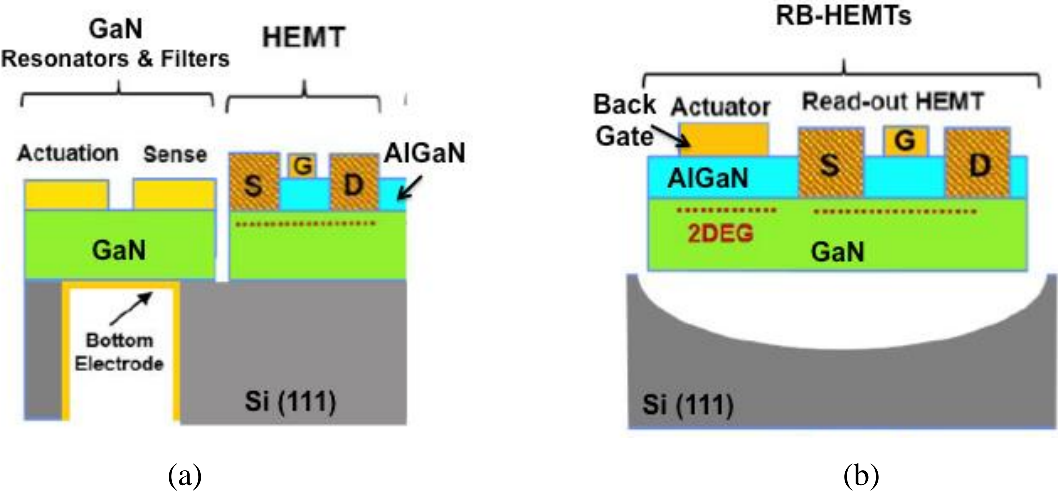

(a) (b)

Figure 4.2 (a) Platform I: a passive bulk-mode resonator is co-fabricated with a HEMT, with the resonator output connected to the HEMT gate. (b) Resonant body HEMT: Confined 2DEG at AlGaN/GaN interface acts as the bottom electrode to actuate AlGaN layer piezoelectrically. Signal is then picked up and amplified by a resonant HEMT.

Approach I incorporates piezoelectric actuation and sensing of GaN resonators, independent of HEMT (Fig. 4.2 (a)). The output of the resonator is fed to the gate of the HEMT, where the electrical signal gets picked up and amplified at the drain. This configuration has several advantages. First, HEMT DC characteristics are set independent of the strain in the resonator; therefore, HEMT characteristics can be tightly controlled and as a result, any type of GaN-based circuitry can be fabricated. For instance, by simply connecting the GaN resonator input to the HEMT drain, a closed loop is formed, in which the resonance can be sustained with the addition of two capacitors connected to the gate and drain to satisfy the Barkhausen criteria (*e.g.*, in a Pierce oscillator configuration) [4.1].

Approach II incorporates a piezoelectric resonant-body transistor, where 2DEG acts as the bottom electrode and is modulated by the acoustic wave launched through Schottky contacts (from a second gate or a piezo actuator). HEMTs, as strain sensors use the exact

same principle of operation; *i.e.* applied strain changes 2DEG mobility and sheet carrier density and thus the drain current [4.2]. In this approach, tuning and amplification of electrical signal can be achieved by different DC biasing of V_{DS} and V_{GS}. Thickness resonance mode can be excited through optimized design of inter-digitated electrodes to modulate the 2DEG channel current. This approach is further explained in detail in the second part of this chapter (Fig. 4.2(b)).

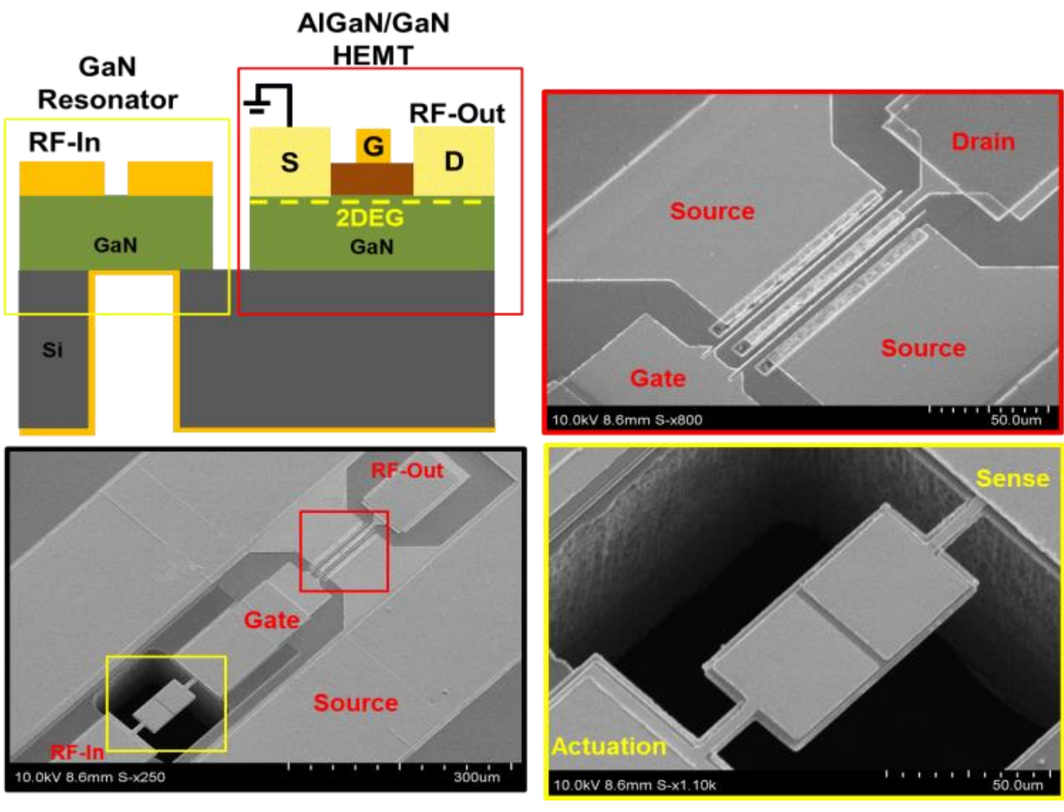

Figure 4.3 An all-GaN integrated microsystem platform wherein GaN MEMS resonators are monolithically integrated with AlGaN/GaN HEMT. Resonator output is connected to the HEMT gate. SEM images of a GaN resonator co-fabricated with a two-gate AlGaN/GaN HEMT. Drain and source are 7 µm apart. Two-fingered gates are each 1 µm long and 100 µm wide. The resonator is a 40 µm × 80 µm resonator.

4.2 GaN Resonator/HEMT Device Modelling

The integration scheme shown in Fig. 4.3 incorporates piezoelectric actuation and sensing of GaN resonators. The output of the resonator is connected to the gate of the HEMT, where the signal gets amplified by the HEMT intrinsic gain ($g_m \times Z_0$), tuned by different DC biasing of V_{DS} and V_{GS}, and finally gets collected from the drain of the HEMT. The equivalent circuit model is shown in Fig. 4.4, which consists of the cascade of a resonator and a HEMT. The resonator is represented with an equivalent modified Butterworth Van Dyke (MBVD) circuit model [4.3].

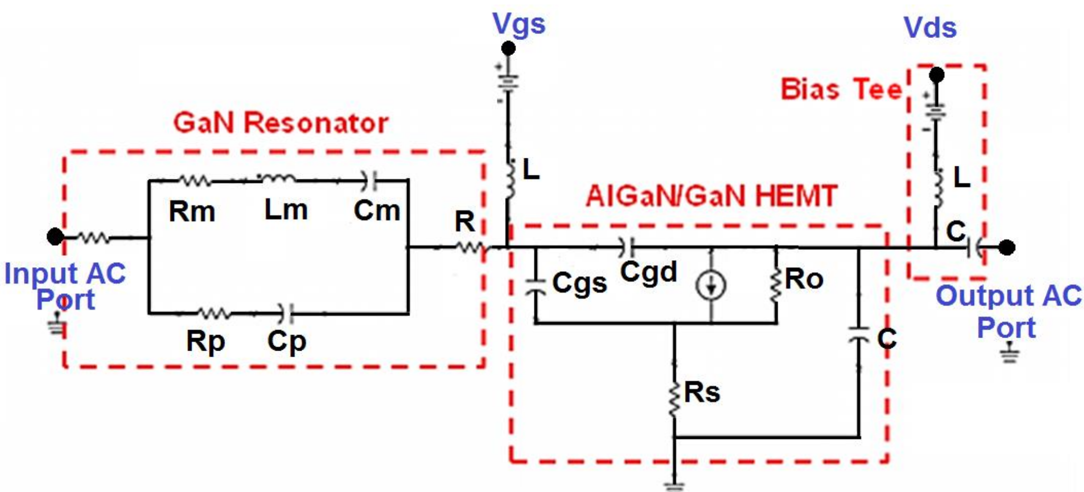

Figure 4.4 Equivalent circuit model of the MEMS resonator cascaded with a HEMT. The output port of the resonator is connected to the gate of the HEMT, where the signal gets amplified and collected at the drain. The inductances connected to the gate and the drain model the Bias Tees.

4.3 HEMT Characterization

In AlGaN/GaN HEMTs, the 2DEG conduction channel exists even with zero gate bias (depletion-mode transistor). The concentration of the 2DEG can be modulated by varying the voltage applied at the gate; thus, a negative DC voltage is applied to the gate of the

transistor to ensure current is confined to the 2DEG channel and the AlGaN barrier layer does not get degraded [4.4]. Static DC I-V curves of a typical two-fingered HEMT with gate length of 1 μm and periphery of 2 × 100 μm are demonstrated in Fig. 4.5 and 4.6 at different temperatures. DC characteristics of HEMTs degrade slightly with an increase in temperature due to an increase in the channel resistance. Unlike Si, AlGaN/GaN HEMTs have been reported to operate at elevated temperatures as high as 600 K [4.5]. Since the channel is formed without any intentional doping and a physical separation exists between parent atoms and the charges that form the 2DEG channel, temperature variations affect the 2DEG sheet carrier density only very slightly [4.6].

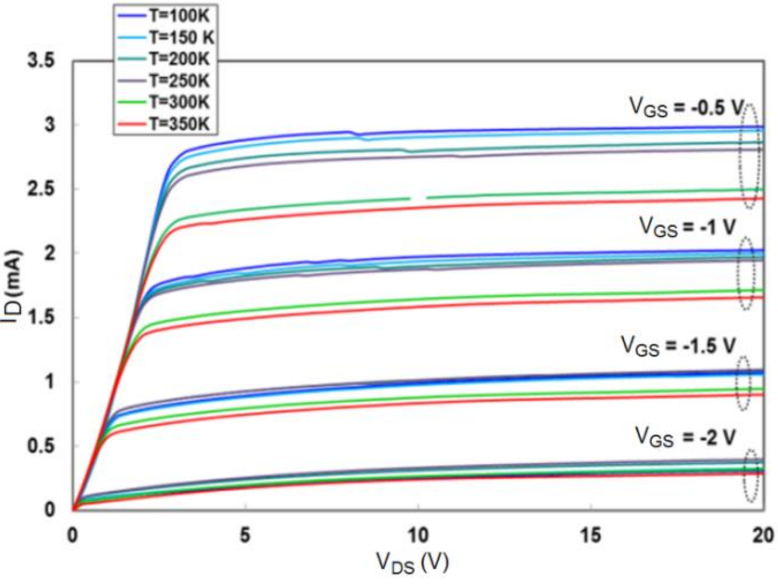

Figure 4.5 DC I-V curves of a two-fingered, 100 μm wide AlGaN/GaN HEMT. Drain current is plotted vs. drain-source voltage, with V_{GS} swept from -0.5 V to -2 V in -0.5 V steps.

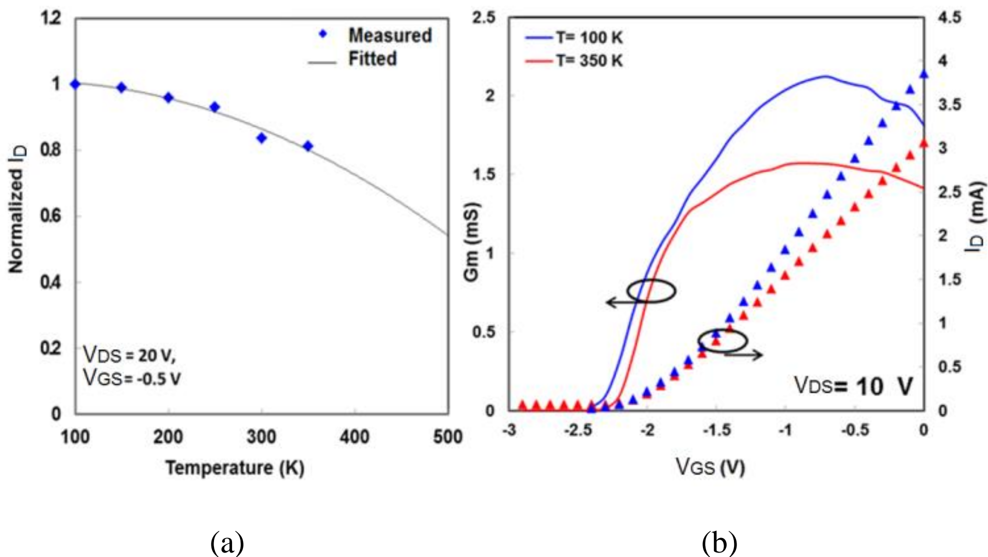

(a) (b)

Figure 4.6 (a) Normalized drain DC current variation over temperature range of 100 K to 350 K with respect to its value at 100 K. T= 350 K as the maximum operation temperature reported here is the measurement tool limit. (b) Drain current and extrinsic trans-conductance *vs.* V_{GS} at 100 K and 350 K for V_{DS} = 10 V.

4.4 Integrated GaN Resonators/HEMT Characterization

Transmission response of the cascaded GaN MEMS resonator/HEMT, shown in Fig. 4.7, are characterized in Figs. 4.8 and 4.9. The large parasitic feed-through capacitance in the piezoelectric resonator is de-embedded from the response using the method discussed in [4.7]. Test devices with the same geometry as the resonators were fabricated but not released from the back side. The test structures were used to de-embed the parasitic feed-through capacitance created by interconnections and pads. More than 30 dB of signal tuning is achieved using a HEMT biased at different DC levels. Further amplification can be achieved with a proper output matching network, a lower loss resonator, and an optimized HEMT design.

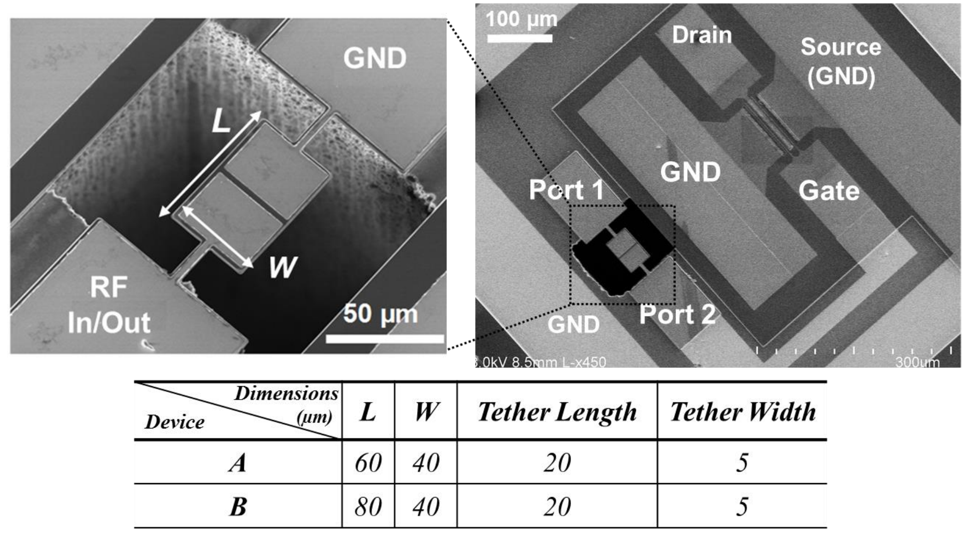

Device \ Dimensions (µm)	*L*	*W*	*Tether Length*	*Tether Width*
A	*60*	*40*	*20*	*5*
B	*80*	*40*	*20*	*5*

Figure 4.7 SEM image of a fabricated GaN BAW resonator integrated AlGaN/GaN HEMT, with the zoomed view of the resonator. The geometry of the fabricated resonators are summarized in the table.

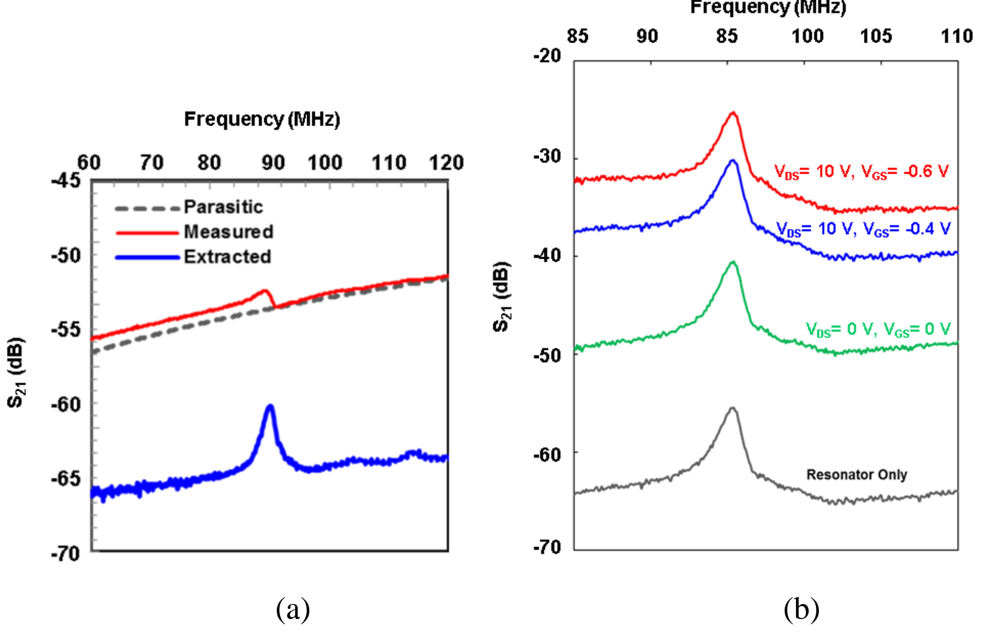

(a) (b)

Figure 4.8 (a) Measured S_{21} response of a contour-mode resonance (red). Unreleased device response is shown in grey and the de-embedded response is shown in blue. (b) Cascaded resonator/HEMT response showing more than 30 dB signal tuning.

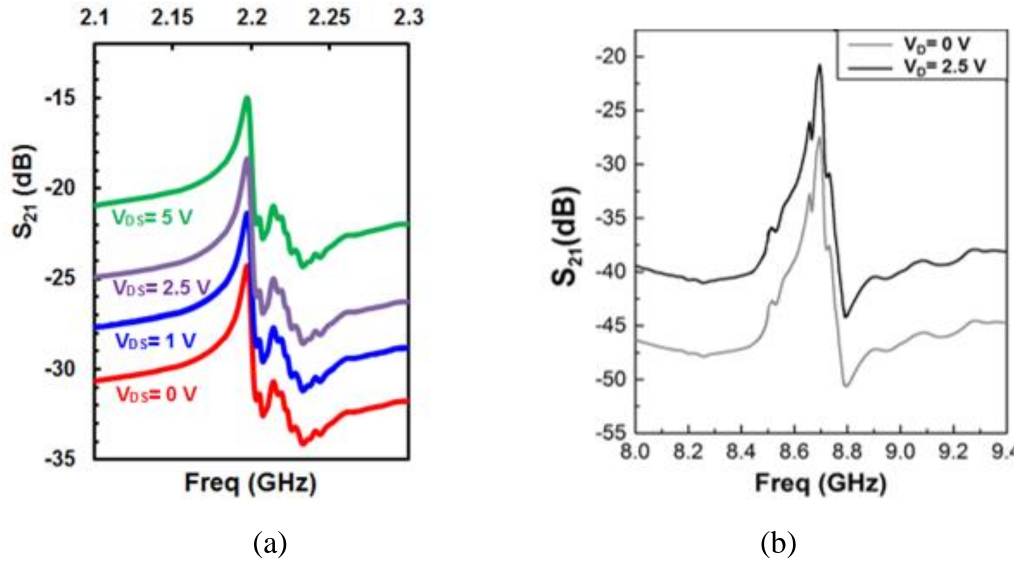

Figure 4.9 (a) Measured S_{21} response of fundamental thickness-mode resonance of a cascaded resonator/HEMT structure. The insertion loss is modulated with various drain DC voltages. (b) The de-embedded fourth-order thickness-mode resonance with ~7 dB of improvement in the insertion loss..

4.5 Temperature Compensation of GaN MEMS Resonators

Similar to silicon and aluminum nitride (AlN), GaN exhibits a negative temperature coefficient of elasticity (TCE), which results in a negative temperature coefficient of frequency (TCF) value. Temperature compensation techniques, although relatively mature in silicon [4.8] and AlN-based piezoelectric MEMS [4.9], had not been shown for GaN BAW resonators until demonstrated by us, recently.

Here, we present a solution already available in GaN HEMT foundry process to reduce/compensate the temperature coefficient of frequency of GaN MEMS resonators [4.10]. We utilize the silicon dioxide passivation layer used for surface passivation of AlGaN/GaN HEMTs [4.11] to cancel out the negative TCE of GaN. Embedding SiO_2 structures at locations of maximum stress depending on the resonance mode can fully compensate the TCF.

Fig. 4.10 shows the temperature trends of the resonance frequency of (a) uncompensated and (b) compensated resonators. The TCF of the uncompensated GaN MEMS resonator is measured to be ~-30 ppm/K, higher than the TCF reported for GaN BAW resonators in [4.12] due to the thicker AlN/AlGaN layer in the stack (TCF_{AlN}~ -25 ppm/K [4.9], TCF_{GaN}~ -18 ppm/K [4.12]), and also the presence of thick gold metal electrodes (10% of the entire stack) with a TCE of ~ -200 ppm/K [4.13]. Furthermore, the property of materials in this specific stack (*e.g.*, different level of doping for unintentionally doped GaN) could affect the resonator TCF. This level of temperature stability is unsuitable for any frequency reference application. Optimized doping and utilizing materials with positive TCE in the stack can reduce TCF values to enable temperature-stable oscillators.

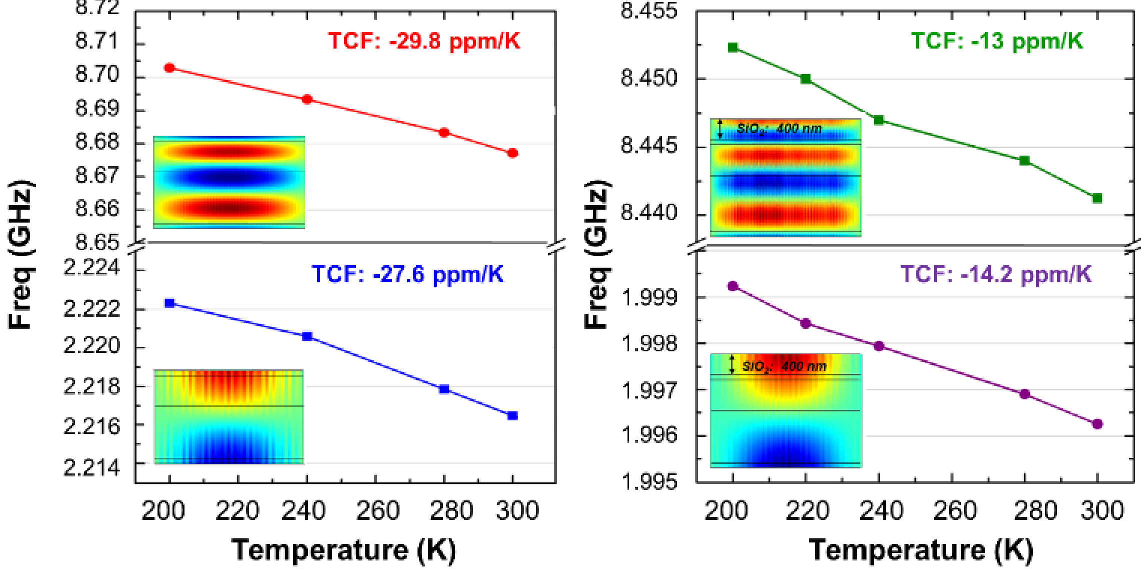

Figure 4.10 Temperature trends of GaN thickness-mode resonator (a) without and (b) with SiO_2 layer. The level of temperature-compensation depends on the stress profile in the location of SiO_2. Lower TCF value achieved for the higher-order mode can be attributed to higher stress levels in SiO_2 for the higher-order resonance mode.

The thickness of the SiO_2 is chosen to optimize the Q and k_t^2 of the resonator. The effect of SiO_2 thickness on k_t^2 and Q of the fundamental thickness-mode is simulated using the Mason's model (Fig. 4.11 (a)). The improvement in the simulated k_t^2 and Q with deposition of ~ 400 nm of SiO_2 can be attributed to the improved distribution of acoustic standing wave energy within the stack. Fig. 4.11 (b) studies the effect of SiO_2 thickness on the TCF, showing that ~650 nm thick SiO_2 can fully compensate the resonator TCF.

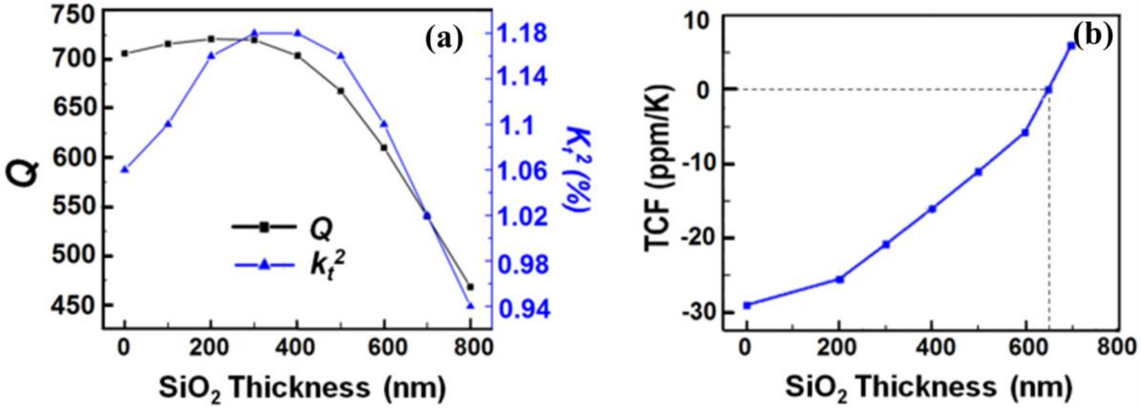

Figure 4.11 (a) Simulated Q and k_t^2 of the first-order thickness-mode resonance of Device B vs. SiO_2 thickness based on Mason's model, taking into account only the acoustic impedance mismatch of the materials in the stack. (b) Simulated TCF vs. SiO_2 thickness, assuming TCE of +160 ppm/K for SiO_2 and -60 ppm/K for the GaN-based stack.

Fig. 4.12 (a) shows the measured admittance response of the fundamental thickness-mode resonance, indicating that deposition of 400 nm SiO_2 slightly improves the resonator Q from 655 to 663 and k_t^2 from 1 to 1.1%. It must be noted that the effect of stress in the thin films is not captured by the Mason's model. Particularly, additional improvement in the measured device performance is expected as a result of stress cancellation with the deposition of SiO_2 layer on the released GaN/AlN stack.

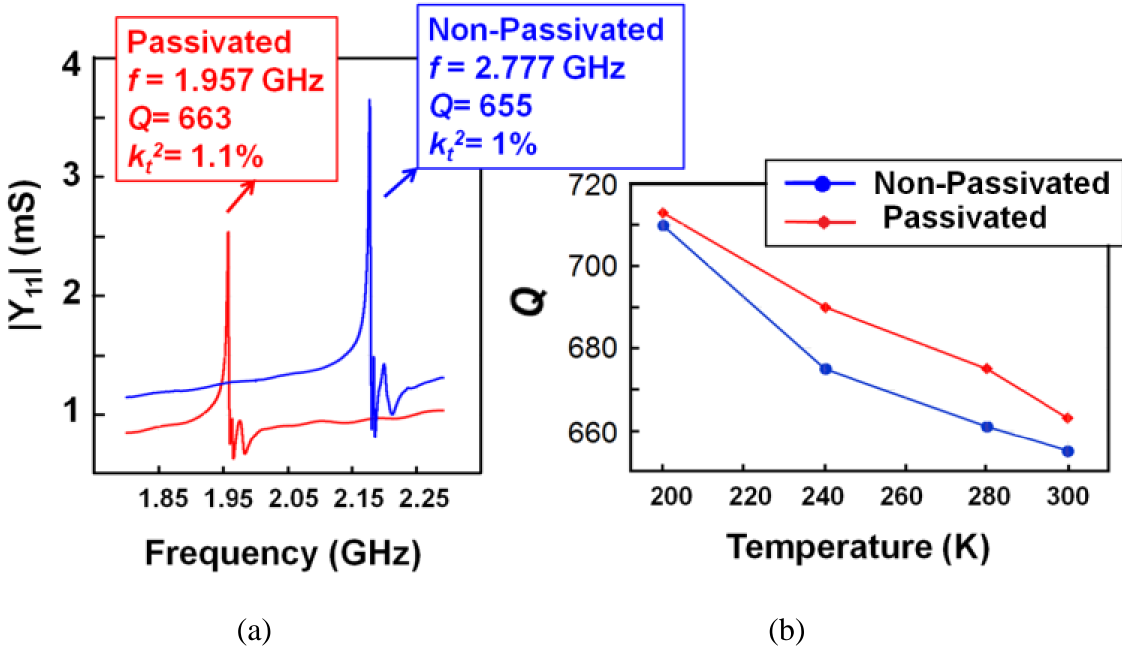

(a) (b)

Figure 4.12 Measured admittance (Y_{11}) plot of the fundamental thickness-mode resonance of Device B, comparing the passivated and non-passivated resonance peaks. Both Q and k_t^2improve with 400 nm SiO_2 passivation. (b) Measured Q vs. temperature of the Device B, showing a reduction of only 7% from T=200 K to T=300 K.

Table IV summarizes the measured performance metrics of the fundamental thickness-mode resonance, verifying that depositing 400 nm of SiO_2 reduces TCF by ~ 50%, improves Q and k_t^2.

Table IV
Summary of measured performance metrics.

Device B	*TCF* (ppm/K)	*Temp* (K)	Q	f_s (GHz)	f_p (GHz)	k_t^2 (%)
Non-passivated	-29	300	655	2.1772	2.1861	1
400 nm-SiO₂ passivated	-15	300	663	1.9576	1.9663	1.1

Significant research in future can be directed on various passive temperature compensation techniques of GaN MEMS resonators as frequency references. Investigations into effects of n- or p-doping of GaN, as well as optimized placement of materials with negative TCE on the TCF of different resonance modes of GaN-based resonators are indispensable in the field of GaN MEMS.

4.6 The Resonant Body Transistor

In this section, we investigate the second approach taken to realize all-GaN multi-GHz oscillator circuits. This is based on a thickness-mode AlGaN/GaN Resonant-Body High Electron Mobility Transistor (RB-HEMT), where we take advantage of the intrinsic HEMT current/voltage sensitivity to small changes in the channel charge. Compared to cascade of a GaN resonator with a HEMT amplifier, RB-HEMTs offer more compact implementation with potentially higher signal to noise ratios at higher frequencies, where capacitive feed-through becomes dominant.

The concept of resonant body or resonant gate transistors (RBTs or RGTs) dates back to the introduction of the MEMS resonators and was coined by Nathanson *et al.*, in 1967 [4.14]. In the past few years, research on RBTs was revived mostly using Si as the resonating material [4.15-17]. One major difference between GaN RB-HEMTs and Si-based RBTs is the origin and the properties of the transistor conduction channel. Spontaneous and piezoelectric polarization due to the lattice mismatch between AlGaN and GaN, create a fixed positive sheet charge at the AlGaN/GaN interface. The positive sheet charge confines electrons at the AlGaN/GaN interface in a potential well, forming a

2DEG channel present at a zero gate voltage (normally ON). The origin of the conduction channel in the III-Nitride HEMT structures suggests that they are very sensitive to mechanical stress, which changes the piezoelectric polarization-induced surface and interface charges. In Si-based transistors, however, the conduction channel is based on creating an inversion layer in the doped substrate by applying a gate voltage, which results in higher scattering due to presence of parent atoms in the channel, higher 1/f noise, lower channel carrier mobility, and more pronounced electron scattering due to imperfections and surface roughness at the non-crystalline Si/SiO_2 interface. Above all, unlike Si-based FETs, GaN HEMTs make it possible to take advantage of piezoelectric actuation inherent in GaN material systems.

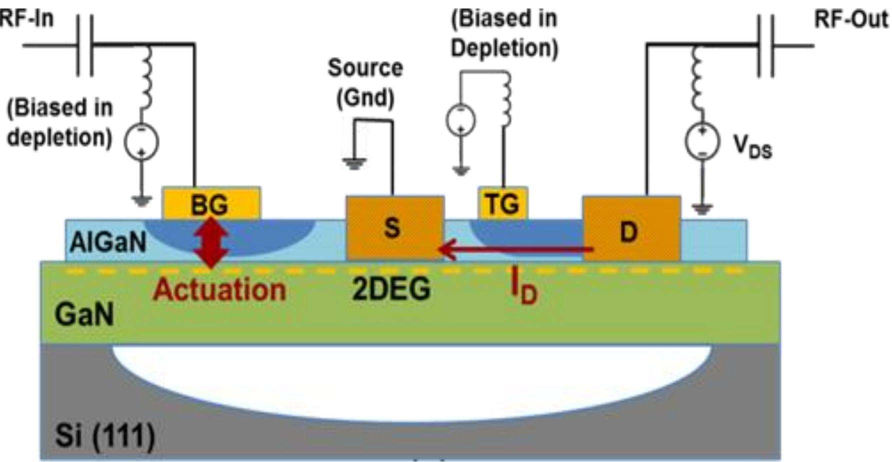

Figure 4.13 Schematic of AlGaN/GaN RB-HEMT. AC signal is applied to the back gate, which is biased in the depletion region (shown as the darker area under the back gate) for efficient transduction. 2DEG, at the AlGaN/GaN interface, acts as the bottom electrode to piezoelectrically actuate the thickness resonance mode of the stack. The 2DEG carrier density is modulated with the induced acoustic strain and reflected in the drain source current (ID).

An AlGaN/GaN Resonant HEMT was first demonstrated in [4.18] and was used to excite the flexural-mode resonance of a beam with frequencies in lower megahertz range. In this work, we propose a single resonating HEMT that not only is the main vibrating element, but also is used to transduce the thickness-mode acoustic resonance (Fig. 4.13). Unlike [4.18] and [4.19], where flexural resonance modes are excited by a HEMT actuator placed at one end of a suspended beam and read out through a separate HEMT at the other end, the proposed device is more compact, has higher electro-mechanical coupling using the thickness mode (e_{33}) piezoelectric coefficient, and operates at higher frequencies. Scanning Electron Microscope (SEM) images of a fabricated RB-HEMT are shown in Fig. 4.14.

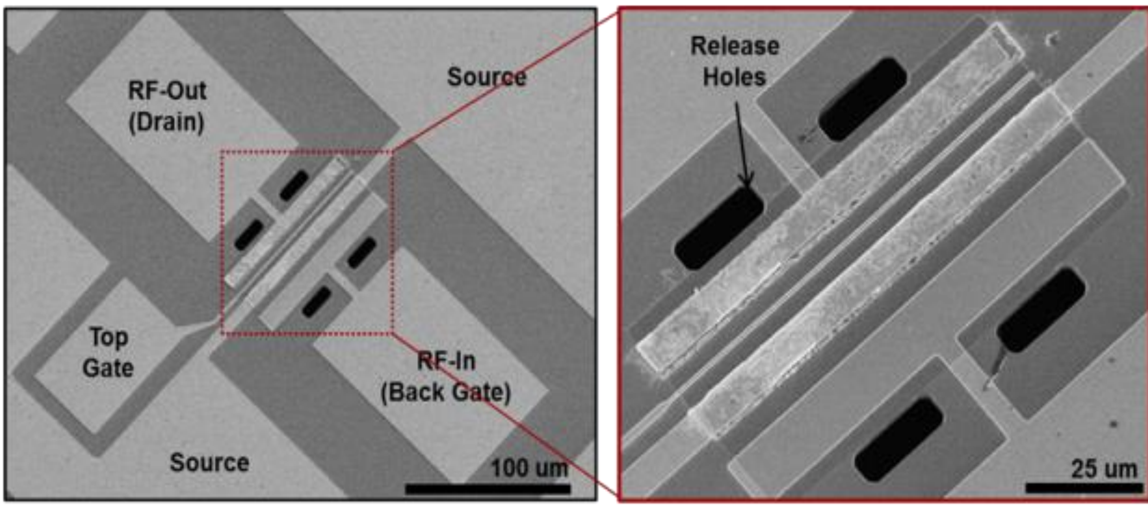

Figure 4.14 SEM images of the AlGaN/GaN RB-HEMT with inter-digitated fingers. Top gate length is 1 μm. The width of source and drain is 6 μm, and the back gate electrode is 8 μm wide.

RB-HEMTs can potentially be used in oscillators and frequency-shifting sensors to realize single-chip GaN-based integrated sensors and systems. The resonance frequency is set by the thickness of the stack and can be trimmed using mass loading or material removal

as in the case of conventional Film Bulk Acoustic Resonators (FBARs) [4.21]. Their fabrication requires no modification to the HEMT baseline fabrication process with the exception of a single release step added as the final stage. These devices require no backside metallization and can be potentially solidly mounted on the substrate using proper acoustic wave reflectors placed underneath the main resonating body, eliminating the mechanical releasing step.

4.7 RB-HEMT Modeling

The proposed RB-HEMT is a four-terminal device consisting of a back gate Schottky contact to launch the acoustic wave into the device, a drain ohmic contact to sense the acoustic resonance, a source ohmic contact tied to zero potential to access the 2DEG channel, placed at a nodal point, and an additional Schottky contact used for electrical modulation of the conducting channel (top gate). The simulated strain along the thickness of the device (z-direction) is obtained using COMSOL multi-physics simulation tool [4.23] in Fig. 4.15. An AC actuation voltage with amplitude of 1 V is applied to the top actuation electrode in the simulation defining the location of the back gate actuation contact. The source ohmic contact is utilized to access the 2DEG channel (bottom electrode), and thus is placed in the middle of the structure with a minimum displacement. The modulated signal is the drain current, picked up from the drain contact. The maximum strain is induced at the top gate-drain region which changes the 2DEG sheet density and is in turn reflected as a change in the drain current.

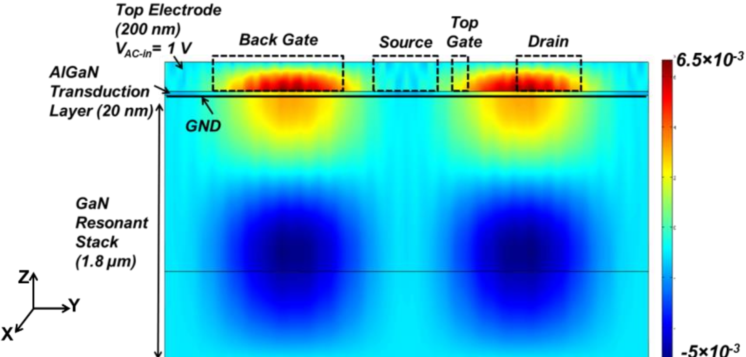

Figure 4.15 COMSOL 2-D simulation of strain in the thickness direction (z), showing the second-order thickness-mode resonance of GaN-based RB-HEMT. The AlGaN piezoelectric transduction layer is sandwiched between the back gate (top metal electrode) and the 2DEG (bottom electrode). The simulation is used to define the electrode layout as shown in Fig. 4.14..

The thin depleted AlGaN layer sandwiched between the back gate Schottky contact and the 2DEG experiences a very high vertical electric field and is responsible for acoustic excitation of the entire 1.8 μm thick AlGaN/GaN stack in the thickness direction, similar to piezoelectric actuation of standard Metal-Insulator-Metal (MIM) structures. The induced strain in the hetero-structure is sensed through a change in the polarization at the AlGaN/GaN interface. The 2DEG channel, under no external strain is originally formed due to a net polarization, composed of two components: (1) piezoelectric polarization in the strained AlGaN layer when grown pseudo-morphically on GaN, (2) spontaneous polarization in AlGaN and GaN layers (Eq. 4.1).

$$+\sigma_B = (P_{SP}^{AlGaN} - P_{SP}^{GaN} + P_{PE}^{AlGaN,Lattice}) , \qquad \text{(Equation 4.1)}$$

where $+\sigma_B$ is the interface sheet charge density, and P_{SP}^{AlGaN} and P_{SP}^{GaN} are the spontaneous polarization in the AlGaN and GaN layers respectively. $P_{PE}^{AlGaN,Lattice}$ denotes the piezoelectric polarization of the thin strained AlGaN layer. Note that there is no

piezoelectric contribution from the 1.8 μm-thick GaN buffer layer, because the lattice of such thick stack is essentially relaxed and no strain is externally applied in this case. The effect of built-in AlGaN strain on the 2DEG sheet density has been extensively investigated in literature [4.2], and in some cases AlGaN/GaN HEMTs have been reported as static strain sensors using the change in the 2DEG sheet charge density expressed by [4.24]:

$$\Delta\sigma_B = (P_{PE}^{AlGaN,mech} - P_{PE}^{GaN,mech}). \qquad \text{(Equation 4.2)}$$

Using the same principle, in this work, we take advantage of the change in interfacial sheet density at the AlGaN/GaN interface to sense bulk acoustic waves at higher frequencies. Using a FET-based sensing, the sensed signal no longer depends on the pick-up electrode area and thus the device dimensions can be further scaled down to realize higher resonance frequencies with higher sensitivities.

Equivalent circuit model of the RB-HEMT is shown in Fig. 4.16. The acoustic resonator is modeled with its Butterworth Van Dyke (BVD) equivalent circuit (R_m, C_m, and L_m). The mechanical branch is located between the back gate and source since the actuation is through the back gate Schottky top electrode and the source ground electrode. The parallel capacitance (C_p) models the parasitic static capacitance of the actuator. It must be noted that the 2DEG sheet is not interrupted between the back gate and the source. The acoustic, g_a, back gate electrical, g_{mb}, and top gate electrical, g_m, transconductances are represented separately. g_a, g_{mb} and g_m are all dependent on the top gate DC voltage, as will be discussed later. g_a is the acoustic transconductance of the RB-HEMT, which has a small off-resonance value and peaks at the resonance frequency. g_{mb} represents the broad-band electrical transconductance from the back gate to the drain.

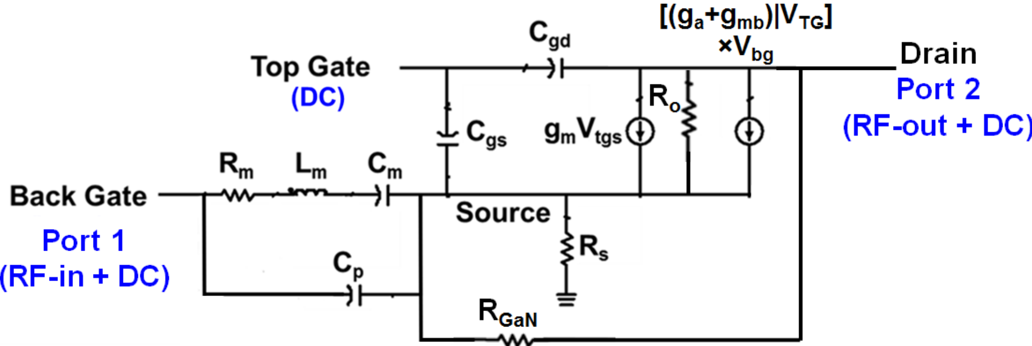

Figure 4.16 Equivalent electrical circuit model of the four-terminal RB-HEMT. AC signal is fed to the back gate and collected from the drain. The actuation takes place between the back gate and the source. The induced acoustic wave modulates the drain current. Values of the acoustic transconductance (g_a) and the back gate transconductance (g_{mb}) both depend on the top DC gate voltage.

4.8 RB-HEMT Measurement Results

DC characteristics of the read-out HEMT are measured using Keithly 4200-SCS parametric analyzer. Radio Frequency (RF) measurements are carried out using an Agilent N5241A PNA with GSG ACP40 probes from Cascade Microtech in a Lakeshore TTPX probe station. Short-Open-Load-Through (SOLT) calibration was performed prior to all measurements. All measurements were taken with 50 Ω termination impedances.

4.8.1. DC Characteristics

As mentioned previously, the back gate Schottky contact is biased in the depletion region to avoid AlGaN layer degradation due to current flow and to limit the conductivity of the AlGaN layer to the AlGaN/GaN interface. DC characteristics of the back gate Schottky contact is shown in Fig. 4.17. The DC characteristics of the HEMT (including top gate, source and drain) are characterized in Fig. 4.18.

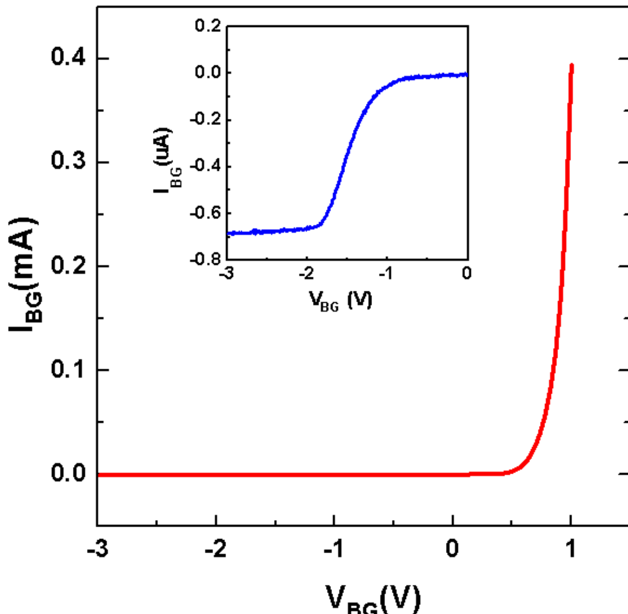

Figure 4.17 Two-port I-V (conductance) measurement between the Schottky back gate and the source ohmic contact. A turn-on voltage of 0.75 V is measured for the Schottky contact. The inset shows the reverse Schottky region of operation, where the back gate is biased at. The back gate voltage of ~ -1.9 V marks the VBG value at which the 2DEG is totally depleted (pinch-off voltage).

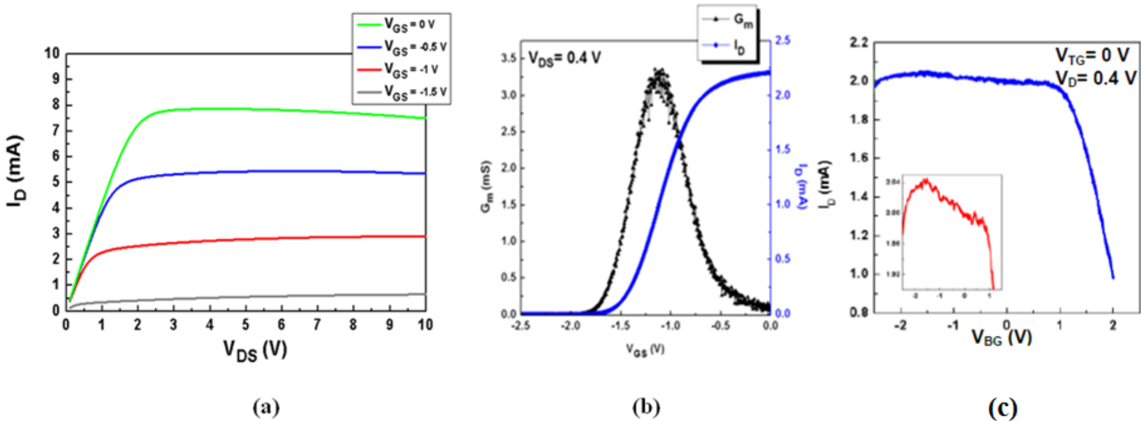

Figure 4.18 DC response of the read-out HEMT, consisting of the drain, top gate, and source (back gate is floating). The gate width is 100 µm. DC I-V transfer curves are plotted as: (a) Drain current versus the drain voltage at different gate voltage values (I_D-V_{DS}). The negative resistance at higher drain currents is associated with self-heating in the AlGaN/GaN HEMT channel. (b) Drain current and transconductance versus top gate voltage at V_{DS}= 0.4 V (I_D-V_{GS} and G_m-V_{GS}). (c) Drain current of the read-out HEMT is plotted vs. the DC voltage of the back gate with the top gate and drain voltage fixed at V_{TG}= 0 V and V_D= 0.4 V.

4.8.2 RF Measurements

The total transconductance of the RB-HEMT is extracted using Eq. 4.3, similar to the case of conventional transistors with the back gate set as Port 1 and the drain as Port 2.

$$|Y_{21} - Y_{12}| = \sqrt{\{Real(Y_{21} - Y_{12})\}^2 + \{Imag\ (Y_{21} - Y_{12})\}^2} \qquad \text{(Equation 4.3)}$$

The total transconductance consists of a purely mechanical component (g_a) and an electrical broadband component (g_{mb}) related to the back gate electrical modulation. Fig. 4.19 shows Y_{21}, Y_{12}, and g_a plots with an input actuation power of Pin= -5 dBm at two different back gate voltages: (a) V_{BG}= 0 V, and (b) V_{BG}= -1.8 V. The back gate-source junction is further depleted in case (b) compared to case (a), resulting in lower Y_{21} and Y_{12} feed-through levels. Furthermore, the acoustic resonance peak only appears in case (b), proving that the back gate Schottky contact acts as the top electrode and the 2DEG as the bottom electrode, with the most effective actuation occurring when the AlGaN layer is depleted and the conduction path is limited to the AlGaN/GaN interface (*i.e.* at V_{BG} = -1.8 V, and V_{AC}= 0.1 V resulting in: $|V_{BG}| + |V_{AC}| \approx |V_{BG\text{-pinch-off}}|$) [4.18]. It is worth noting that large levels of feed-through in the admittance plots are mainly due to the fact that the 2DEG was kept uninterrupted within the resonating device and are mostly canceled out when the acoustic transconductance is extracted. The feed-through level in both Y_{21} and Y_{12} plots can be significantly decreased by etching the 20-nm AlGaN layer from the un-electroded area between actuation and sense electrodes and thus removing the electric coupling between the back gate and the drain contact.

In Fig. 4.19 (c), g_a is extracted by subtraction of the back gate electrical transconductance (g_{mb} = 0.043 mS) from the total transconductance value ($|Y_{21} - Y_{12}|$). g_a rises to ~ 25 µS with a very small off-resonance signal level.

It must be noted that the RB-HEMT acoustic transconductance is measured from the back gate to the drain and does not follow the trend of the read-out HEMT transconductance curve, measured from the top gate to the drain (shown in Fig. 4.18(b)). This can be explained by the transduction mechanism and the physics of the device. The 2DEG carrier density is locally modulated only in the drain access region, where maximum strain is induced (shown in Fig. 4.15). Thus the change in the sheet density is not uniform along the entire HEMT channel. The acoustic transconductance of the fundamental thickness mode resonance is also shown in Fig. 4.19. The acoustic transconductance rises to g_a~ 16 µS when back gate is biased at V_{BG}= -1.8 V.

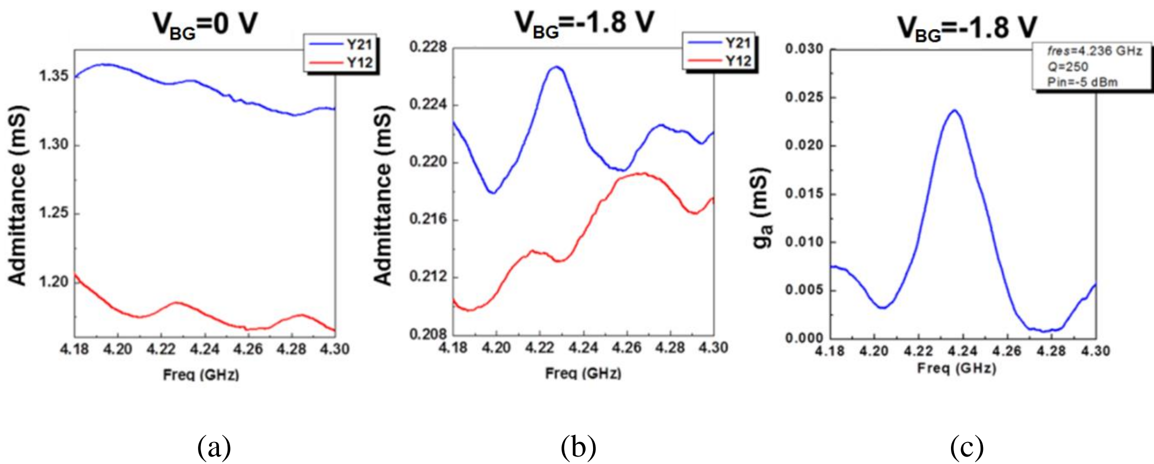

(a) (b) (c)

Figure 4.19 Admittance parameters (Y_{21} and Y_{12}) are plotted at (a) V_{BG}= 0 V and (b) V_{BG}= -1.8 V. The resonance peak only appears in (b) where the 2DEG under the back gate is depleted. (c) The acoustic transconductance (g_a) is extracted from (b). The second-order thickness-mode resonance at 4.23 GHz is excited, with a *Q* of 250 at V_{BG}=-1.8 V. The electrical back gate feed-through floor (gmb= 0.043 mS) is subtracted from $|Y_{21}$-$Y_{12}|$ to plot ga. V_{TG}= -1 V, and V_{DS}= 0.4 V is kept constant in all the plots.

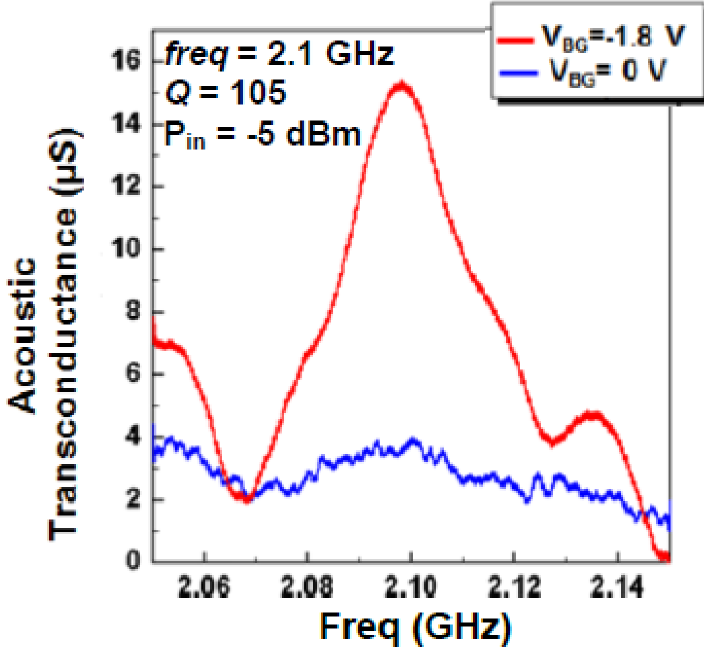

Figure 4.20 Fundamental thickness mode resonance of the RB-HEMT. The acoustic peak only appears when back gate is biased in depletion. The DC voltage on the back gate can act as a switch and turn the acoustic transconductance ON and OFF.

The depletion region between the top gate and the drain grows wider as the voltage difference between them increases, thus narrowing the conducting channel and resulting in lower admittance values between the back gate and the drain. Hence, at a fixed drain voltage, as the top gate voltage approaches more negative values, g_a and g_{mb} both drop. Fig. 4.21 shows the RB-HEMT transconductance dependency on the top gate voltage at V_{DS}= 0.4 V.

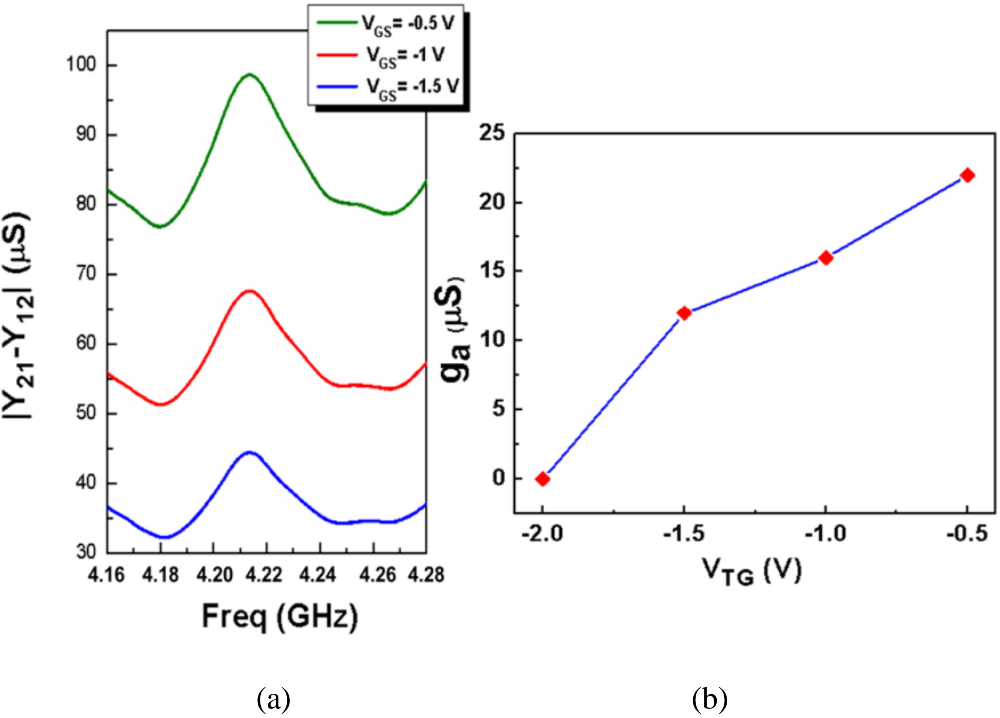

(a) (b)

Figure 4.21 (a) Total transconductance dependency on the top gate voltage (V_{BG}=-1.8 V, V_{DS}= 0.4 V). $|Y_{21} - Y_{12}|$ is plotted at different top gate voltages. The acoustic and back gate electrical transconductance decrease as the top gate DC voltage decreases. (b) Acoustic transconductance is plotted versus top gate DC voltage. The acoustic transconductance drops to zero when the channel is fully depleted (at V_{TG}= -2 V).

Similarly, at a fixed top gate voltage, as the drain voltage increases, the depletion region width increases at the drain end resulting in lower 2DEG carrier concentration, until the channel gets pinched at the drain side (Fig. 4.22(a)). As mentioned before, the detection mechanism relies on modulation of the 2DEG carrier concentration in the top gate- drain region. Therefore, the most effective modulation occurs when the channel under the top gate-drain is conducting. At V_{DS}= $V_{DS(sat)}$, the 2DEG on the drain side gets pinched and its carrier concentration can no longer be modulated by the induced acoustic strain on the drain side; therefore, $|Y_{21}- Y_{12}|$ drops significantly (Fig. 4.22 (c)).

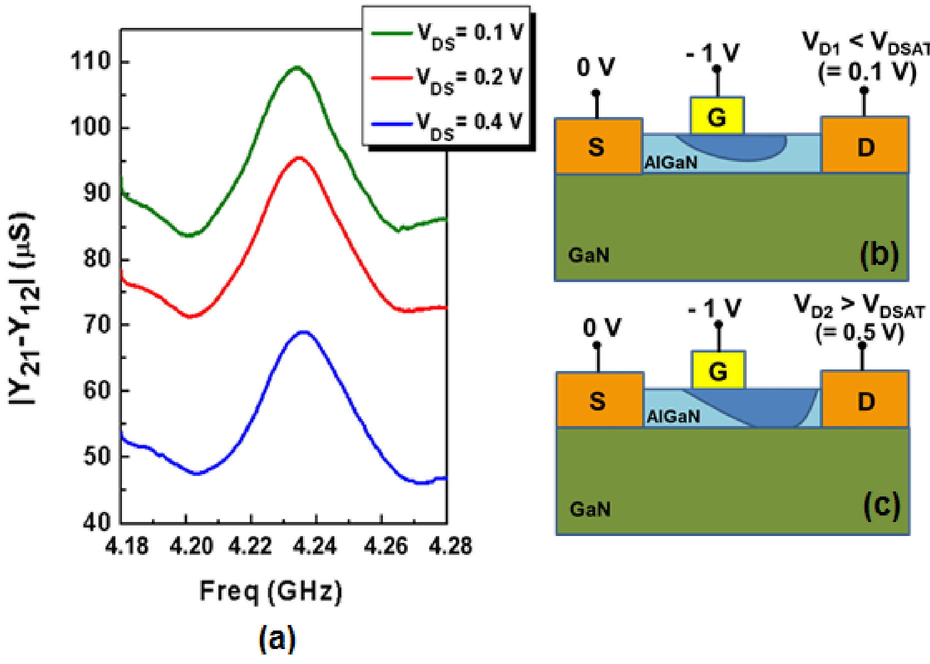

Figure 4.22 (a) Total transconductance $|Y_{21} - Y_{12}|$ at different drain-source voltages in the linear region of operation. (b) The acoustic transconductance decreases as the depletion region grows towards the drain contact at higher V_{DS} values. (c) When the 2DEG under the drain contacts gets pinched (SAT region), the acoustic transconductance value drops to zero. V_{DS}= 0.5 V, corresponds to the knee voltage measured in Fig. 4.7, when V_{TG}= -1 V, marking entering the saturation region of operation. The darker area in the AlGaN channel shows the depletion region, growing at higher V_{DS} values.

Fig. 4.23 shows the dependency of the drain motional current on the input RF power applied to the back gate. As the input AC actuation voltage increases, the strain induced in the hetero-structure increases, resulting in larger polarization and sheet density induced at the AlGaN/GaN interface, and therefore an increase in the motional current. However, the back gate-source depletion width and thus actuator depletion capacitance gets modulated with applied input AC voltage. Particularly, nonlinearity is introduced in the response at larger input AC voltages. At P_{in}= 10 dBm, the acoustic current starts to saturate as shown in Fig. 4.23. Furthermore, the reflection of the incident power from Port 1 of the VNA

determines the effective actuation voltage at the input of the RB-HEMT. Hence, matching conditions vary at different RF input power levels, which is another source of non-linearity in the motional current response.

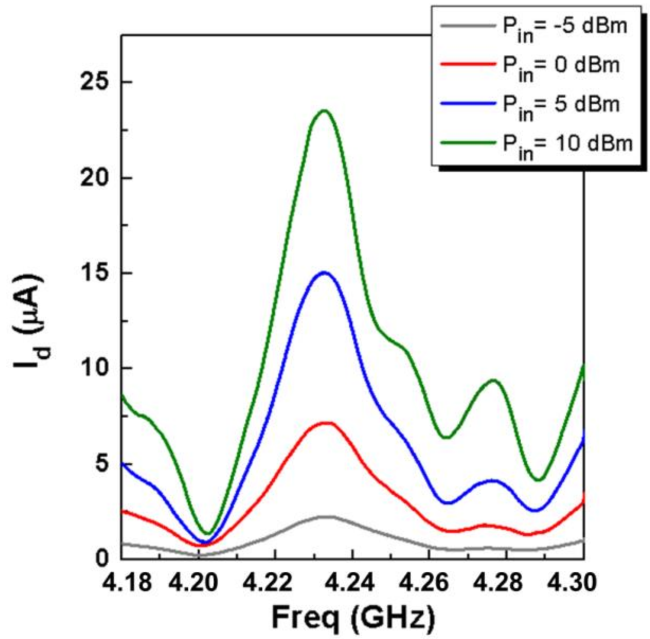

Figure 4.23 Frequency response of the drain motional current ($g_a \times V_{bg}$) of the RB-HEMT. As the input RF power increases, the motional current increases. Nonlinear effects start to show up at higher P_{in} values.

4.9 RB-HEMT Analytical Modelling

In this section the acoustic transconductance is analytically derived and compared to the measurement results. As discussed previously, under external strain, piezoelectric polarization fields in the AlGaN and GaN layer change; therefore, a change in the 2DEG sheet density is expected. Piezoelectric polarization induced along the thickness of a piezoelectric material when a voltage of V_z is applied across its thickness is:

$$P_Z = V_Z \times \varepsilon_0\, \varepsilon_r / d \qquad \text{(Equation 4.4)}$$

With ΔV_Z = 0.1 V applied across the AlGaN actuation layer, AlGaN dielectric constant (ε_r) of 9, and AlGaN thickness (d) of 200 Å, polarization along the thickness of the AlGaN actuation layer is calculated as:

$$P_Z^{AlGaN} = 3.98 \times 10^{-4}\ \text{C/m}^2. \qquad \text{(Equation 4.5)}$$

The induced strain in the thickness direction can be calculated from the polarization field by:

$$\varepsilon_Z = P_Z / e_{33}, \qquad \text{(Equation 4.6)}$$

where e_{33} is the thickness-mode piezoelectric constant, which is estimated for $Al_xGa_{(1-x)}N$ alloy according to Vegard's law [4.24] as:

$$e_{ij}^{AlGaN} = x.\, e_{ij}^{GaN} + (1-x) e_{ij}^{AlN} \qquad \text{(Equation 4.7)}$$

Using piezoelectric constants of GaN and AlN from [4.24] (e_{33}^{GaN}= 0.7 C/m^2, and e_{33}^{AlN}=1.4 C/m^2) and an Al mole fraction (x) of 0.3, e_{33}^{AlGaN} is found to be 1.03 C/m^2.

Therefore the strain in z-direction (ε_Z) in the actuator area is calculated to be 3.86×10^{-4} using P_Z and $e_{33}$of AlGaN calculated above with V_z= 0.1 V, which is about 10× smaller than the simulated strain for V_z= 1 V shown in Fig. 4.15.

The effective induced strain on the sense area (ε'_z), which is smaller than ε_z, creates a polarization in the AlGaN/GaN interface due to their different piezoelectric constants as:

$$P_z = \varepsilon'_z.\left(e_{33}^{AlGaN} - e_{33}^{GaN}\right) + 2\varepsilon'_y.\left(e_{31}^{AlGaN} - e_{31}^{GaN}\right) \qquad \text{(Equation 4.8)}$$

Yielding a change is piezoelectric polarization of $P_{z,interface}$= 1.3 ×10^{-4} C/m^2, or equivalently a sheet density change ($d(n_s)$) of 8 × 10^{14}/m^2. Please note that the first term in Eq. (4.8) is dominant and the in-plane strain is neglected.

As shown in the COMSOL simulation in Fig. 4.15, the strain is induced effectively only at top-gate-drain region, and does not affect the entire channel of the read-out HEMT. Thus, the contribution of each region with a different strain profile in the read-out HEMT is taken into account separately. To find the change in the drain current, we define three regions in the read-out HEMT as the source, drain access regions, and the intrinsic HEMT channel (Fig. 4.24).

The change in the drain current due to change in the channel resistance is:

$$d(I_D) = d\left(\frac{V_{DS}}{R_{ch,ext}}\right) = -d\left(R_{ch,ext}\right) \times \frac{V_{DS}}{(R_{ch,ext})^2}, \qquad \text{(Equation 4.9)}$$

where $R_{ch,ext}$ is the extrinsic channel resistance comprising of:

$$R_{ch,ext} = R_S + R_D + R_{ch} \qquad \text{(Equation 4.10)}$$

R_S and R_D are the source and drain access resistances, and R_{ch} is the intrinsic HEMT channel resistance expressed by:

$$R_{ch} = \frac{L_G}{Wq\mu n_{S,ch}}, \qquad \text{(Equation 4.11)}$$

$$R_S = R_c + \frac{L_{GS}}{Wq\mu n_S}, \qquad \text{(Equation 4.12)}$$

$$R_D = R_c + \frac{L_{GD}}{Wq\mu n_S}. \qquad \text{(Equation 4.13)}$$

L_G, L_{GS}, L_{GD}, are the gate length, gate-source and gate-drain spacing, respectively, shown schematically in Fig. 4.24. As the strain is only induced in the drain-gat region with this design, the change in the external resistance becomes:

$$d(R_{ch,ext}) = d(R_D) = -d(n_S) \times \frac{L_{GD}}{Wq\mu n_S{}^2}\,. \qquad \text{(Equation 4.14)}$$

Thus, Eq. 9 can be re-written as:

$$d(I_D) = d(n_S)\frac{\frac{L'_{GD}}{Wq\mu n_S{}^2}}{\left(\frac{L_{GS}+L_{GD}}{Wq\mu n_S}+\frac{L_G}{Wq\mu n_{S,ch}}\right)^2} \times V_{DS} \qquad \text{(Equation 4.15)}$$

$n_{S,ch}$ is the sheet density in the intrinsic HEMT channel, which is dependent on the HEMT biasing. n_S denotes the sheet density at the drain and source access regions. The mobility used in the above equation is the average electron mobility in the channel at low electric fields.

Note that L_{GD} in Eq. 4.14, has been replaced with L'_{GD} in Eq. 4.15, to account for the depletion width modulation with increased drain voltage. As the drain voltage increases, the depletion region between the gate and drain grows wider and the effective L_{GD} decreases. Thus the sense area or the drain access region in the read-out HEMT decreases, which reduces the $d(I_D)$. Therefore L'_{GD} is defined as the effective gate-drain access region length, taking the effect of depletion width modulation at higher drain voltages into account.

In the linear region of operation, at open channel condition, we assume the sheet density is constant for the three regions of HEMT to calculate the acoustic transconductance. Therefore, the acoustic transconductance, g_a, defined as:

$$g_a = \frac{d(I_D)}{d(V_{BG})} \qquad \text{(Equation 4.16)}$$

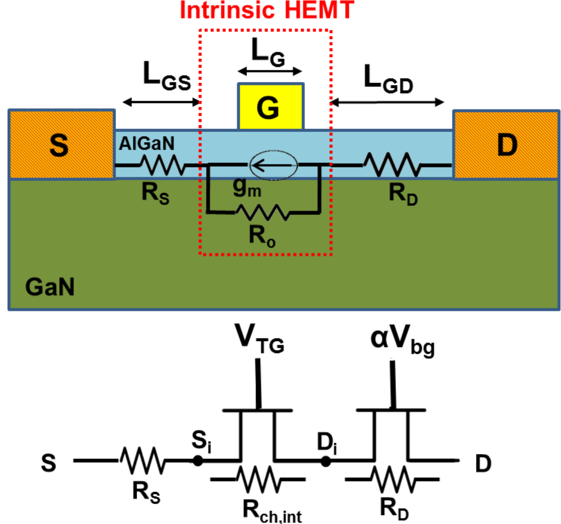

Figure 4.24 (a) Structure of the read-out HEMT, showing the source and drain access regions and the intrinsic HEMT. (b) The external strain in the channel is induced from the back gate actuator, and effectively modulates the sheet density of the drain access region only. The drain access resistance can be equivalently modeled as a transistor [4.25], where the channel resistance is modulated with the back gate voltage. The voltage drop at the drain and source access regions, results in effective voltages of V_{Di} and V_{Si} at the intrinsic HEMT drain and source terminals.

where g_a is calculated to be 32 μS using $L_{GD} = 4\ \mu m,\ L_G = 1\ \mu m,\ L_{GS} = 3\ \mu m,$ average electron mobility $\mu_n = 300\ \text{cm}^2/\text{v.s}$, V_{DS}= 0.1 V, and V_{BG}= 0.1 V. The calculated value of g_a is slightly larger than measurement data for acoustic transconductance (g_a= 27 μS) shown in Fig. 4.21 (g_a). The small discrepancy is attributed to the growth-dependent values of piezoelectric coefficients of GaN and AlGaN, material loss, smaller effective induced strain in the channel at the sense area than actuation, and the fact that the depletion width modulation is not taken into account in our calculations (*i.e.*, $L'_{GD} < 4\ \mu m$). From this analysis, it is clear that in order to get maximum acoustic transconductance, one has to place the drain and source contact across the region of maximum strain.

4.10 Conclusion

A multi-gigahertz RB-HEMT was demonstrated in this chapter, which exhibits a second-order thickness-mode resonance frequency of 4.23 GHz with a *Q* of 250. Co-integrated with GaN ICs, the proposed RB-HEMT can potentially offer all-GaN integrated nano/micro sensors and systems that are the ultimate platforms proposed in this work. The resonance frequency can be further increased by exciting higher harmonics of the thickness mode; however, in our preliminary results because of the large back gate periphery and thus high capacitive and electrical feed-through overwhelming the acoustic transconductance, the frequency was limited to less than 6 GHz. Higher resonance frequencies can be excited by scaling the device dimensions further into the nanometer scale. Furthermore, using an optimized design, the RB-HEMT can operate in the saturation region and take advantage of the intrinsic amplification of the HEMT. The proposed RB-HEMT is the first step towards the realization of a resonant transistor that can offer similar advantages as its Si counterparts but in a piezoelectric GaN-based material system.

Table V compares figures of merit (FoM) of AlGaN/GaN Resonant HEMTs with this work. As mentioned earlier in the chapter, utilizing the thickness-mode resonance allows us to take advantage of the thickness-mode piezoelectric coefficient of GaN (e_{33}), which is larger than the e_{31} coefficient used in contour-mode or flexural-mode resonators and thus translates into larger acoustic transconductance values.

Table V
Comparison of performance metrics of AlGaN/GaN resonant HEMTs.

Ref.	***SEM Image***	***Material***	***Mode***	***Frequency (GHz)***	***Q***	***g_a (μS)***
Durand et al		**Si**	**Flexural**	**0.014**	**700**	**-**
Grogg et al.		**Si**	**Flexural/ Bulk Mode**	**0.071**	**13200**	**-**
Weinstein et al.		**Si**	**Bulk Mode**	**11.7**	**1830**	**15**
Faucher et al.		**AlGaN/GaN**	**Flexural**	**0.013**	**226**	**6**
Popa et al.		**AlGaN/GaN**	**Length Extension**	**2.67**	**650**	**6**
Ansari et al. [TED]		**AlGaN/GaN**	**Thickness Mode**	**4.2**	**250**	**20**
Ansari et al. [IEDM]		**AlGaN/GaN**	**Thickness Mode**	**2.1**	**105**	**16**

Chapter 4: References

[4.1] V. S. Kaper, et al., "High power GaN Monolithic AlGaN/GaN oscillator," IEEE JSSC, Vol. 38, No. 9, pp. 251-254, Sep. 2003.

[4.2] Y. R. Wu, J. Singh, "Polar Heterostructure for Multifunction Devices: Theoretical Studies," IEEE Trans. Electron Devices, Vol. 52, No. 2, pp. 284 – 293, Feb. 2005.

[4.3] MBVD Model

[4.4] D. Ducatteau et al., "Output power density of 5.1/mm at 18 GHz with an AlGaN/GaN HEMT on Si substrate," IEEE Electron Device Lett., Vol. 27, No. 1, pp. 7-9, Jan. 2006.

[4.5] N. Adachi, et al., "High temperature operation of AlGaN/GaN HEMTs," IEEE MTT-S, June 2005, pp. 507-510.

[4.6] M. A. Haque, et al., "Temperature dependent analytical model for current–voltage characteristics of AlGaN/GaN power HEMT," Solid-State Electronics, Vol. 53, pp. 341–348, March 2009.

[4.7] K. E. Wojciechowski, et al, "Single-chip precision oscillators based on multi-frequency, high-Q aluminum nitride MEMS resonators," Transducers'09, Denver, June 2009, pp. 2126-2130.

[4.8] R. Melamud et al., "Temperature-compensated high-stability silicon resonators," Appl. Phys. Lett., vol. 90, no. 24, pp. 244107-1–244107-3, Jun. 2007.

[4.9] C.-M. Lin et al., "Temperature-compensated aluminum nitride Lamb wave resonators," IEEE Trans. Ultrason., Ferroelectr., Freq. Control, vol. 57, no. 3, pp. 524–532, Mar. 2010.

[4.10] A Ansari EDL

[4.11] B. M. Green et al., "The effect of surface passivation on the microwave characteristics of undoped AlGaN/GaN HEMTs," IEEE Electron Device Lett., vol. 21, no. 6, pp. 268–279, Jun. 2000

[4.12] V. J. Gokhale, J. Roberts, and M. Rais-Zadeh, "High performance bulk mode gallium nitride resonators and filters," in Proc. 16th Int. Trans. Conf. Solid-State Sens., Actuators Microsyst. Conf. (TRANSDUCERS), Beijing, China, Jun. 2011, pp. 926–929.

[4.13] Y. Chang and L. Himmel, "Temperature dependence of the elastic constants of Cu, Ag, and Au above room temperature," J. Appl. Phys., vol. 37, no. 9, pp. 3567–3572, Aug. 1966.

[4.14] H. C. Nathanson et al., "The resonant gate transistor," IEEE Transactions on Electron Devices, No. 14, Vol. 3, pp. 117-133, 1967.

[4.15] C. Durand et al., "In-plane silicon-on-nothing nanometer-scale resonant suspended gate MOSFET for in-IC integration perspectives," IEEE Electron Device Letters, Vol. 29, No. 5, pp. 494-496, May 2008.

[4.16] D. Grogg, et al., "Multi-gate vibrating-body field effect transistor (VB-FETs)," IEEE International Electron Device Meeting, San Francisco, CA, Dec. 2008, pp. 1-4.

[4.17] D. Weinstein and S.A. Bhave, "The resonant body transistor," Nano Letters, Vol. 10, No. 4, pp. 1234-37, Feb. 2010.

[4.18] M. Faucher, et al., "Amplified piezoelectric transduction of nanoscale motion in gallium nitride electromechanical resonators," Applied Physics Letters, Vol. 94, Issue 23, pp. 233506, June 2009.

[4.19] M. Faucher, Y. Cordier, M. Werquin, L. Buchaillot, C. Gaquiere, D. Theron, "Electromechanical Transconductance Properties of a GaN MEMS Resonator With Fully Integrated HEMT Transducers," JMEMS, Vol. 21, No. 2, pp. 370-378, April 2012.

[4.20] L. Popa, and D. Weinstein, “Switchable Piezoelectric Transduction AlGaN/GaN MEMS Resonators,” IEEE Transducers, June 2013, pp. 2461-64.

[4.21] H. Campanella, “Tunable FBARs: Frequency Tuning Mechanisms,” Proceedings of the 40th European Microwave Conference, Paris, Sep. 2010, pp. 795-98.

[4.22] A. Ansari, and M. Rais-Zadeh, “HEMT-based read-out of a thickness-mode AlGaN/GaN Resonator,” IEEE Electron Device Meeting, Washington, DC, Dec. 2013, pp. 1-4.

[4.23] COMSOL Home Page. http://www.comsol.com/

[4.24] O. Ambacher et al., “Two dimensional electron gases induced by spontaneous and piezoelectric polarization in undoped and doped AlGaN/GaN heterostructures,” Journal of Applied Physics, Vol. 87, No. 1, pp. 334-344, Jan. 2000.

[4.25] U. Radhakrishna, “A Compact Transport and Charge Model for GaN-based High Electron Mobility Transistors for RF applications,” Master Thesis, MIT, June 2013.

Chapter 5 Depletion-mediated AlGaN/GaN Piezoelectric Resonators and Resonant HEMTs

In this chapter, we introduce "depletion-mediated" piezoelectric transduction mechanism to actuate/sense radio frequency (RF) resonance modes in micro-electromechanical devices based on epitaxially-grown AlGaN/GaN heterostructures. We show that the addition of depletion forces (modulation of 2DEG density) to the piezoelectric transduction force significantly enhances the quality factor (*Q*) of AlGaN/GaN resonators. Furthermore, we study the effect of DC electric field on the characteristics of the depletion layer under Schottky contacts in AlGaN/GaN heterostructures and its subsequent effect on the acoustic properties (Q, k_t^2, $frequency \times Q$, *frequency tuning*). Furthermore, we introduce phonon trap designs realized for the first time in AlGaN/GaN heterostructures to trap acoustic energy in the center of the acoustic cavity and minimize energy leakage to the substrate. Finally, we integrate such depletion-mediated piezoelectric actuators with a resonant HEMT embedded in the center of acoustic cavity to sense and amplify the acoustic resonance modes. The results presented in this chapter, demonstrate the highest $frequency \times Q$ values reported to date for GaN-based acoustic resonators.

5.1 A Brief History

Semiconductor junctions in piezoelectric III-V and II-VI semiconductors have been employed as actuators for a number of years [5.1] and recently there has been renewed interest in their application as actuators for nanomechanical resonators [5.2]. Similarly, depletion forces have been used as micro/nano actuators in PN junctions realized in Si by many groups [5.3-4]. Such transduction mechanism was in fact first discovered when the I-V characteristic of Schottky contacts or PN junction didoes were realized to be highly sensitive to stress [5.5]. This led to implementation of PN junction/Schottky as stress sensors. Later such junctions where utilized as actuators placed on cantilevers embedded in Si material systems. Such transduction mechanism was highly desirable particularly for high-frequency applications because it obviated the need for fabrication of narrow air gaps used in capacitive transduction or embedding a dielectric layer inside Si micromechanical devices in those actuated through internal dielectric transduction.

However, reports on simultaneous depletion and piezoelectric transduction are very few. This is more complicated due to interaction of piezoelectric stress and charge carriers. In [5.2], GaAs-based p-i-n diodes were implemented to actuate NEMS cantilevers. When investigating depletion forces in AlGaN/GaN heterotructures the peculiarities of a 2D quantum well structure need to be taken into consideration. Few groups have reported on bulk and surface acoustic resonance modes based on depletion of AlGaN layer in AlGaN/GaN heterostructures. However, their operation was based on using 2DEG as the bottom electrode and limited to the region wherein the 2DEG is not pinched off [5.6-8]. Our work introduces a transduction scheme based on multi-fingered Schottky contacts on

AlGaN/GaN heterostructures, where the highest performance is achieved under large negative voltages applied to the Schottky, when the 2DEG is pinched off.

5.2 Design and Characterization

There are very few compound semiconductors that possess piezoelectric and piezoresistive properties and can be monolithically integrated with electronic and optoelectronic components. GaN is among a few that not only demonstrates strong piezoelectric effects but can also form 2D quantum-well heterostructures, wherein there is a strong coupling between the electronic band structure and piezoelectric strain. This leads to significant interplay between electric field and mechanical properties of GaN-based piezoelectric acoustic devices, where acoustic properties can be tailored either by doping of GaN thin films, or applying an electric field to deplete the carriers locally.

Here, we investigate the theory and present experimental results, showing the dependency of electromechanical properties of acoustic waves propagating in a piezoelectric media on the resistivity of the piezoelectric material. By modulating the charge carriers in the depletion layer under Schottky interdigitated transducers in AlGaN/GaN heterostructures, upon application of DC voltage, we tune the acoustic properties of bulk-mode resonators.

SEM image and a cross-section schematic of the fabricated AlGaN/GaN resonator is shown in Fig. 5.1 (a,b). The resonator is 70 µm wide, consisting of nine IDT fingers, each 5 µm wide and spaced 3 µm apart. The device operates at its ninth-order width-extensional

resonance mode at ~512 MHz. The mode shape and frequency response of the resonator are shown in Fig. 5.1 (c,d).

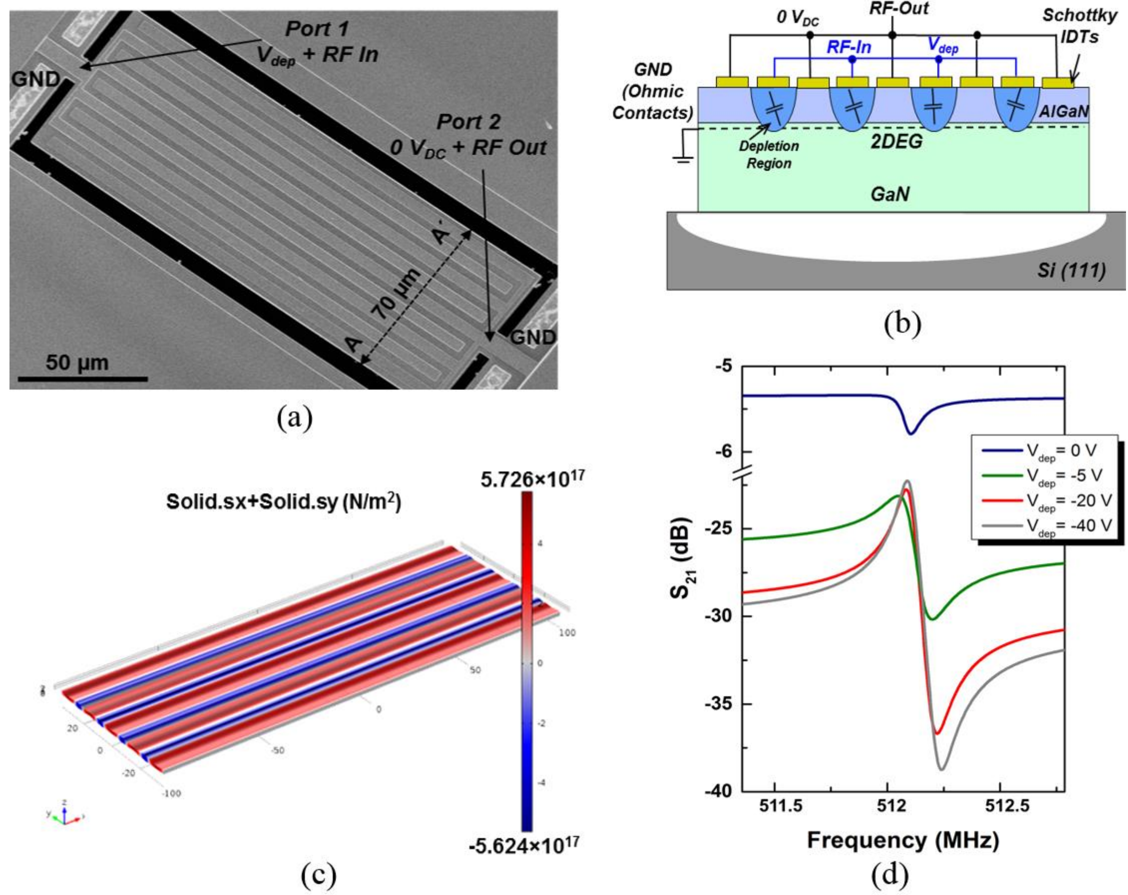

Figure 5.1 SEM image of the fabricated AlGaN/GaN resonator. (b) A cross-section schematic of the depletion-mediated resonator, where the input Schottky IDTs are biased in depletion and the output Schottky IDTs are biased at 0 V_{DC}. Access to 2DEG is provided via Ohmic contacts biased at 0 V_{DC}. (c) COMSOL simulation of the stress profile of the ninth-order width-extensional resonance mode. (d) S_{21} frequency response at P_{in}= -5 dBm when the depletion voltage at the input port is varied from 0 V to -40 V. The voltage at output port is kept at 0 V_{DC}. Mechanical Q increases from 3500 at -5 V to 5000 at -40 V.

5.3 Effect of Electric Field on Acoustic Properties

The dependency of acoustic properties (resonance frequency, electromechanical coupling coefficient (k_t^2), mechanical Q, and $k_t^2 \times Q$) on DC voltage are shown in Fig. 5.2.

To better understand such trends, we characterize the depletion region and study the effect of DC voltage on the depletion capacitance and resistivity of the AlGaN layer and its subsequent effect on the motional properties of AlGaN/GaN resonators. It is worth mentioning that the discussed transduction mechanism is different from Schottky back gate actuation in our RB-HEMT presented in Chapter 4, and other works [5.6-7], where 2DEG is used as the bottom electrode and thus the transduction is switched off when the 2DEG is pinched. Here, we rely on lateral electrical field excitation, thus the larger the depletion layer, the more efficient the transduction is. The dependency of Q and transduction efficiency on the depletion layer will be discussed in detail in the following sections.

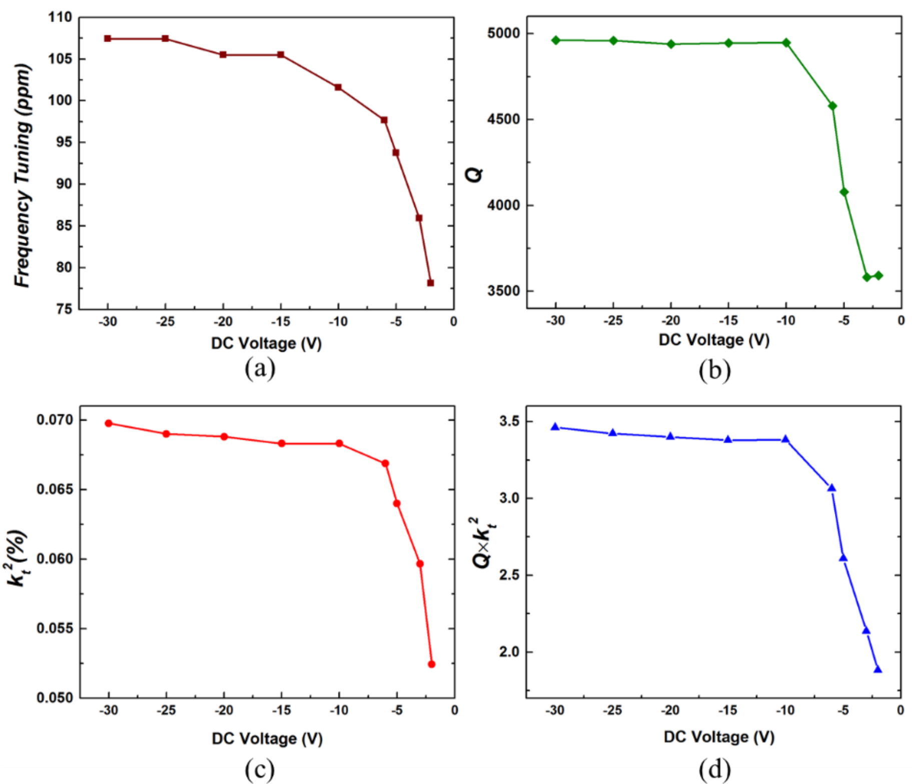

Figure 5.2 Dependency of acoustic properties of piezoelectric resonators on DC voltage. (a) Frequency (or acoustic velocity) tuning, normalized to the resonance frequency at 0 V. (b) electromechanical coupling coefficient (k_t^2), (c) mechanical Q, and (d) $k_t^2 \times Q$ *vs.* DC voltage.

Fig. 5.2 shows that as the 2DEG channel gets mode depleted, the resonance frequency increases, as well as the $k_t^2 \times Q$, which is a figure of merit for acoustic resonators. Fig. 5.3 shows the modified diode-embedded Butterworth Van-Dyke (BVD) circuit model of the AlGaN/GaN resonator to explain the increase in *frequency* and $k_t^2 \times Q$ with DC voltage.

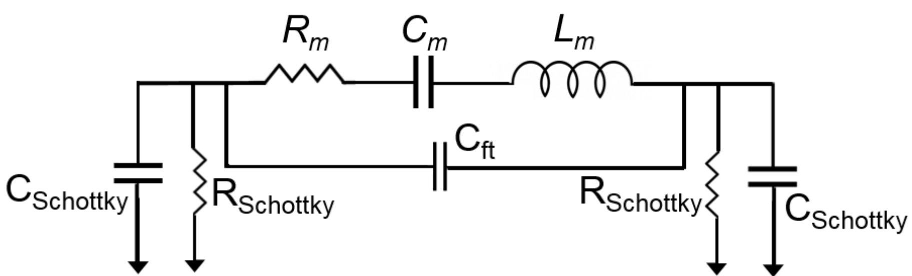

Figure 5.3 Diode-embedded equivalent circuit model of depletion-mediated AlGaN/GaN resonators.

In this circuit model, the motional branch, as well as the electric components depend on the applied electric field. R_m, L_m and C_m for a width-extensional piezoelectric resonator with a width of W, length of L, and thickness of T can be estimated as [5.9]:

$$R_m \approx \frac{\sqrt{M_{eq}.k_{eff}}}{\eta^2 Q}, \quad \text{(Equation 5.1)}$$

$$L_m \approx \frac{M_{eq}}{\eta^2} = [\frac{\pi^4 \rho}{32}\frac{LT^3}{W}\frac{1}{d_{31}^2}]\frac{1}{k_{eff}^2}, \quad \text{(Equation 5.2)}$$

$$C_m \approx \frac{\eta^2}{k_{eff}} = [\frac{16}{\pi^4}\frac{W^2}{T^2}d_{31}^2]\ k_{eff}, \quad \text{(Equation 5.3)}$$

where M_{eq} is the equivalent mass of the acoustic resonators ($M_{eq} = \rho\frac{WLT}{2}$), k_{eff} is the effective stiffness, η is the electromechanical transduction efficiency, or in/output voltage to force transformation ratio. ρ is the density of the resonating material and d_{31} is the piezoelectric coefficient. R_m, L_m, and C_m depend on k_{eff}, which in turn depends on DC

voltage. $C_{Schottky}$ and $R_{Schottky}$ denote the depletion capacitance and resistance of in/output Schottky IDTs, which depend on the applied DC voltage. C-V and DC I-V characteristics of the Schottky contacts are shown in Fig. 5.4.

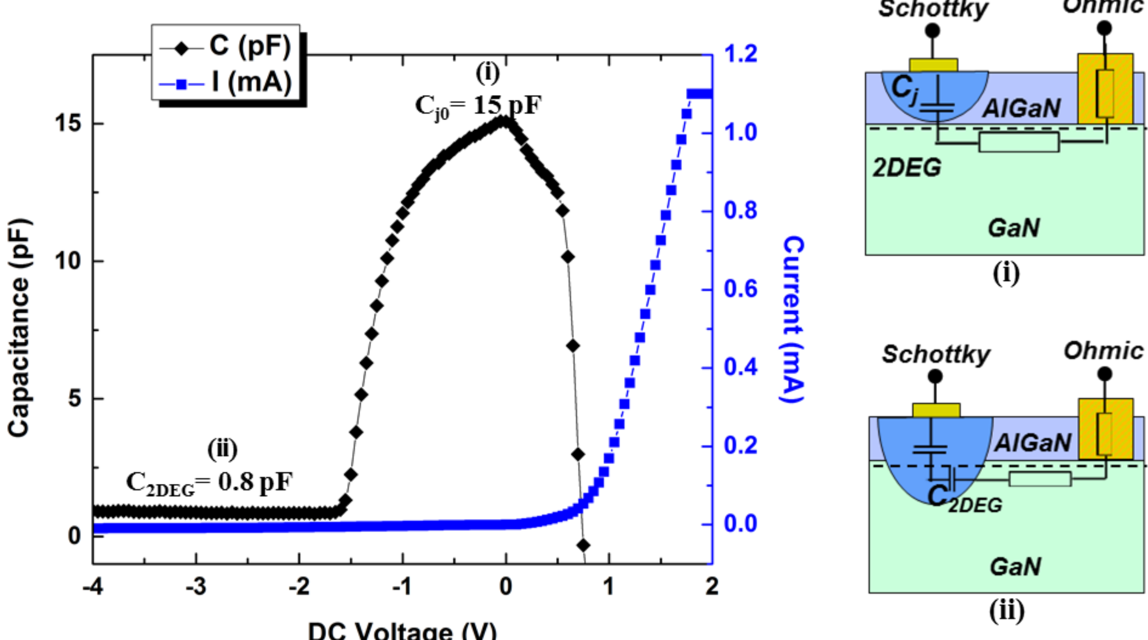

Figure 5.4 Schottky characteristics: C-V (measurement taken at 1 MHz) and DC I-V curves between one Schottky IDT set and Ohmic GND. -1.65 V marks the threshold voltage at which point the depletion region pinches the 2DEG. 0.75 V marks the turn-on voltage of the Schottky diode. In case (i), at zero DC voltage, the depletion layer depth in the z-direction is set by the thickness of the AlGaN layer; in case (ii) the depletion layer has pinched the 2DEG sheet and penetrated into the high-resistivity GaN layer.

Two regimes are observed in the depletion region in the C-V profile shown in Fig. 5.4. In regime (i) the capacitance reflects the effective thickness of the Schottky barrier. As the 2DEG gets depleted and the charge is removed, the capacitance decreases. In regime (ii) the edge of the depletion layer has entered the high-resistivity GaN layer and the capacitance value has dropped significantly due to depletion of the 2DEG channel. Under

zero external voltage biasing, the depletion layer extension in z-direction is determined by the thickness of the AlGaN layer, hence the junction capacitance is:

$$C_0 = C_{j0} = n \times \frac{\varepsilon\varepsilon_0 A}{d}, \quad \text{(Equation 5.4)}$$

where n is the number of Schottky fingers (n=5 for one IDT set), ε is the relative permittivity of the AlGaN layer, reported as (8~9.5) at low frequencies [5.10]. ε_0 is the free space permittivity and A is the area of each finger (5 μm × 200 μm) and d is thickness of the AlGaN layer (20 nm). Plugging in the measured value of 15 pF for C_0 at zero external voltage bias from Fig. 5.4 into Eq. 5.4, the relative permittivity of the AlGaN layer at 1 MHz is derived as 6.8, agreeing well with the reported values in [5.10]. The depletion width (Z_d) under Schottky contact for a uniformly-doped sample is defined as [5.11-12]:

$$Z_d = \sqrt{\frac{2\varepsilon\varepsilon_0}{qN_d}(\Phi_b - V)}, \quad \text{(Equation 5.5)}$$

where q is electron charge, N_d is the carrier density, Φ_b is the barrier built-in potential and V is the applied voltage. It must be noted that in a 2D heterostructure with quantum confinement, the carrier density is not uniformly distributed along the thickness (z-direction) of the AlGaN layer. Thus Eq. 5.5 does not accurately model the extension of the depletion layer in regime (i) in z-direction. First, we take a look at the maximum sheet carrier concentration located at AlGaN/GaN interface for a nominally undoped sample.

$$n_s = \frac{+\sigma}{e} - \left(\frac{\epsilon\epsilon_0}{de^2}\right)\left[e\emptyset_b + E_f - \Delta E_c\right], \quad \text{(Equation 5.6)}$$

where d is the AlGaN layer thickness, $e\emptyset_b$ is the Schottky barrier, E_f is the Fermi level with respect to the GaN conduction band edge energy, and ΔE_c is the conduction band offset at the AlGaN/GaN interface.

In order to gain additional information about the peak carrier concentration and its depth, particular to our AlGaN/GaN heterostructure, we utilize the C-V profile shown in Fig. 5.4 (b) to derive the carrier concentration (N_{CV}) as a function of depth (z_{CV}) in the depletion region based on the method discussed in [5.13-14] as shown in Fig. 5.5 (b).

$$N_{CV} = \frac{C^3}{q\varepsilon\varepsilon_0}\frac{dV}{dC}, \qquad \text{(Equation 5.7)}$$

$$z_{CV} = \frac{\varepsilon\varepsilon_0}{C}, \qquad \text{(Equation 5.8)}$$

where C is the measured capacitance in the C-V profile, when voltage (V) is applied to the Schottky contact. The 2DEG sheet carrier concentration can then be simply calculated as:

$$n_s = \int_{-\infty}^{\infty} N_{CV}(z_{CV})dz_{CV}, \qquad \text{(Equation 5.9)}$$

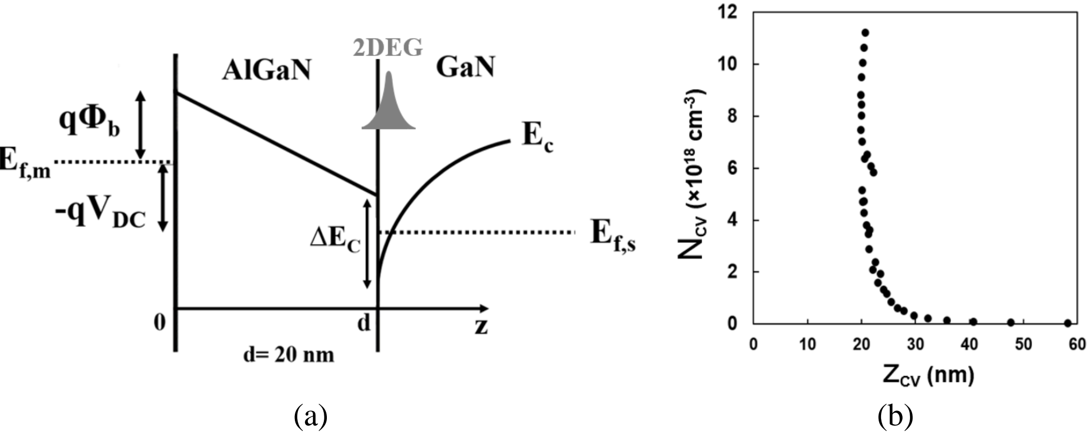

Figure 5.5 (a) Energy band diagram of the AlGaN/GaN hetero-structure under reverse bias condition. (b) Measured 2DEG carrier concentrations *vs.* depth from the C-V profile in Fig. 5.4.

By applying a negative external bias, 2DEG charge starts to deplete. As the value of the negative voltage gets larger, the space charges get more depleted and at V_{th}= -1.65 V the depletion layer will completely penetrate through the 2DEG (pinch-off voltage). In regime (ii) where V_{dep} is smaller than $V_{pinch\text{-}off}$, the measured capacitance drops significantly, due

to depletion of 2DEG charges. In regime (ii), extension of the depletion region in the GaN layer occurs under large depletion voltages and is known to cause reliability issues in AlGaN/GaN HEMTs [5.15]. It must be noted that the lateral extension of the depletion region as well as its further extension into the GaN layer, below the pinch-off voltage is not completely captured in the C-V measurement, explaining further improvement in the acoustic properties of laterally-field excited resonators when $V_{dep} < V_{pinch\text{-}off}$.

5.3.1 Acoustic velocity

It has been shown that the velocity of acoustic wave propagation in a piezoelectric semiconductor is dependent on the resistivity of the medium [5.16]. In [5.16], *White et al.* took advantage of such a phenomenon in surface acoustic waves (SAWs) to build delay lines with variable velocity of transmission by modulating the resistivity of the piezoelectric semiconductor material.

In the width-extensional AlGaN/GaN bulk-acoustic resonator, shown in Fig. 1 (a), the acoustic velocity increases at larger depletion voltages. Fig. 5.2 (a) shows this trend. The increase in the acoustic velocity is attributed to an increase in the effective stiffness of the resonant structure as the AlGaN layer gets depleted of the carrier charges and thus becomes more resistive. Qualitatively, a piezoelectric material with higher resistivity can tolerate a larger electric field, whereas in a conductive piezoelectric material, the effect of the electric field is screened. Since piezoelectric strain depends on the voltage applied to the piezoelectric material, a material with higher resistivity is effectively stiffer than its conductive counterpart under an applied electric field. Hence, larger resonance frequencies and acoustic velocities are expected with larger depletion voltages:

$$\omega = \sqrt{\frac{k_{eff}}{M_{eq}}},\ \upsilon = \sqrt{\frac{k_{eff}}{\rho}}, \qquad \text{(Equation 5.10)}$$

$$k_{eff} = k\left(1 + \frac{K^2}{1+\left(\frac{\sigma}{\omega\varepsilon\varepsilon_0}\right)^2}\right), \qquad \text{(Equation 5.11)}$$

where ω is the fundamental angular resonance frequency, ν is the acoustic velocity, k is the stiffness under super conductivity conditions, K^2 is the electro-mechanical coupling coefficient of the piezoelectric material, σ is the conductivity of the material [5.16].

As shown in Fig. 5.2, the increase in the acoustic velocity is ~108 ppm, translating into ~0.021% of change in the effective stiffness. This rather small tuning is due to the fact that the modulation of the resistivity (and thus stiffness) occurs in the depletion region merely, which comprises only ~6% of the entire GaN-based resonant stack in the thickness direction. In order to significantly modulate the acoustic velocity in bulk-mode resonators, the thickness of the resonator should be thinned down to dimensions in the same order of the depletion width.

Finally, to verify that the added stiffness is indeed due to charge modulation in the depletion layer and distinguish it from the standard piezoelectric frequency tuning with DC bias, we characterize a GaN bulk acoustic resonator in Section 5.4. The standard piezoelectric frequency tuning originates from the dependency of R_m, L_m and C_m on the resonator dimensions (Eqs (5.1-3)), which changes under DC bias, as well as the dependency of d_{31} piezoelectric coefficient on DC bias [5.9]. It is seen that the effect of purely piezoelectric frequency tuning is negligible compared to the effect of k_{eff} tuning in depletion-mediated AlGaN/GaN resonators.

5.3.2 Electromechanical coupling

For efficient electromechanical actuation, it is important to keep the Schottky actuators in the depletion region or in the reverse bias region in the case of pn junctions. Since piezoelectric strain is proportional to the electric field across the junction, lowering the resistance via forward or excessive reverse biasing of the diode screens the electric field and leads to a reduction of actuation efficiency. The dependency of k_t^2 on DC voltage is studied in Fig. 5.2(b). As expected, more efficient transduction is achieved when the actuation layer is more resistive.

Effective electromechanical coupling coefficient, defined as the ratio of the stored mechanical energy to the total input energy, is estimated as:

$$k_t^2 \approx \frac{C_m}{C_0}, \qquad \text{(Equation 5.12)}$$

where C_m is the motional capacitance and C_0 is the total static equivalent capacitance between the input and output ports, setting the feed-through level is S_{21} transmission response. C_m is proportional to stiffness as indicated by Eq. 5.3. In depletion-mediated resonators, both C_m and C_0 change with DC voltage. In fact, the effect of change in C_0 on k_t^2 is more pronounced in the two distinct regimes in the depletion region compared to the effect of C_m change. The transduction efficiency is maximized when the channel is fully pinched and C_0 is minimum.

Using C_m= 0.25 aF from MBVD fitting, and C_0= 0.35 pF from direct C-V measurement between the input and output Schottky IDTs, k_t^2 is extracted as 0.07% at V_{dep}= -30 V, which agrees well with the measured k_t^2 shown in Fig. 5.2(c).

5.4 *Q* Enhancement

It has been shown in [5.17] that Q in bulk-mode GaN resonators depends on DC electric field, via phonon-electron interactions in such materials. Similarly, in AlGaN/GaN resonators, upon application of negative DC voltage to the Schottky contacts, the charge carriers are removed from the surface of the AlGaN layer and thus the loss associated with phonon-electron scattering in piezoelectric semiconductor materials is reduced. Furthermore, an increase in Q is reported when negative DC voltage is applied to Schottky contacts in AlGaN/GaN heterostructures in [5.18], where the Q enhancement is attributed to increased stress in the thin films through an increased piezoelectric actuation of the Schottky barrier. In other words, Q increases due to the added stiffness in such resonators. While all the aforementioned phenomena contribute to Q-enhancement in AlGaN/GaN resonators, in this work, we attribute the significant Q and insertion loss enhancement to a different phenomenon, caused by the depletion forces added to the piezoelectric actuation force, at large negative DC voltages. The dependency of Q on input power further proves that such mechanism is indeed dominant in AlGaN/GaN resonators in this work.

Fig. 5.6 shows the frequency response of the depletion-mediated resonator when driven at input power level of P_{in}= +10 dBm. While the feed-through level is the same for different DC voltages, (unlike Fig. 5.1 (d)), improvement in the insertion loss only occurs at the frequency of resonance. To explain the Q enhancement at high input power levels, we investigate the actuation mechanism of depletion-mediated piezoelectric resonators. Two mechanisms contribute to the actuation of such resonators, (i) the force caused by piezoelectric strain proportional to the z-component of the lateral electric field (E_z): e_{31} =

$E_z.d_{31}$, and (ii) modulation of depletion impedance of the depleted AlGaN/GaN layer [5.2]. The second contributor is negligible at low RF input power levels or low frequencies, however, as the input power increases, the depletion layer changes significantly with the same frequency as the frequency of actuation. Therefore, an electrostatic force is generated and added to the initial piezoelectric force. PN diode resonators based on depletion forces operate based on such mechanism [5.3,4]. Depletion-mediated piezoelectric semiconductors have the advantage of combining both actuation mechanisms, thus improving the *Q* significantly. The added electrostatic force is due to charge modulation upon application of AC voltage to the Schottky contact.

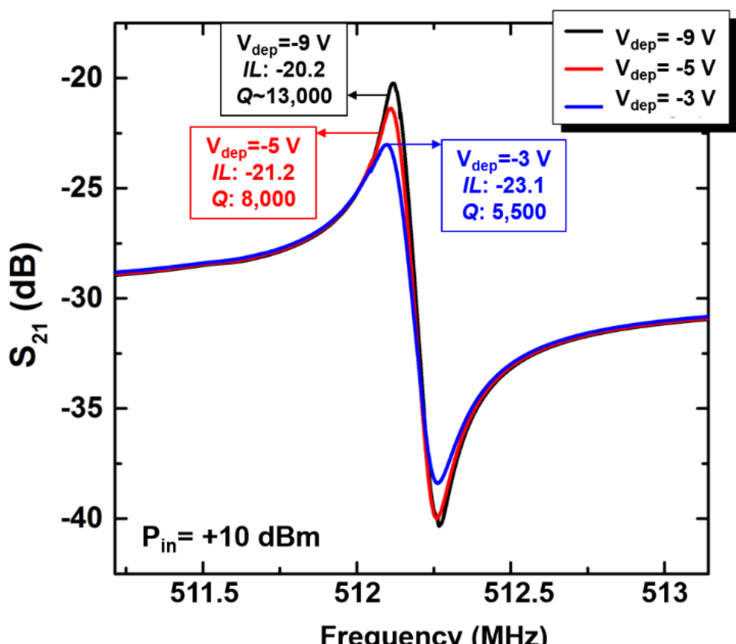

Figure 5.6 *Q* amplification and *IL* enhancement at frequency of resonance for P_{in}= +10 dBm. Modulation of the impedance of the depletion layer with a frequency equal to the actuation frequency creates an electrostatic force, which adds to the piezoelectric force only at the frequency of resonance.

Fig. 5.7 shows the carrier concentration vs. depth from AlGaN surface, when an AC voltage is applied in addition to the negative DC voltage. The depletion width in z-direction is set by AlGaN thickness (20 nm) at zero DC voltage. At a larger negative DC voltage, the carrier density is modulated with AC voltage. The charge modulation gives rise to modulation of electric field and thus electrostatic actuation force. At larger negative voltages, when the 2DEG is fully pinched, the carrier density can be simply estimated as the high-resistivity GaN background carrier density.

The variation of the 2DEG charge density and the depth of the depletion layer is the main source of the actuation force when the 2DEG channel is not yet fully pinched. Since the charge distribution is not uniform in the z-direction, the generated electrostatic force component is derived as:

$$dF(z) = q_v A E dz = q N_{CV}(z) A \frac{\int_{z_d}^{z} q N_{CV}(z) dz}{\varepsilon \varepsilon_0} dz, \qquad \text{(Equation 5.13)}$$

where q_v is the charge per unit volume, N_{CV}(z) is the carrier concentration derived from Eq. 5.6 and A is the area of the depletion layer. z_d and z denote the depth of the depletion layer at V_{DC} and $V_{DC}+v_{AC}$, respectively (Fig. 5.7).

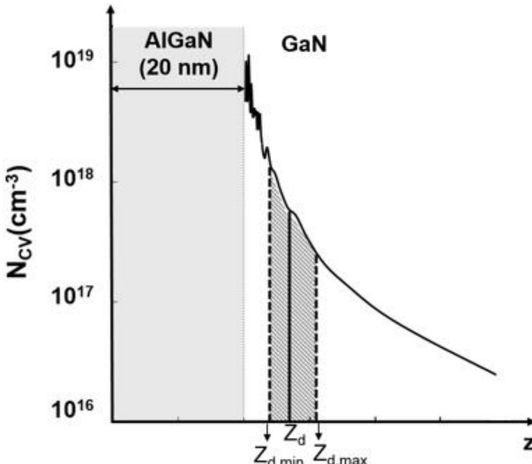

Figure 5.7 Carrier concentration *vs.* depth from the AlGaN surface in AlGaN/GaN heterostructure. The dashed lines show charge modulation when ac signal is applied in addition to a negative DC voltage to the Schottky contact.

In the case of uniform carrier density distribution, we can model the depletion layer actuation force as shown in Eq. (5.13). Such equation is used in pn junction and Schottky actuators reported in [5.3-4]. In the case of AlGaN/GaN resonators, once the depletion layer has fully pinched the 2DEG and penetrated into the GaN layer, Eq. 5.14 can be used to model the depletion force, given that the depletion layer resides in the GaN layer.

$$dF(z) = q_v AEdz = \frac{Aq^2N_d^2}{\varepsilon\varepsilon_0}(z - z_d)dz, \quad \text{(Equation 5.14)}$$

where E is the electric field and Z_d is the depletion width when no ac signal is applied, N_d is the background carrier concentration in the GaN layer and *A* is the area of the depletion layer. Also, such model holds true in AlGaN/GaN resonators for estimation of lateral extension of depletion layer since the charge carrier distribution is assumed uniform in the lateral direction. The carrier concentration would depend on the depth from the AlGaN surface as shown in Fig. 5.7.

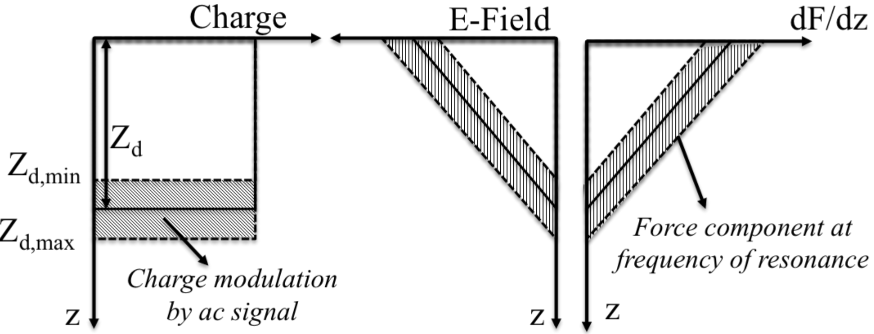

Figure 5.8 Charge, electric field, and force component of depletion-mediated resonators with uniformly-distributed charge carriers. $Z_{d,min}$ and $Z_{d,max}$ denote the minimum and maximum depletion widths when ac signal is applied [5.19].

5.5 Standard GaN piezoelectric resonators with lateral electric field excitation

This class of acoustic resonators are used as control experiments to compare the effect of Schottky contacts in depletion-mediated resonators with standard lateral electric field piezoelectric resonators. These devices have the same geometry as the AlGaN/GaN resonators discussed previously except that 20 nm-thick AlGaN layer is removed by a chlorine-based plasma etch. GaN layer is used as the active piezoelectric layer where two sets of IDT electrodes are deposited on top of it. Since there is neither a bottom metal electrode, nor the 2DEG sheet, Ohmic contacts for accessing the ground bottom electrode are not required in this case. The ninth-order width extensional resonance mode is shown in Fig. 8(a) and is at a slightly higher resonance frequency of 520 MHz due to reduction of the resonator mass by removal of the AlGaN layer as shown in Eq. (5.1).

DC voltage affects the stiffness and permittivity of any piezoelectric material (not only piezoelectric semiconductors) and hence their resonance frequency. To separate this effect

from the frequency tuning in depletion-mediated resonators shown in Fig. 5.2(a), we study the effect of DC voltage on a standard GaN resonator in Fig. 5.9. The frequency tuning shows a linear trend and is only ~17 ppm at -40 V. This shows that depletion-mediated resonators are able to modulate the stiffness of the resonant stack more efficiently than their purely piezoelectric counterparts. Due to the combined depletion and piezoelectric actuation force, Q and insertion loss of the depletion-mediated piezoelectric resonators are more sensitive to DC voltage as compared to the pure GaN resonators. The dependency of Q of standard GaN resonators on DC voltage is attributed to reduction of charge trapping effects as well as removal of charge carriers upon application of DC voltage. This reduces the loss associated with phonon-electron scattering in piezoelectric semiconductors.

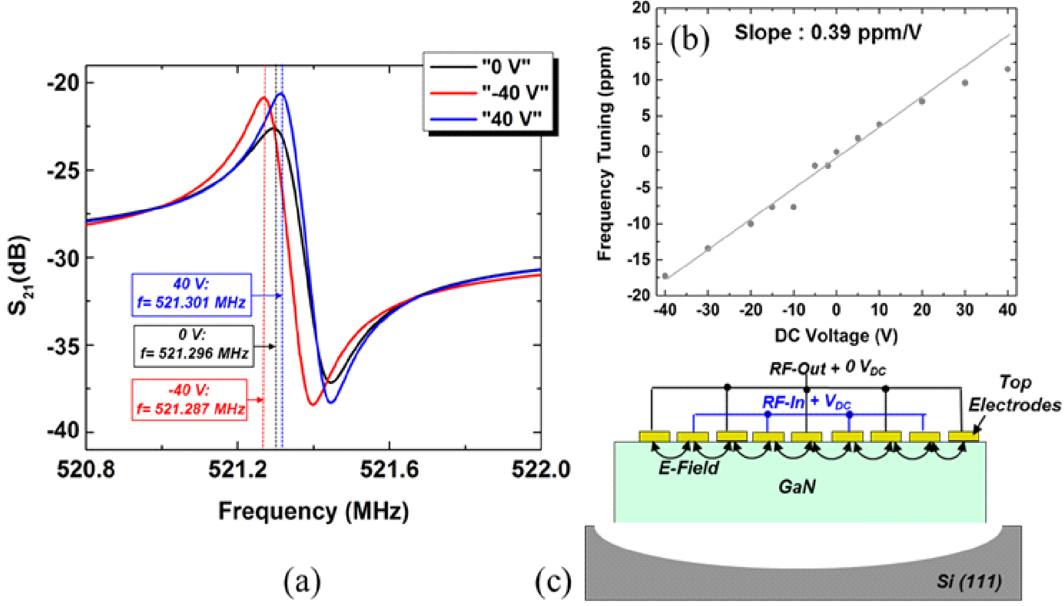

Figure 5.9 (a) S_{21} frequency response of the ninth-order width-extensional resonance mode of GaN resonator when 2DEG is removed. The voltage applied between two adjacent electrodes are -40 V, 0 V and +40 V. (b) Small fractional resonance frequency change with applied DC voltage. The slope of the frequency tuning *vs.* DC voltage is 0.39 ppm/V, corresponding to piezoelectric tuning effect. (c) Cross section schematic of the lateral-field-excited GaN resonator.

5.6 Optimization of the geometry of acoustic cavity

Up to this point, in this chapter, we investigated the depletion-mediated piezoelectric transduction scheme in detail and studied the inter-relation between the acoustic properties and electric field in AlGaN/GaN bulk-mode resonators. In order to further improve the performance of such resonators, we look into different ways to engineer the geometry of the acoustic cavity for optimized performance.

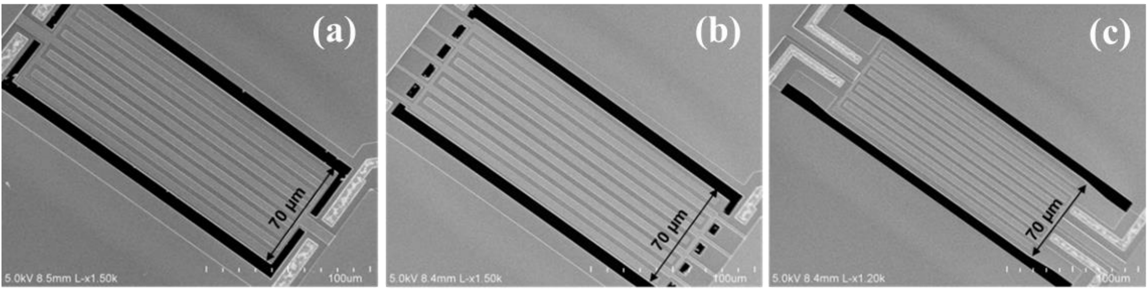

Figure 5.10 SEM images of a ninth-order width-extensional mode resonator with (a) single narrow tethers, and (b) multiple tethers. (c) “Phonon trap” design, where narrow tethers do not exist.

One of the well-known dissipation mechanism that limits *Q* of MEMS resonators is the anchor loss. Care must be taken in designing acoustic cavities to place the anchors at nodal points or locations with minimal displacement to minimize disturbing the mode shape. Many approaches have been taken so far to this end [5.20]. Narrow tethers have been traditionally used in MEMS community, later, multi-tethers were proved to enhance *Q* and power handling. Here. We utilize tapered contours where the need for narrow tethers are obviated. This was shown in other material systems and used to tailor the frequency-temperature trends of micromechanical resonators [5.21].

The geometry of acoustic cavities has been engineered to efficiently trap the energy in the central region of devices, where the interdigitated excitation/sense electrodes are located. Such an energy trapping method facilitates routing of multiple lines. Furthermore, elimination of narrow tethers improves the power handling capability of the GaN resonators, making them suitable for high-power applications. The devices discussed operate in the ninth-order width-extensional mode that is excited and sensed using Schottky IDTs.

5.7 Phonon Trap Design

The distribution of laterally-polarized phonons are engineered to trap the energy in the central part of the acoustic cavity and far from the substrate; therefore eliminating the need for narrow tethers while substantially reducing anchor leakage. This facilitates integration of multiple IDT sets and HEMT read-outs on a single device, as shown in Fig. 5.11.

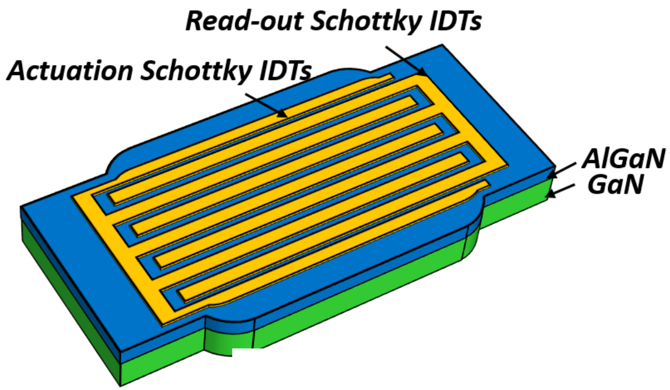

Figure 5.11 Schematic of a ninth-order width extensional phonon trap using Schottky IDTs to actuate and sense acoustic resonance modes.

Acoustic engineering of the device geometry [5.21] has been done using the dispersion characteristic of the 9th-order width-extensional laterally propagating wave in an AlGaN/GaN/AlN waveguide. The substrate used in this work is composed of a stack of AlN, $Al_xGa_{(1-x)}N$ and GaN layers. Since the acoustic properties of the transitional $Al_xGa_{(1-x)}N$ layer is unknown, this layer is simulated as a stack of several layers with acoustic properties approximated by a linear combination of that of AlN and GaN. Fig. 5.12 shows the dispersion curve of the 9th width-extensional branch for different widths. Decreasing the width of the waveguide moves the dispersion curve into higher frequencies. When a central waveguide is flanked with gradually decreasing widths, a synthesized solution may exist, resulting from coupling of the propagating waves in the central region and evanescent waves in the flanks. This is schematically shown in Fig. 5.12, where the synthesized solution is indicated by the line intersecting the dispersion curves of constituent waveguides marked by stars.

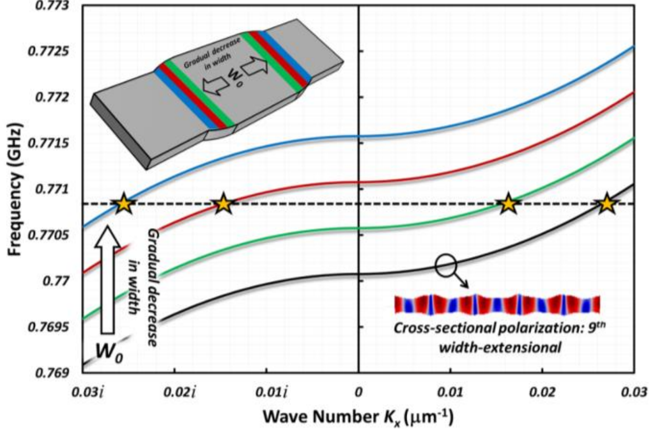

Figure 5.12 Dispersion characteristic of the 9th width-extensional mode for different widths, along with the schematic demonstration of the acoustic engineering concept for phonon trapping.

The exponentially decaying energy of the evanescent wave results in energy concentration in the central part of the cavity and far from the substrate. Therefore, the cavity can be anchored to the substrate through wide tethers. While this substantially relaxes the power handling limitations defined by narrow tethers, such wide anchors facilitate integration of multiple electrically isolated piezoelectric transduction ports as well as HEMT read-out lines. Fig. 5.13 and 5.14 show the simulated mode shape and the SEM of the device.

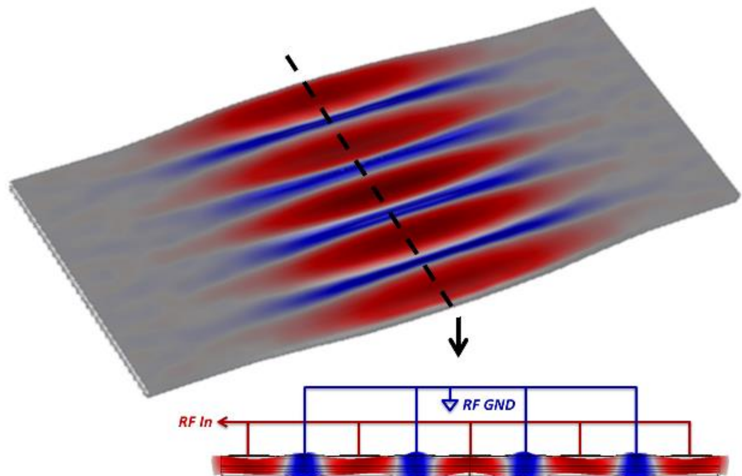

Figure 5.13 Simulated synthesized mode shape of the phonon trap along with its cross sectional polarization and the proposed lateral-field excitation scheme.

5.8 Device Characterization

The S_{21} frequency response and its dependency on DC voltage, and the power handling and temperature trends of AlGaN/GaN phonon traps are characterized in this section.

5.8.1 Frequency Response

The measured frequency response is shown in Fig. 5.15. When 0 V_{DC} is applied to one set of the Schottky IDTs, the depletion region is very small and therefore the piezoelectric

transduction is highly inefficient. As we increase the magnitude of the DC voltage applied to the Schottky IDTs, the 2DEG channel gets further depleted and the *Q* significantly increases. While at 0 V_{DC}, the *Q* is low due to large feed-through and inefficient piezoelectric transduction, at V_{DC}= -9 V, a record high *Q* of 13,122 is measured at the resonance frequency of 740.75 MHz. Fig. 5.15 summarizes the frequency response of the device for different V_{DC} values.

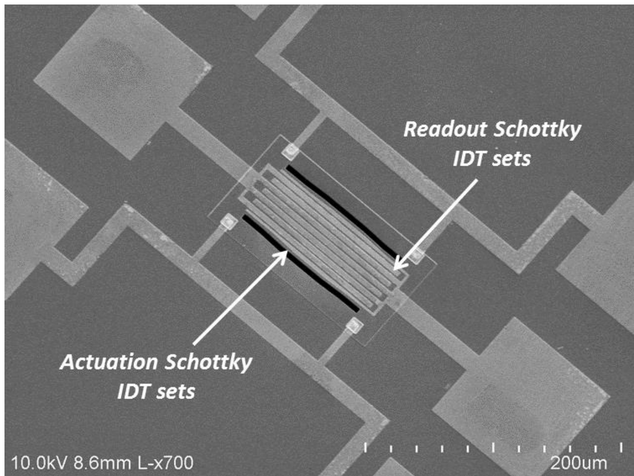

Figure 5.14 A SEM image of a fabricated piezoelectric lateral field-excited AlGaN/GaN resonator. DC voltage is applied to one set of the Schottky IDTs for a more effective acoustic transduction. The device is designed to resonate at its 9th-order width-extensional mode.

5.8.2 Power Handling Capabilities

One of the biggest advantages of GaN is its suitability for high power applications, therefore it is necessary to characterize the power handling capabilities of GaN MEMS devices for future integration with other GaN components. Fig. 5.16 shows the frequency response of the 740 MHz phonon trap at various input power levels.

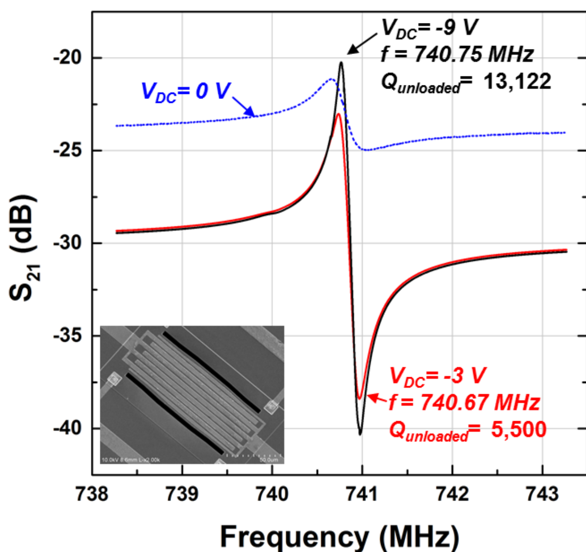

Figure 5.15 Measured S_{21} response at room temperature. A record high Q_{unloaded} of 13,122 is extracted from the measured phase of S_{21} when V_{DC}= -9 V.

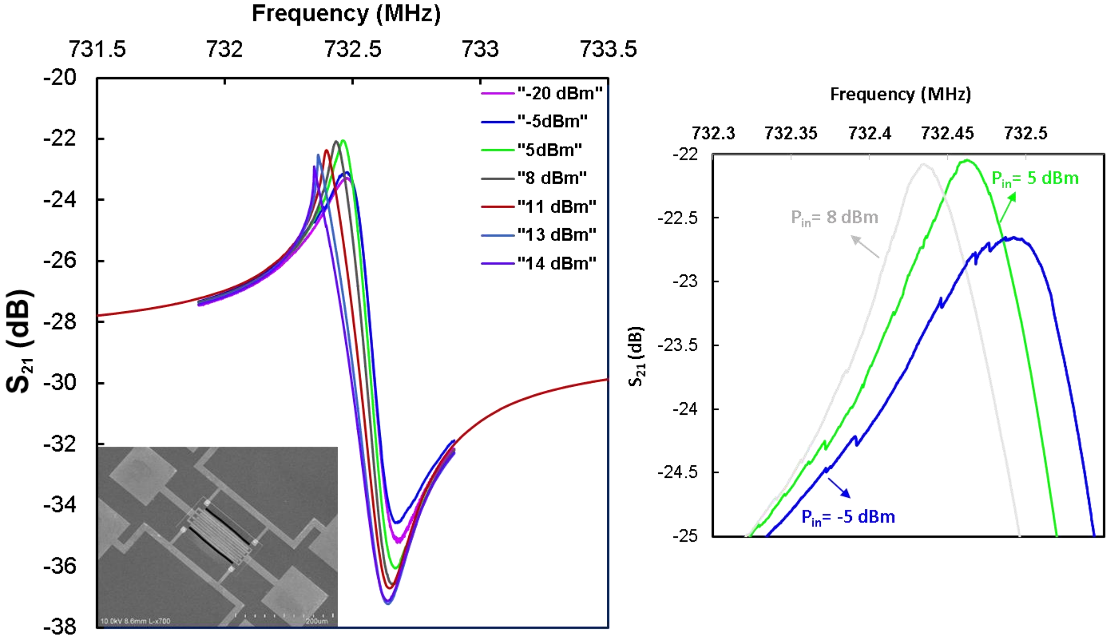

Figure 5.16 Phonon trap frequency response when the input RF power is varied from -20 dBm to 14 dBm. The improvement of *IL* and *Q* from -20 dBm to 5 dBm is attributed to efficient charge modulation as the depletion layer varies. The inset shows the zoomed plot. The weak spurious resonance modes are supressed a higher input levels.

The linearity and power handling capability of the 740 MHz phonon trap is characterized using two-tone power measurements. Fig. 5.17 demonstrates the third-order input intercept point (IIP_3) of the acoustic phonon trap with an extracted value of 31.2 dBm, proving high power handling capability of such devices. Similar power handling values have been measured for thickness mode resonators that also do not rely on narrow power-sensitive tethers.

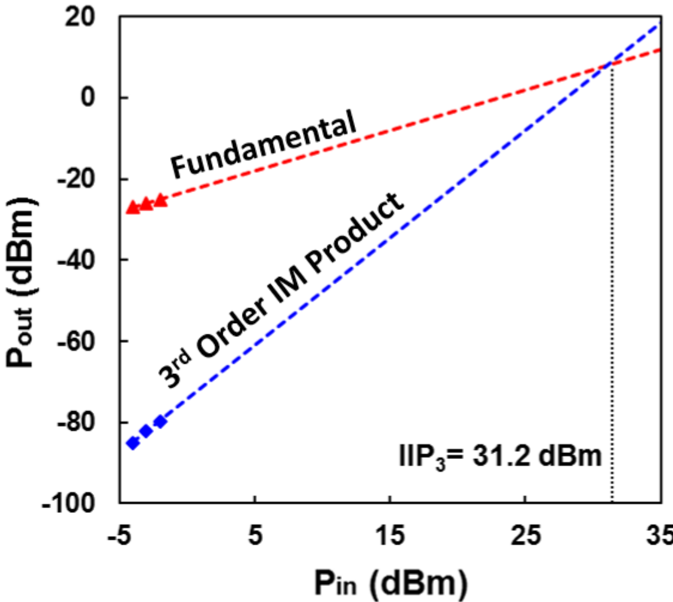

Figure 5.17 Two-tone power measurement of the resonator shown in Fig. 6. The frequency separation of the two tones is 20 kHz and the extracted IIP3 value is 31.2 dBm.

5.8.3 Temperature Trends

The resonance frequency drift with respect to ambient temperature is studied. The temperature coefficient of frequency (TCF) is extracted to be ~ -21 ppm/K in the linear

region. We observe a turnover temperature of ~160 K in our devices both for the third-order and ninth-order width-extensional resonance modes.

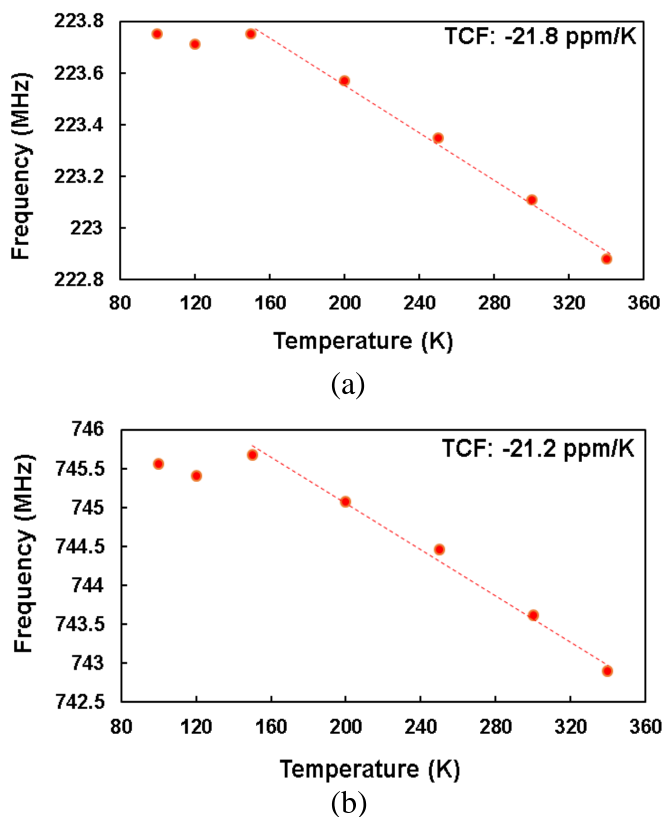

Figure 5.18 Frequency vs. temperature dependency of (a) third-order resonance, and (b) ninth-order resonance modes of acoustic phonon trap. A TCF of ~-21 ppm/K is extracted for both resonance modes.

5.9 Forward-biased Schottky IDTs

Various approaches have been sought so far to reduce the temperature sensitivity of the resonance frequency in MEMS resonators, particularly when used as frequency references in time keeping application. One of the approaches is "ovenization" or constant flow of a DC current to keep the temperature of the device constant and less sensitive to changes in

the environmental temperature variations. Inspired by self-ovenized platform as well as addition of frequency tuning, we bias the sense IDT set in forward bias region in this section. Piezoelectric resonators typically suffer from small frequency tuning capability. By using a current-assisted readout scheme, we can tune the resonance frequency via Joule heating of the device. The actuation IDT set is still kept in the depletion region to ensure efficient piezoelectric transduction. Figs. 5.19 (a), and (b) show an SEM image along with the DC-IV characteristic of the output Schottky IDT set at different depletion voltages of the input IDT set. Fig. 5.20 shows the frequency response at different DC voltage levels applied to the forward biased output IDT. The frequency of resonance shifts by 500 ppm, when input DC power is 25 mW. The linear trend between the frequency tuning *vs.* consumed power proves that Joule heating is the dominant frequency tuning mechanism. Furthermore, the slope of Fig. 5.20(b), when divided by the thermal resistance yields the TCF of the device, agreeing well with the measured TCF values shown in Fig. 5.18. Fig. 5.21 shows the frequency tuning vs. DC voltage applied to the sense IDT demonstrating the significant frequency tuning, when sense IDT is forward biased.

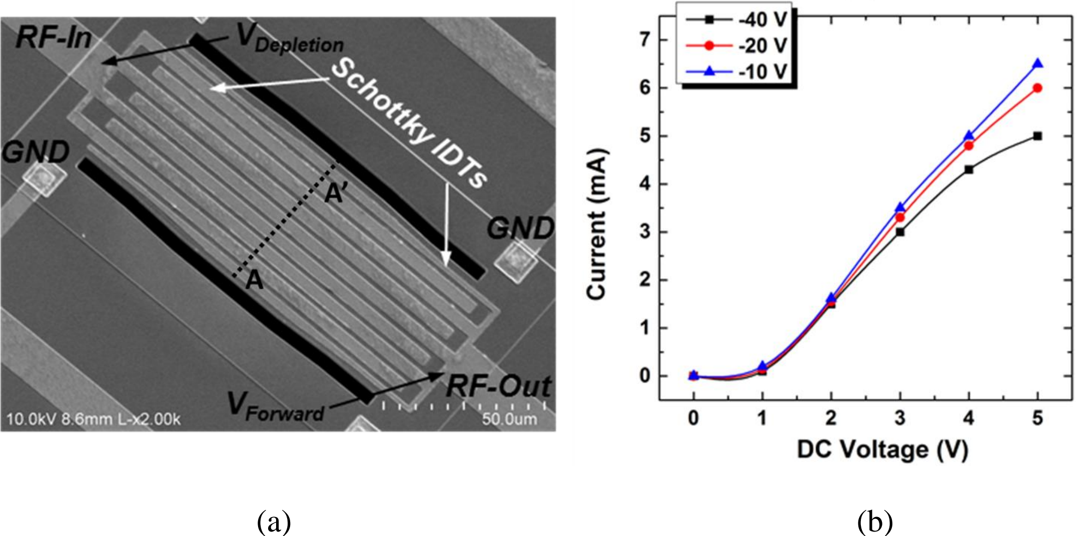

(a) (b)

Figure 5.19 (a) SEM image of the AlGaN/GaN resonator. Access to the 2DEG sheet is provided by Ohmic contacts outside of the active device area indicated as GND. (b) DC I-V curve of the forward biased output Schottky IDT, when input IDT set is biased at -10 V, -20 V, and -40 V.

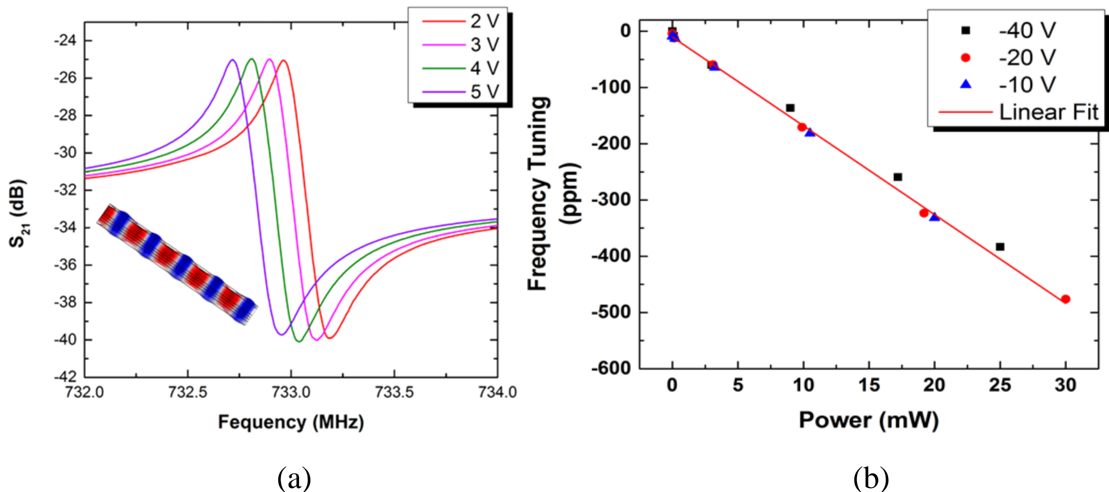

(a) (b)

Figure 5.20 (a) Frequency response of the AlGaN/GaN resonator at its 9th-order width-extensional resonance mode at frequency of ~733 MHz and Q= 4,500, when the input IDT set is biased in depletion (i.e. V_{DC}= -40 V) and the output IDT set is forward biased with a DC voltage varying from 2 V to 5 V. The cross section of COMSOL simulation of the stress profile is shown in the inset. (b) Frequency tuning versus consumed DC power. Actuation IDT set is biased in depletion (V_{DC}= -40 V, -20 V, and -10 V) and sense IDT setis biased in forward region. The slope of the linear fit is -10 ppm/mW.

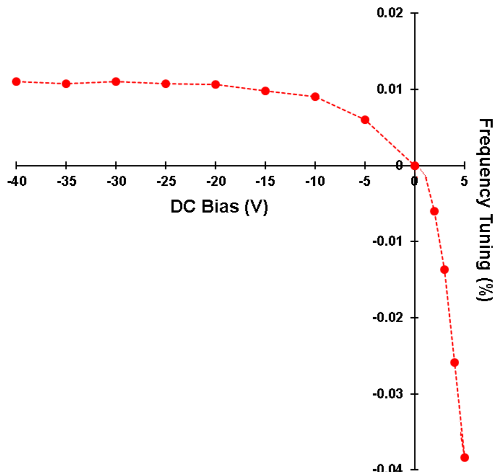

Figure 5.21 Normalized resonance frequency vs. DC voltage applied to the sense IDT set. The acuation IDT bias is maintained at -40 V. The resonance frequency is normalized against its value at 0 V. Significant frequency tuning is observed once the sense IDT set enters the forward bias region.

5.10 Embedded Resonant AlGaN/GaN HEMTs

Based on the efficient actuation mechanism and novel phonon trap discussed so far, we now integrate and embedded HEMT on the acoustic cavity and utilize it to sense the acoustic resonance mode. The signal readout is based on the piezo-resistive properties of 2DEG channel in the embedded HEMT. A wide-range frequency tuning is achieved by flowing DC current through the contacts, causing large elastic modulus change due to Joule heating of the device. Frequency tuning allows for compensation of effects of fabrication variations as well as environmental changes. The ninth-order width extensional resonance mode at ~719 MHz shows Q amplification from 1,710 at V_{DS}= 4 V to 13,851 at V_{DS}= 9 V with more than 2,500 ppm of frequency tuning. Resonant devices with such large frequency tuning are perfect candidates as in-situ temperature sensors, where the resonance frequency shift is an indicator of the temperature rise in the channel of the suspended HEMT.

Taking advantage of the current-assisted readout, we now replace the sense Schottky-IDT sets with a resonant HEMT, and flow various DC current levels to study the effect of electric field and current between S/D in HEMTs on the acoustic performance of such resonant HEMTs. Fig. 5.22 shows the schematic and mode shape of the resonant HEMT discussed.

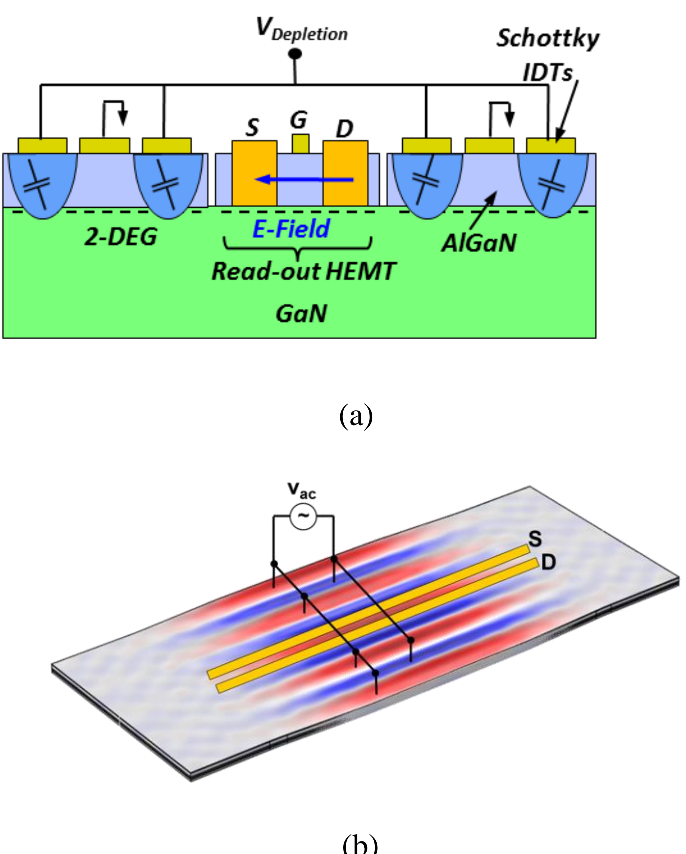

Figure 5.22 (a) A cross-section schematic of a resonant HEMT, with three IDT fingers on each side of the acoustic cavity for piezoelectric actuation and an embedded HEMT in the middle of the cavity to readout the strain. (b) COMSOL simulation of stress profile of the ninth-order width-extensional resonance mode indicating the Source and Drain located at the location of maximum stress.

5.11 Resonant HEMTs: Design and Characterization

The geometrical design of the acoustic cavities in the resonant body transistors were explained in detail in Section 5.7. The ninth-order width extensional mode of resonance is excited, wherein the two main contributions to the actuation force are the modulation of impedance of the depletion region and the piezoelectric strain between two adjacent electrodes. A large electric field is applied between the source and drain of the readout HEMT to sense the induced piezoelectric stress. The actuators are placed on the two sides of the device and the suspended HEMT is placed in the middle of the structure. Fig. 5.23 shows the SEM image of the resonant HEMT.

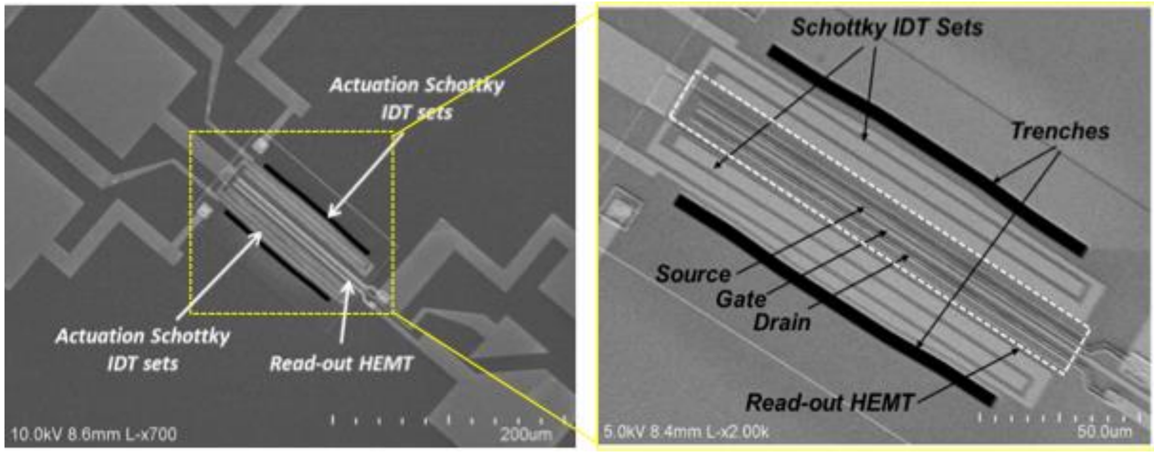

Figure 5.23 SEM images of the resonant body HEMT. The trenches are tapered to concentrate the acoustic energy in central region of the device and couple the propagating acoustic wave in the center to the evanescent waves in the flanges.

The DC I_{DS}-V_{DS} and P_{DC}-V_{DS} characteristic of the embedded HEMT is shown in Fig. 5.24.

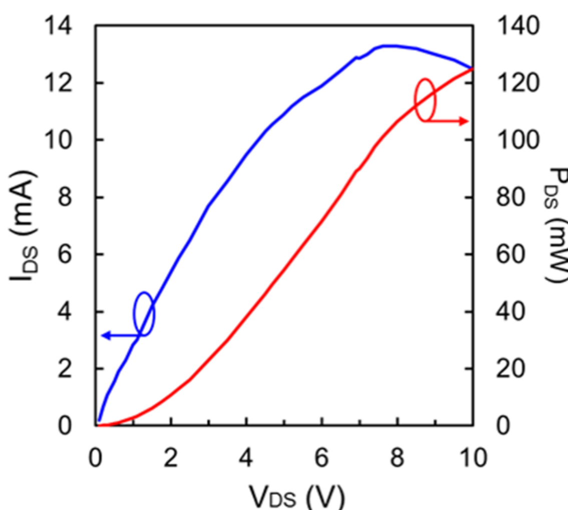

Figure 5.24 DC trends of the current and consumed DC power of the embedded HEMT, when no DC voltage is applied to the gate.

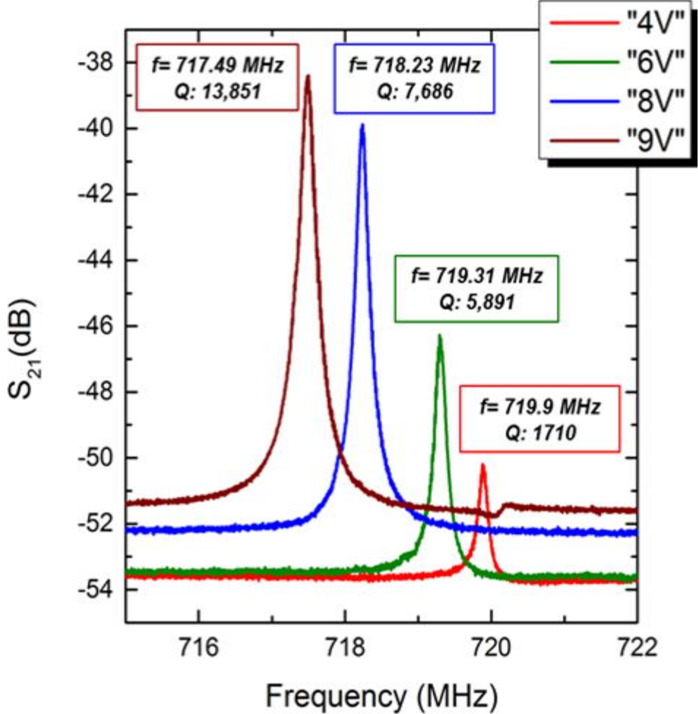

Figure 5.25 Frequency response of the AlGaN/GaN resonator at various V_{DS}. The drain-source DC voltage is varied from 4 V to 9 V. The quality factor of the resonator increases with an increase in the electric field applied between the source and drain.

Q amplification and frequency tuning is observed with application of larger DC voltages to the readout HEMT. The readout mechanism is highly sensitive to the DC voltage and Joule heating of the device. The Q enhancement observed upon application of DC voltages to the readout HEMT is attributed to internal generation of thermo-elastic forces that add constructively to the initial depletion-mediated actuation force. In piezo-resistive readout schemes, the transconductance (g_m) is defined as:

$$g_m = \frac{i_{out}}{v_{in}} = |y_{21} - y_{12}|, \qquad \text{(Equation 5.15)}$$

where y_{21} and y_{12} are the admittance parameters. Fig. 5.26 shows the piezo-resistive transconductance and its dependency on V_{DS}.

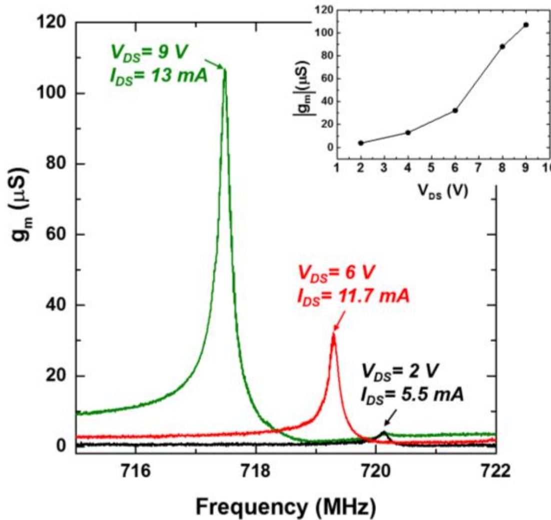

Figure 5.26 Frequency response of the piezo-resistive trans-conductance (g_m). |g_m| rises to ~107 μS when V_{DS} is biased at 9 V and is hardly detectable with a value of only ~2 μS at V_{DS}= 2 V. The inset shows the dependency of |g_m| on V_{DS}.

5.12 *Q* Enhancement Mechanism in Resonant HEMTs

Significant *Q* enhancement of ~8× was observed in Fig. 5.25, with *Q* rising from 1,710 at V_{DS}= 4 V to 13,851 at V_{DS}= 9 V without any external feedback applied to the system. Similar *Q*-enhancement results have been reported for Si resonators with piezo-resistive [5.22, 5.23] or FET-based [5.24] readout, with frequencies ranging from a few MHz to several GHz.

Different mechanisms have been sought so far to explain such current-assisted *Q* enhancement phenomenon. One possible explanation is that a series of inter-related mechanisms give rise to an alternating elastic force added in phase to the initial piezoelectric actuation force at the frequency of resonance [5.25]. To shed light on this phenomenon, we take a closer look at the power consumed in the readout HEMT. The dissipated power at the readout HEMT has two constitutive current components:

$$P_{DC} = R_{DS}(I_{DC} + i_{AC})^2, \quad \text{(Equation 5.16)}$$

which translate into frequency components at f_0 and $2f_0$ and a DC term, where f_0 is the frequency of resonance. At the frequency of resonance, due to the modulation of the resistance of the 2-DEG between the source and the drain (ΔR_{DS}), the dissipated power varies, causing local heating/cooling of the channel. Such thermal forces give rise to elastic forces that can expand/contract the device. Depending on the phase of this additional thermo-elastic force, it can add up to or subtract from the original piezoelectric actuation force and thus at certain conditions can enhance the quality factor quite significantly [5.23].

Same principle is the basis of operation of parametric amplifiers and laser-driven micromechanical oscillators.

In our implemented HEMT-based readout scheme, the periodic drain-source resistance (R_{DS}) variation is utilized to sense the strain at the frequency of resonance, through a change in the drain-source voltage. Running current through R_{DS} acts as an actuator itself, feeding energy from a third terminal into the system, where the additional force is dependent on ${I_{DC}}^2$. The generated thermal energy due to piezo-resistive effect is calculated as:

$$P_{added} = \Delta R_{DS}(I_{DC})^2, \quad \text{(Equation 5.17)}$$

5.13 Thermal Modelling

Another advantage of using current-assisted acoustic resonators is the large frequency tuning that is only achievable through Joule heating in piezoelectric bulk-acoustic resonators. Fig. 5.28 (b) plots the frequency tuning versus the consumed power, where the linear trend proves that the Joule heating of the device is indeed responsible for the frequency tuning.

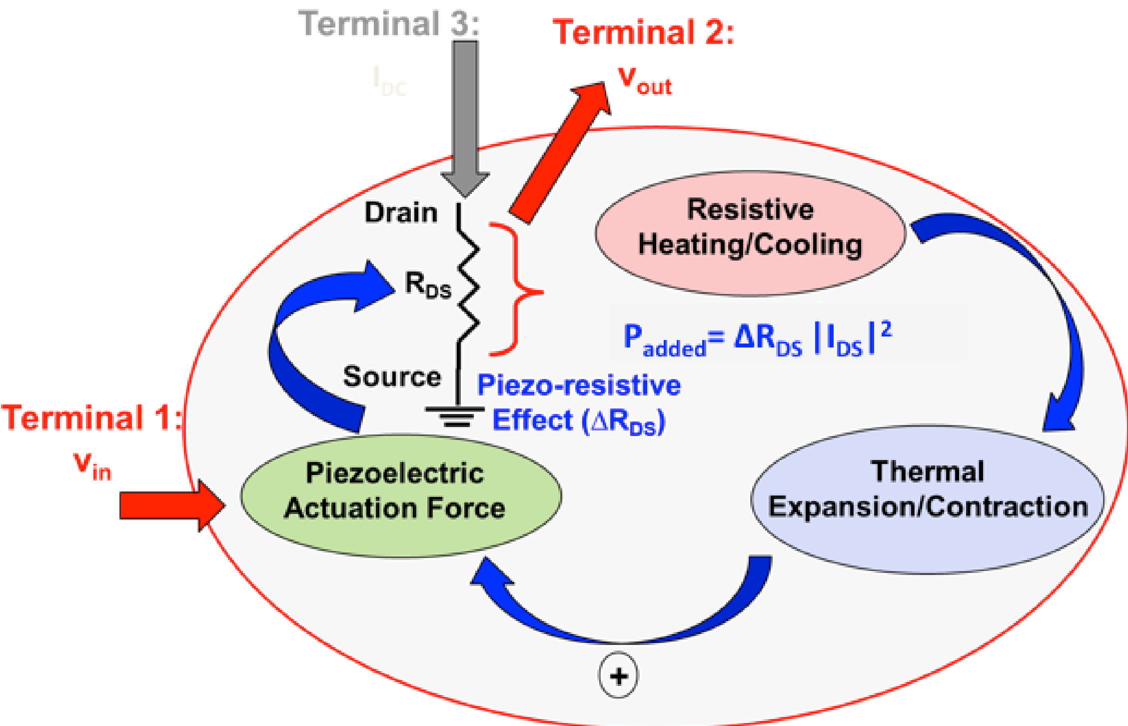

Figure 5.27 Thermo-elastic feedback loop, indicating the three terminals of the resonant HEMT (RF input, output and DC Source) and demonstrating a series of inter-related mechanisms. Once the thermal expansion/contraction caused by the resistive heating/cooling is in phase with the initial piezoelectric actuation, Q is enhanced.

Knowledge of the temperature of the channel of AlGaN/GaN HEMTs is essential to improve the device reliability and to optimize device design and performance; however, direct measurement of channel temperature is usually complicated. Here, we introduce a simple in-situ and non-destructive temperature sensing of the HEMT channel by using our resonant HEMTs. We then compare the extracted channel temperature using the frequency shift with the measurement results using a micro-thermocouple in contact with the surface of the HEMT channel. The temperature rise in the HEMT channel is calculated based on the consumed DC power and the thermal resistance of the resonant HEMT by:

$$\Delta T = \Delta P_{DC} \times R_{th}, \qquad \text{(Equation 5.18)}$$

The thermal resistance (R_{th}) of the resonant HEMTs can be extracted from the slope of the frequency tuning versus DC power, plotted in Fig. 5.28(b), and the measured TCF of such devices as:

$$R_{th} = \frac{(\frac{\Delta f}{f})}{\Delta P_{DC}} \times \frac{1}{TCF}, \qquad \text{(Equation 5.19)}$$

Using a slope of -29 ppm/mW from Fig. 5.28(b) and a measured TCF value of ~ -27 ppm/K for such devices, the thermal resistance is calculated as R_{th}= 1,074 K/W based on Eq. 5.19. Plugging the extracted value of R_{th} back into Eq. 5.18, the temperature rise in the channel at ΔP_{DC}= 110 mW is estimated as ΔT =118 K.

Moreover, since the thermal resistance of the device is dominated by the thermal resistance of the two wide tethers that connect the resonator to the heat sink (*i.e.* substrate), R_{th} could have been simply calculated as:

$$R_{th} = \frac{1}{2} R_{tether} = \frac{1}{2} \times \frac{1}{K} \frac{L}{wt}, \qquad \text{(Equation 5.20)}$$

where K is the thermal conductivity of GaN (K= 130 W/m.K) and t is the total GaN epi-layer thickness (t= 1.8 μm). L and w are the length and width of the wide tethers. Eq. 5.20 yields a thermal resistance value of R_{th}=1,068 K/W, which agrees very well with the extracted R_{th} from Eq. 5.19.

To compare the estimated channel temperature rise using our in-situ temperature sensors with readings from a thermocouple, we utilized a micro-thermocouple that touches the surface of the suspended HEMT channel during operation. At P_{DC}= 110 mW, an increase of $\Delta T \approx 100 \pm 20$ K is measured with a thermocouple which agrees well with ΔT=

118 K estimated by our thermal model based on the in-situ temperature sensor. It must be noted that since the precise positioning of thermocouple tip on the channel surface was rather difficult, the temperature readings from the thermocouple are not as accurate as our resonant HEMTs and are only used to roughly estimate the temperature in the channel.

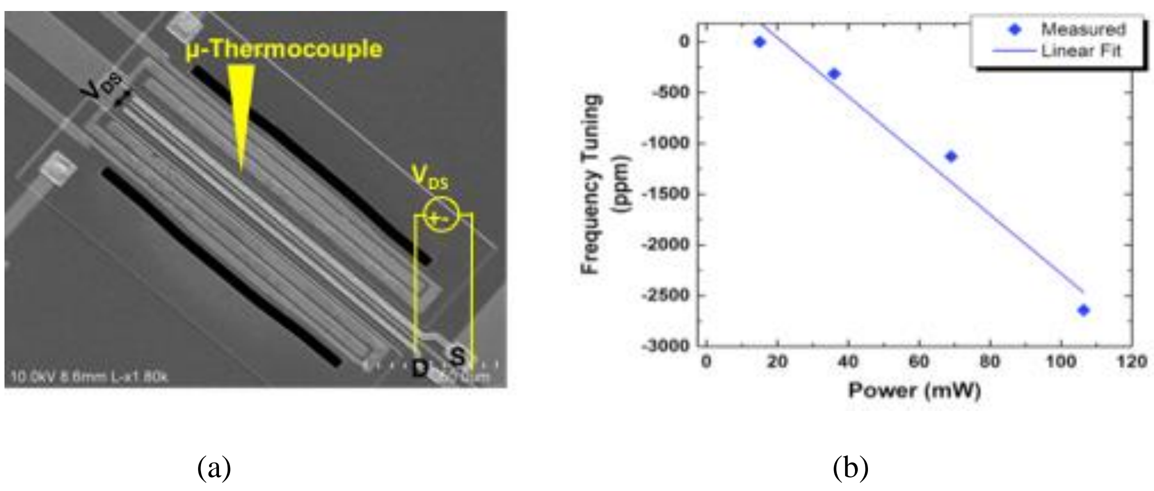

(a) (b)

Figure 5.28 (a) SEM image of the resonant using a micro-thermocouple to estimate the temperature rise in the channel of the HEMT. (b) Frequency tuning versus consumed DC power. The slope of the linear fit is -29 ppm/mW.

It is worth mentioning that such resonant HEMTs are ovenized in nature. That is, by flowing a constant DC current in the HEMT channel and maintaining a constant channel temperature, the device becomes essentially insensitive to normal environmental temperature changes and merely reflects the HEMT channel temperature. Such devices can be used as temperature-compensated resonators with internal *Q*-amplification used in frequency-stable self-sustained oscillator circuits.

5.14 Conclusion

In this chapter, we introduced depletion-mediated piezoelectric transduction in AlGaN/GaN resonators and showed higher Q and acoustic velocity tunability as compared to pure GaN resonators with higher strain generated at the same electrical voltage input. We demonstrated phonon traps for the first time in AlGaN/GaN platforms and embedded AlGaN/GaN HEMTs for acoustic signal pickup on the acoustic cavities. Finally, frequency-tunable current-assisted resonators were presented, which combine depletion-mediated piezoelectric actuation with current-assisted piezo-resistive sensing. The presented resonators show $f \times Q$ values as large as $\sim 1 \times 10^{13}$ upon application of DC voltage, which is the highest reported in the literature to date, with an added advantage of a wide frequency tuning range. The presented resonant HEMTs also act as in-situ sensors of the temperature of the HEMT channel. Furthermore, by running a fixed DC current in the HEMT channel, we can implement temperature-compensated resonators with internal Q-amplification used in self-sustained oscillators in frequency references. By optimizing the designs of the presented resonant HEMTs, thermal oscillators can be realized that operate without the need of any electronic feedback components.

Chapter 5: References

[5.1] F. S. Hickernell, IEEE Trans. Ultrason. Ferroelectr. Freq. Control 52, 737. 2005.

[5.2] S. C. Masmanidis *et al.*, Multifunctional Nanomechanical Systems via Tunably Coupled Piezoelectric Actuation, Vol. 317, pp. 780-2, Aug 2007

[5.3] J. Ransley, *et al.*, Silicon depletion layer actuators, Applied Physics Letters, 92, 184103 (2008)

[5.4] E. Hwang and S. A. Bhave, "Transduction of high-frequency micromechanical resonators using depletion forces in p-n diodes," IEEE Transactions on Ultrasonics, Ferroelectrics, and Frequency Control, vol. 57, no. 7, pp. 1664-1672, 2010.

[5.5] J. J. Wortman, J. R. Hauser, and R. M. Burger, "Effect of Mechanical Stress on p-n Junction Device Characteristics," J. Appl. Phys., vol. 35, no. 7, p. 2122, 1964.

[5.6] L.C. Popa, D. Weinstein, "Switchable Piezoelectric Transduction in AlGaN/GaN MEMS Resonators" *International Conference On Solid-State Sensors, Actuators and Microsystems (Transducers 2013)*, June 16-20, 2013.

[5.7] M. Faucher *et al.*, "Electromechanical transconductance properties of a GaN MEMS resonator with fully integrated HEMT transducers," Journal of Micromechanical Systems (JMEMS), vol. 21, no. 2, pp. 370–378, April 2012.

[5.8] L. Shao *et al.*, "Emission and detection of surface acoustic waves by AlGaN/GaN high electron mobility transistors," Appl. Phys. Lett. 99, 243507 (2011)

[5.9] G. Piazza, P. J. Stephanou, and A. P. Pisano, "Piezoelectric Aluminum Nitride Vibrating Contour-Mode MEMS Resonators," Journal of Microelectromechanical Systems (JMEMS), vol. 15, no. 6, pp. 1406–1418, Dec. 2006.

[5.10] Z. J. Zhi et al., "Determination of the relative permittivity of the strained AlGaN barrier layer in AlGaN/GaN heterostructures," Chinese Physics B, Vol. 18, No. 9, Sept. 2009.

[5.11] P. Javorka, "Fabrication and characterization of AlGaN/GaN high electron mobility transistors," PhD thesis, RWTH, Aachen, Germany, Feb. 2004.

[5.12] Z. Miao and L. Xin-Yu, "Analysis of Capacitance-Voltage-Temperature Characteristics of GaN High-Electron-Mobility Transistors," Chinese Physics Letters, Vol. 32, No. 4 (2015) 048501.

[5.13] O. Ambacher *et al.*, "Two dimensional electron gases induced by spontaneous and piezoelectric polarization in undoped and doped AlGaN/GaN heterostructures," Journal of Applied Physics, Vol. 87, No. 1, pp. 334-344, Jan. 2000.

[5.14] O. Ambacher *et al.*,“ Two-dimensional electron gases induced by spontaneous and piezoelectric polarization charges in N- and Ga-face AlGaN/GaN heterostructures,” Journal of Applied Physics, Vol. 85, No. 6, March 1999, pp. 3222-3233.

[5.15] R. Vetury *et al.*, “The impact of surface states on the DC and RF characteristics of AlGaN/GaN HFETs,” *IEEE Transactions on Electron Devices (T-ED)*, vol. 48, no. 3, March 2001.

[5.16] D. L. White *et al.*, “Ultrasonic wave transmission device utilizing semiconductor piezoelectric material to provide selectable velocity of transmission,” US Patent, 3200354, Aug. 1959.

[5.17] V. J. Gokhale and M. Rais-Zadeh, “Phonon-electron interactions in piezoelectric semiconductor bulk acoustic wave resonators*,” Nature Scientific Reports*, 4:5617, DOI: 10.1038, 2014.

[5.18] K. Tonisch *et al.*, “Piezoelectric actuation of GaN/AlGaN/(GaN) heterostructures,” J. Appl. Phys., 104, 084516 (2008)

[5.19] S. M. Sze, Semiconductor Devices, Physics and Technology Wiley, New York, 2002.

[5.20] M. Shahmohammadi, B.P. Harrington, and R. Abdolvand, “Concurrent enhancement of Q and power handling in multi-tether high-order extensional resonators,” *Proc. IEEE MTT-S International Microwave Symposium*, Anaheim, CA, 23-28 May 2010.

[5.21] R. Tabrizian *et al.*, “Acoustically-engineered multi-port AlN-on-silicon resonators for accurate temperature sensing*,” IEEE International Electron Device Meeting (IEDM)*, pp. 18.1.1-4, 2013.

[5.22] Weinstein and S. Bhave, “Piezoresistive sensing of a dielectrically actuated silicon bar resonator,” *Solid State Sensors, Actuators and Microsystems Workshop*, Hilton Head, pp. 368-371, June 2008.

[5.23] A. Rahafrooz and S. Pourkamali, “Thermalpiezoresistive energy pumps in micromechanical resonant structures,” *IEEE Transactions on Electron Devices*, Vol. 59, No. 12, pp. 3587–3593, Dec. 2012.

[5.24] D. Grogg and A. M. Ionescu, “The vibrating body transistor,” *IEEE Transactions on Electron Devices*, Vol. 58, No. 7, pp. 2113-2121, July 2011.

[5.25] P. G. Steeneken *et al.*, “Piezoresistive heat engine and refrigerator,” *Nature Physics*, Vol. 7, pp. 354–359, January 2011.

Chapter 6 Big Picture & Future Directions

6.1 Summary and Big Picture

The focus of this thesis has been the development and demonstration of novel electro-acoustic devices and integration of GaN-based micro-electro-mechanical devices with GaN HEMTs and circuitry. Fig. 6.1. schematically summarizes the devices realized in this Ph.D. work and discussed thus far. The ultimate goal of this work is integration of electric/acoustic devices with different functionalities to build more-complicated integrated microsystems, as well as realizing novel electro-acoustic devices. Fig. 6.2 shows a simple transceiver module ideally realized in all-GaN platform. To this end, we have so far implemented GaN micromechanical resonators and filters (FBARS, acoustic filters, resonators, phonon traps, resonant body HEMTs, and *etc.*) integrated with GaN HEMTs. All the devices discussed so far operate based on reciprocal propagation of acoustic waves. However, GaN material systems have more to offer and allow for implementation of novel electro-acoustic devices that exhibit properties not normally found in nature. Breaking the symmetry of acoustic wave propagation is one example. Non-reciprocal communication which can be realized in AlGaN/GaN material systems based on "Acoustoelectric Effect," [6.1-4] is the basis of operation of acoustic diodes, isolators, convolvers, correlators, and acoustic circulators. Such GaN-based components are compact alternatives to the state-of-the-art technology and can be integrated with GaN electronics to ultimately build a miniaturized transceiver MMIC that would significantly reduce area, noise, and cost.

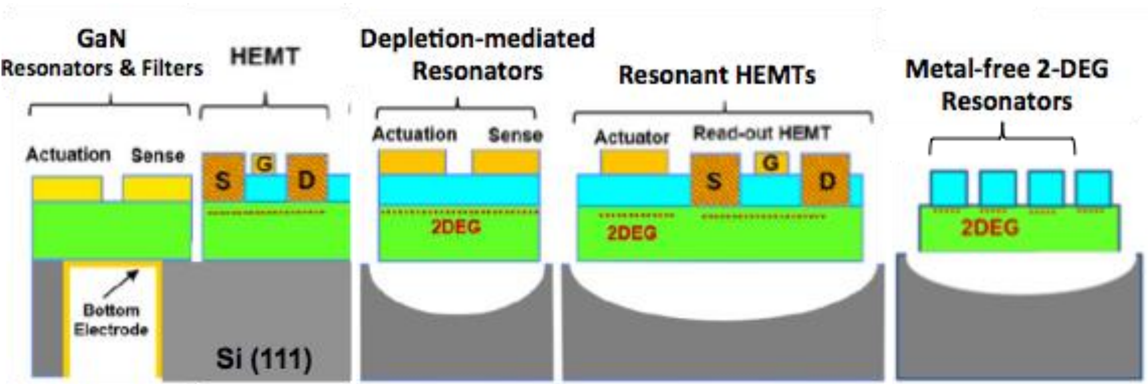

Figure 6.1 Summary of GaN-based devices realized in this work showing the schematic of cross section of various classes of GaN-based MEMS devices, HEMTs and resonant HEMTs.

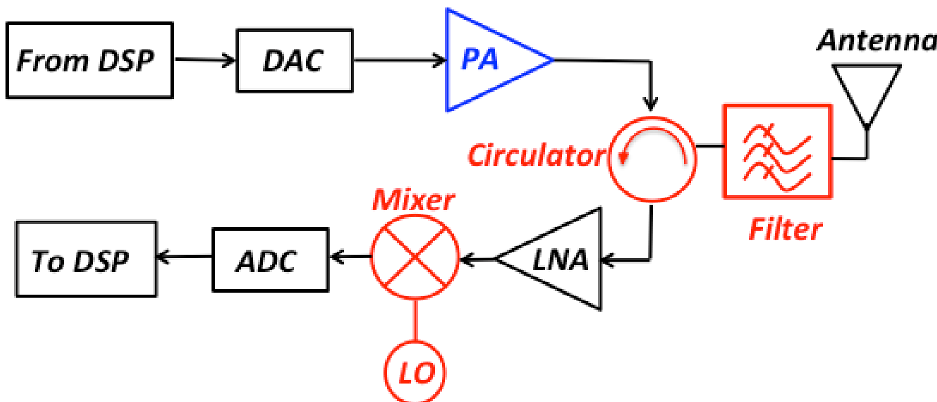

Figure 6.2 Big Picture: A simple schematic of an RF transceiver module. GaN power amplifiers (PAs) are already being used in base stations. Future direction of research on GaN includes realization of novel electroacoustic devices (e.g. acoustic circulators), and integration of all GaN components to build an integrated GaN MMIC transceiver module.

As seen in Fig. 6.2, acoustic circulators are used in RF front-ends to enable full-duplex systems to increase isolation between the transmit and receive channels. Using acoustic circulators, makes transmission of high power signals without saturating the receiver LNA possible. This also saves RF bandwidth. Unlike their ferrite-based magnetic counterparts, such acoustic circulators are compact and can be integrated with rest of the GaN circuitry.

Acoustoelectric effect enables amplification or attenuation of acoustic waves when they propagate in a piezoelectric media wherein a DC electric field is applied to in the same direction as the acoustic wave. If the electron velocity is larger (or smaller) than the acoustic velocity, the amplitude of the acoustic wave is amplified (or attenuated) under certain conditions (Fig. 6.3). “It is known that when a travelling acoustic wave propagates through a piezoelectric semiconductor, it induces a traveling sinusoidal potential that causes bunching of carriers and hence a periodic variation in electrical conductivity. In the presence of a DC current, this periodic conductivity leads to an additional periodic potential that has a phase difference with respect to the acoustic wave due to the motion of charge carriers. This phase difference leads to acoustic amplification under the condition that the electron drift velocity is higher than the acoustic wave speed.” [6.5]

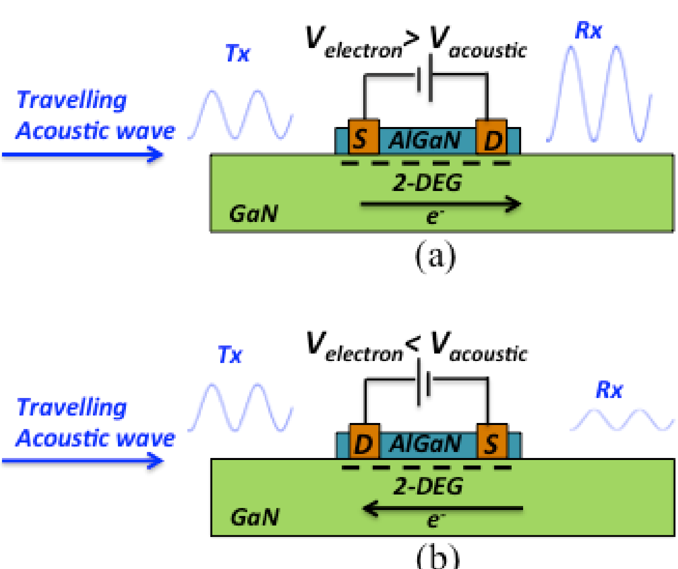

Figure 6.3 (a) Amplification, (b) attenuation of travelling acoustic wave based on the direction of electric field applied to the 2DEG channel via Source and Drain Ohmic contacts. $V_{electron}$ is assumed positive if electron drift direction is the same as the travelling wave and negative if it is in the opposite direction.

6.2 Future Work

6.2.1 Acoustoelectric Effect in AlGaN/GaN Heterostructures

Piezoelectric semiconductor materials provide a perfect test vehicle to study the interaction of charge carriers (electrons) and acoustic waves (phonons). GaN is one of the few piezoelectric semiconductor materials that can be used to investigate the interplay between piezoelectric strain and charge carriers. Few reports exist on the theoretical study of acoustoelectric in bulk-mode GaN [6.6-7], and comparison of acoustoelectric effect in 2D GaN and bulk GaN and emission and detection of surface acoustic waves in GaN and AlGaN/GaN and the wave directionality [6.6,8]. 2DEG sheet is extremely sensitive to strain and was shown throughout this thesis as a means for strain sensing particularly desirable at higher frequencies wherein the capacitive feed-through becomes an issue. In the cases discussed so far, an acoustic cavity is driven into a particular resonance mode through piezoelectric transduction and the strain is sensed utilizing the change in the carrier concentration (or resistivity) of 2DEG. However, 2DEG can also be used as the transmission media where travelling acoustic wave can interact with the 2DEG sheet, when travelling from an actuator (transmitter) to a sensor (receiver). The investigation of interplay between piezoelectric strain and high electric fields in piezoelectric semiconductor media is interesting from both device physics as well as application perspective.

6.2.2 Acoustic Diodes

Acoustoelectric effect breaks the acoustic wave transmission symmetry resulting in a diode effect (Fig. 6.4). The proposed acoustic diode consists of two sets of transmit and receive

interdigitated transducers (IDTs) and a transmission media on an AlGaN/GaN heterostructure. Such structure uses electrical energy as the input and delivers electrical signal as the output thus fully integrable with electrical components. The transmission media (or delay line) is comprised of the AlGaN/GaN heterostructure where 2DEG interacts with acoustic phonons. An external electric field is applied to the 2-DEG through two Ohmic contacts. Depending on the direction of the electric field and under certain conditions, the travelling acoustic wave generated from the transmit IDT can be amplified or attenuated when picked up by the receive IDT set. The targeted acoustic resonance modes in such devices are travelling surface acoustic waves or travelling Lamb-waves. It is important to avoid creation of standing waves in the designed acoustic cavities to enhance the uni-directionality. Therefore, reflections from the free boundaries should be suppressed.

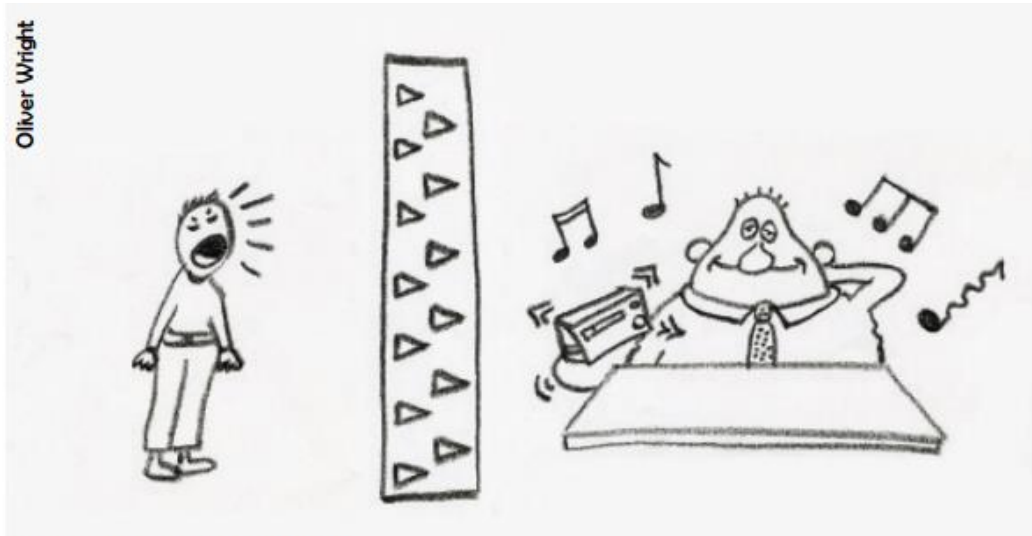

FIG. 7. “What is a phonon diode!?”

Figure 6.4 Acoustic diode or listening without being heard [6.9].

Fig. 6.5 shows SAW and Lamb-wave acoustic diodes realized in AlGaN/GaN heterostructures. The AlGaN layer can alternatively be maintained in the transduction area for more efficient actuation force.

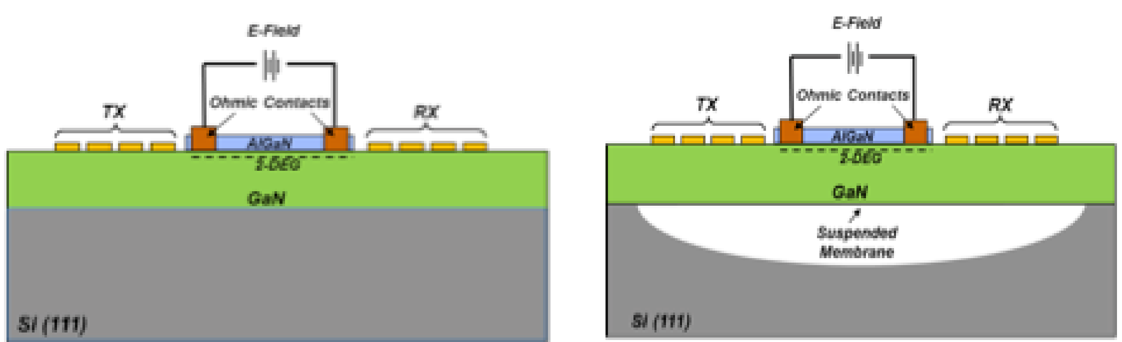

Figure 6.5 Realization of piezoelectric acoustic diodes based on travelling surface acoustic waves or Lamb waves. The acoustic cavity is designed to avoid creation of standing waves. If the GaN waveguide is continuous in the wave propagation direction, the reflections from the edges are minimized and thus one-directional acoustic communication would be possible.

As a proof of concept, travelling Lamb-wave delay lines have been realized in GaN thin films with two sets of transmit and receive IDT sets. The same acoustic cavity has been realized based on standing waves to compare the resonance modes existing in such material stack. The two designs have the same pitch size and IDT finger width. The frequency responses and the SEM images are shown in Fig. 6.6.

6.2.3. Acoustic Circulators

Another possible research direction is combining three acoustic diodes to build a three-port acoustic circulator. Such acoustic circulators are orders of magnitude smaller and lighter than their electromagnetic (or optical) counterparts based on magnetized ferrite at the same frequency bands. They can also be potentially integrated with on-chip electronics.

Depending on the direction of the DC electric field, the acoustic wave can be transmitted from Port 1 to Port 2, and blocked from Port 3 to Port 2 for instance.

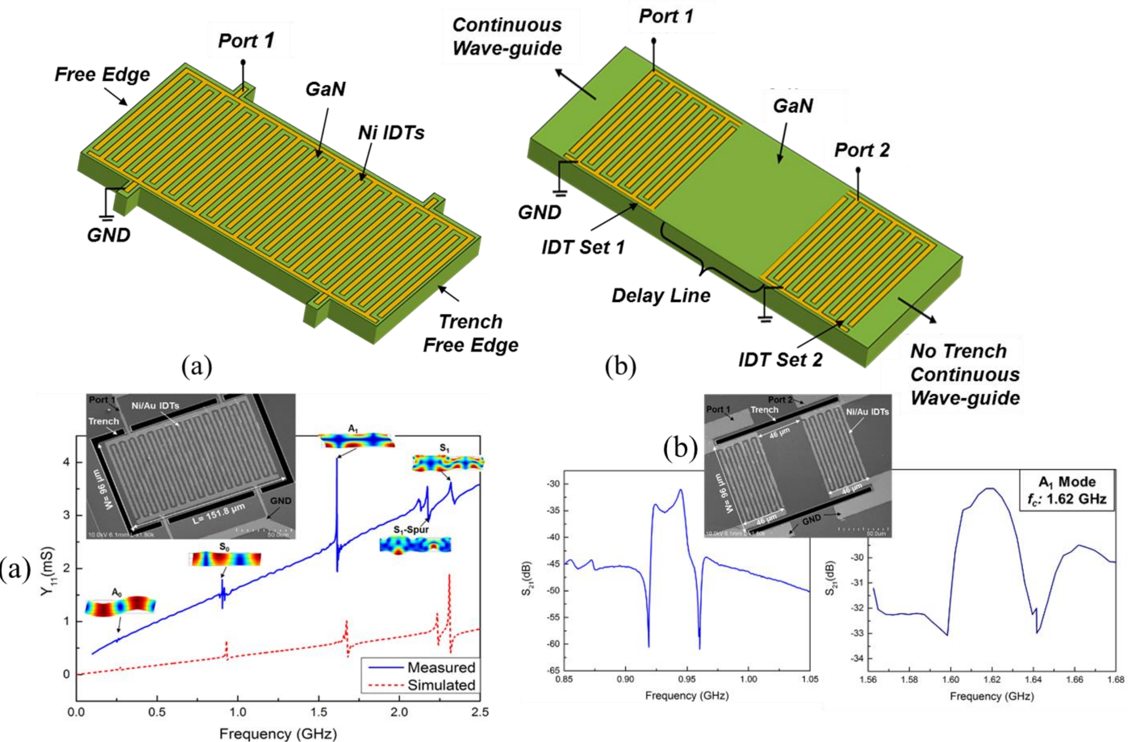

Figure 6.6 (Top) Schematic images of Lamb-wave GaN devices, showing (a) the standing wave resonator, and (b) the travelling-wave delay-line structure. (Bottom) Frequency response of (a) the resonator and (b) the delay-line. The SEM images are shown in the inset. [6.10]

A circulator waveguide is used to allow for simultaneous acoustic wave transmission among the three ports. The acoustic circulator consists of three functional components: electromechanical transducers for generating acoustic wave based on the piezoelectric properties of GaN, acoustic waveguides for steering traveling wave and active areas for breaking reciprocity. The acoustic waves are generated using the piezoelectric properties of GaN and are amplified/attenuated through their interaction with 2DEG at AlGaN/GaN interface. Such devices find application in full-duplexing RF front-end, on-chip radar system, and *etc.*

6.2.4 Other GaN-based Electroacoustic Devices

Besides non-reciprocal acoustic devices, one can envision numerous novel devices and microsystems realized in GaN. Of special interest would be applications requiring operation of optical, mechanical, and electrical elements at high temperatures that conventional Si-based technologies cannot endure. Such GaN systems can be especially attractive for mining and harsh environment resource exploration, aerospace, and defense. Subsequent future direction of this work were discussed at the end of each chapter. Here, I provide a list of other novel devices that can further diversify future integrated microsystems. To name a few, GaN, being piezoelectric, pyroelectric and piezo-resistive, has a great potential for harsh environment sensing, which includes resonant as well as non-resonant sensing. The resonant sensors would sense through a shift in their resonance frequency, while the non-resonant sensors utilize an absorption coating on the gate area to sense gas, proteins, bio-molecules, *etc.* through the change in 2DEG sheet density. Also, the high strain sensitivity of 2DEG can be used in strain sensors used in harsh environments. Thermal oscillators can be utilized due to the high current levels flowing in 2DEG and based on the thermo-elastic feedback loop. Furthermore, modulation of gate-source voltage in HEMTs, generate surface acoustic waves that could be harvested to actuate acoustic devices. This is readily available in HEMT technology. Methods of utilizing acoustic waves to monitor the HEMT channel temperature is yet another direction of future research. In short, one can envision numerous novel semiconductor devices that would combine the advantages that GaN has to offer.

6.3 Challenges and Mitigations

One of the biggest challenges in the area of research on GaN is that the growth and material characterization of GaN wafers are still at infancy. In fact, the material properties of GaN are highly dependent on the growth conditions and vary from wafer to wafer. Different industrial vendors sell GaN wafers with various defect densities, doping levels, nucleation layers with different thickness and *etc*. Furthermore, properties, such as the residual stress present between the epitaxial layers and the host substrate can contribute to various mechanical/acoustic properties. This leads to a wide range of numbers that cannot be trusted, making accurate design of GaN-based devices rather challenging. In this work, test structures were utilized to extract the electromechanical properties of GaN in the first place, so that they can be used to build electromechanical devices upon such parameters.

Collaboration between industry and university can significantly help mitigate such problems by carefully characterizing the epitaxial stack. Knowledge of the exact composition of the GaN-based epitaxial stack and the properties of AlN/GaN thin films grown on Si (111), as well as the ability to grow high quality pure GaN thin films, whether via epitaxial growth or sputtering can significantly improve the design of novel electro-acoustic devices enabling tighter control over the performance metrics.

Chapter 6: References

[6.1] R. H. Parmenter, "The acousto-electric effect," *Physical Review*, Vol. 89, No. 5, March 1953.

[6.2] G. Weinreich and H. G. White, "Observation of the acoustoelectric effect," *Physical Review*, Vol. 106, pp. 1104–1106, 1957.

[6.3] A. R. Hutson, D. L. White, and J. H. Mcfee, *Physical Review Letters,* Vol. 7, No. 237, 1961.

[6.4] R. M. White and F. W. Voltmer, "Direct piezoelectric coupling to surface acoustic waves," *Applied Physics Letters,* Dec. 15, 1965.

[6.5] L. Shao *et al.*, "Amplification and directional emission of surface acoustic waves by a two-dimensional electron gas," *Applied Physics Letters*, 106, 023106, 2015.

[6.6] V. J. Gokhale and M. Rais-Zadeh, "Phonon-electron interactions in piezoelectric semiconductor bulk acoustic wave resonators," *Nature Scientific Reports*, 4:5617, DOI: 10.1038, 2014.

[6.7] S. K Abdelraheem, D.P. Blyth andN. Balkan, "Amplification of Ultrasonic Waves in Bulk GaN and GaAlN/GaN Heterostructures*" Physica Status Solidi*, Volume 185, Issue 2, pages 247–256, June 2001.

[6.8] L. Shao, M. Zhang, A. Banerjee, P. K. Bhattacharya and K. P. Pipe, "Electrically driven nanoscale acoustic source based on a two-dimensional electron gas," *Applied Physics Letters,* Vol. 103, No. 083102, 2013.

[6.9] A. A Maznev *et al.*, "Reciprocity in reflection and transmission: what is a "phonon diode"," Oct. 2012.

[6.10] A. Ansari, H. Zhu, and M. Rais-Zadeh, "Gallium nitride high-order mode Lamb-wave resonators and delay-lines," *Solid-State Sensors, Actuators and Microsystems Workshop*, Hilton Head, SC, June, 2016.